SURFACE INSTABILITIES AND INTERFACIAL PHENOMENA FOR NANOMANUFACTURING AT THE ATOMICALLY-THIN LIMIT

BY

CAI MIKE WANG

DISSERTATION

Submitted in partial fulfillment of the requirements
for the degree of Doctor of Philosophy in Mechanical Engineering
in the Graduate College of the
University of Illinois at Urbana-Champaign, 2018

Urbana, Illinois

Doctoral Committee:

Assistant Professor SungWoo Nam, Chair and Director of Research
Professor M. Taher A. Saif
Professor Joseph W. Lyding
Professor Catherine J. Murphy
Research Assistant Professor Glennys A. Mensing

ABSTRACT

Two-dimensional (2D) layered materials, exemplified by the prototypical graphene, have been intensively studied for their diverse material properties and superlative mechanical strength. Due to their atomically-thin nature, weak basal plane van der Waals interactions, and vanishing bending stiffness, 2D materials are extremely flexible and thus susceptible to mechanical instabilities that result in deformed out-of-plane morphologies. Such unique combination of material properties and mechanical anisotropy presents new scientific and practical challenges, but also enables novel opportunities in the nanomanufacture of 2D materials and of their derivative materials systems and devices.

Surface instabilities (e.g. wrinkling and buckling) and interfacial phenomena (e.g. delamination) are typically deemed as engineering nuisances and failure modes. However, these universally ubiquitous phenomena can instead be harnessed to realize novel strategies and architectures for precise manipulation and assembly of 2D and other low-dimensional nanoscale materials, the combination of which contributes to an ever-growing toolset of capabilities towards layer-by-layer nanomanufacturing at the atomically-thin limit.

This dissertation details new methods that have been developed to deterministically create hierarchical and deformed 2D materials via large-scale elastic strain engineering and controlled shape memory deformation. The emergent tunable 3D architectures arising from flat 2D materials exhibit large-scale, uniform, and well-organized patterns with characteristic length scales spanning from tens of nanometers to few microns without any *a priori* patterning or lithographic definition of the constituent sub-nanometer 2D thin films.

By controlling bulk substrate deformation, this highly robust and scalable process imparts spatially heterogeneous strain gradients that perturb the intrinsic lattice structure and consequently the local optoelectronic properties of atomically-thin monolayer graphene analogs such as semiconducting transition metal chalcogenides, thus creating highly uniform and periodic lateral superlattice configurations. In addition, the generality of this self-patterning scheme allows for facile and scalable definition of nanoscale architectures for template guided nano-convective/capillary self-assembly of arbitrary 0D/1D nanoparticles onto deformed 2D substrates. Here, high quality colloidally prepared gold nanoparticles of diverse shapes and sizes readily self-assemble into various tunable structured mixed-dimensional metamaterials, opening the opportunity to investigate emergent phenomena such as those arising from coupling between metallic plasmonic nanostructures/nanoparticles with excitons and other quasiparticles in 2D materials.

Finally, with the eventual goal towards large-scale nano-manufacturing of these 2D materials and devices, a new technique has been developed to cleanly and sustainably manufacture graphene and recycle the catalyst metal substrate using benign materials. By separating the 2D material from the growth substrate via electrochemical interfacial delamination, this method forgoes the harsh chemicals typically used in conventional processing of 2D materials while simultaneously avoiding expenditure of the expensive precursors, thus leading to scalable production of high quality, clean graphene with reduced negative externalities.

ACKNOWLEDGEMENTS

It feels like only last week did I submit my GRE scores to this school with an awkward four-lettered acronym whilst cramming for midterm exams in the sunny halls of Gerstein Library. Yet, it's been almost six years. In many ways, it seems nothing has changed, but everything has.

I owe my utmost gratitude to so many mentors and teachers throughout these past twenty-three plus years of schooling. Each in their own unique and impactful ways, these amazing educators exuded the joys of teaching and slowly guided me onto this path of academia. I owe my inspiration and intrigue in those formative years especially to Mr. Ron Avery, Mr. Andrew Wong, Mr. Joe Rutherford, Mr. John Shim, and so many others. Without the support and encouragement from Prof. Bryan Karney, Prof. Joseph Paradi, Dr. Judy Favolden, Prof. Javad Mostaghimi, and Prof. Sanjeev Chandra, I would never have made it to (and through) Chambana. Many thanks to Prof. Xinlei Wang and the entire Solar Decathlon crew on both sides of the Pacific. Their energy, hospitality, passion, and shenanigans made those early days in Chambana that much more memorable and through whom I have made many life-long friends.

It has been my greatest fortunate to work with such a collegial and diligent cohort in Prof. SungWoo Nam's group. I learned so much from Jaehoon Bang, SungGyu Chun, Ali Ashraf, Pilgyu Kang, Jonghyun Choi, and Juyoung Leem. Ever since the arrival of Keong Yong and Peter Knapp (and especially their involvement in GRAMS), our lab has always been well fed. It has been so refreshing and insightful to work alongside our many new lab members over the years, including Farhad Haque, Chace Cho, Yerim Kim, Yeageun Lee, Zhichao Zhang, Jin Myung Kim, Saif Khan Alen, Hyung Jong Bae, Sunghwan Cho, and Keon-Hee Lim. I'm sure our group will be even more productive and prolific in the coming months and years with their new energy and drive.

I also owe my gratitude to Tasha Mamaril and Prof. Sue Larson. Without these two, I would have never had the privilege to work with such a cohort of bright and fun mentees through the ISUR program. It has been my utmost pride to see these budding engineers and scientists kickstart each of their own postgraduate ambitions: Brandon Paul Smith, Janna Eaves, Scott Zaeck, Mahmoud Fouly, Ryan Han, Advika Battini, David Lisk, Siddhesh Dhanawade, Satoshi Takekuma, Widi Moestopo, Thomas Stofko, William Sun, Patrick Burke, Zhuo Chen, and Ziran Zhou.

Many thanks to all the wonderful folks at MRL, MNTL, Beckman ITG, and Argonne CNM for putting up with my peculiar work schedules. My research would not have been possible without the help from Scott MacLaren, Kathy Walsh, Julio Soares, Rick Haasch, Edmond Chow, Yaguang Lian, David Gosztola, and many many others.

I will always be grateful to Prof. Glennys Mensing for letting me jump ahead of the MNMS training queue. I am so ever fortunate to have gotten to know Prof. Mark Shannon even if just for a few brief weeks, who exemplified what it means to dedicate one's life to science and education.

Many thanks to all the wonderful folks in MechSE for running such a tight show: Bill Bowman, Blake Johnson, Cliff Gulyash, Damon McFall, David Farrow, Emily Lange, Gary Sedberry, Holly Foster, Jeff Smith, Joe Maduzia, Joe Muskin, Julia Cation, Kathy Smith, Katrina Hagler, Kyle Cheek, Laurie Macadam, Pam Vanetta, Ralf Moller, Robbie Vermillion, Ruthie Lubkeman, Stacy Walker, Tammy Smith, and many many others. Kathy has been a motherly figure to the entire MechSE graduate student cohort, and an indispensable source of knowledge for (fur)children rearing.

It has been such a joy working with Matthew Thomas Gole, Wayne Lin, and Prof. Catherine Murphy. I am ever grateful for their enthusiasm and support for our collaborative research. I wish

I had gotten to know these guys earlier and also apologize to their significant others for texting them way too much (I promise it's all professional).

To my committee members, Prof. Taher Saif and Prof. Joe Lyding. It has been a pleasure being office neighbours with Prof. Saif's group and befriending many of them. Prof Saif has always been so resourceful every time I urgently needed some life advice, even if its sporadically in the halls of MEL. I am grateful for having the privilege of sneaking into Prof. Lyding's captivating lectures and thank him for providing the opportunity to collaborate with Dr. Gang Wang.

Many thanks to all my professors and MechSE faculty for their kind advice and reassuring nods in the hallway, especially Prof. Alison Dunn, Prof. Arend van der Zande, Prof. Ben Freund, Prof. Brian Thomas, Prof. Gabe Juarez, Prof. Gaurav Bahl, Prof. Harley Johnson, Prof. Iwona Jasiuk, Prof. Jian-Min Zuo, Prof. Kimani Toussaint, Prof. Liz Hsiao-Wecksler, Prof. Narayana Aluru, Prof. Nenad Miljkovic, Prof. Pinshane Huang, Prof. Sam Tawfick, Prof. Seok Kim, Prof. Wenjuan Zhu, Prof. Xiuling Li, Prof. Yuhang Hu, and many many others.

It has been the luck of my life to have worked for such a prolific, dedicated, and tireless assistant professor as Prof. SungWoo Nam from day one. They say that imitation is the sincerest form of flattery, and I can only hope to replicate if only a fraction of Prof. Nam's success. It is comforting to know that I can always count on Prof. Nam for a lifetime of advice and support as I start my own independent career.

To my boys back in the 6 (both 416 and 604, that is), thanks for always checking up on me and for the constant and timely comic relief. There's a lot of accumulated FOMO after all these years which will necessitate retroactive fulfillment pronto.

Words cannot express my gratitude to my parents and my wife for their incredible patience and confidence throughout this journey. But be forewarned…those endless days and nights in the lab are just beginning!

I-L-L!

To our grandmas, and their unconditional love

Table of Contents

Chapter 1. Introduction

This chapter is adopted in part from work published in *2D Materials*, **15 (3)**, 1829-1835 (2018).

1.1. Mechanical instabilities in two-dimensional materials

Two-dimensional (2D) materials exhibit diverse and impressive properties, superlative mechanical strength, and possess vast potential as a diverse library of materials for layer-by-layer additive nano-manufacturing at the atomically-thin limit. Graphene, as the prototypical 2D material that constitutes the ubiquitous graphite, has captivated the scientific community for decades, initially for its ultimate atomic thinness,[1] ostensible flatness, and "all surface" nature. As a two-dimensional crystal arranged in a hexagonal lattice, graphene also forms the basis for other carbon allotropes, including carbon nanotube (CNT) and buckyballs, may be conceptualized as bending graphene in different chiral directions.[2]

While graphene has been touted for its enormous in-plane stiffness of 1 TPa [3–5] and large intrinsic tensile strength of ~100 GPa,[6–9] its atomic thinness (and thus extremely low bending rigidity) and weak van der Waals (vdW) basal plane interactions dictate that graphene and its ever expanding family of 2D analogs are intrinsically "floppy". Such large anisotropy in the mechanical properties of 2D materials lead to out-of-plane morphologies and topological defects to minimize their total deformation energy in response to mechanical and other stresses or stimuli. These ubiquitous instabilities and morphologies come in various configurations and have been given a multitude of colourful names including: buckling, creases, crinkles, delamination, folds, rippling, ripplocations, rugas, scrolls, wrinkling, etc.

These non-linear complex deformations in atomically-thin 2D materials result from mechanical stresses due to suspension,[10,11] in-plane deformation,[12–15] shear,[16–18] anisotropic, graded or local

tension,[19] etc. Such nano and micron scale deformations are often unavoidable during their preparation and handling and have conventionally been treated as nuisances and artifacts. This thesis attempts to elucidate some of their significant influence on a plethora of material properties due to the unique morphology, coupled physical phenomena arising from heterogeneous strain, and methods to control such morphology for a variety of interesting effects and applications.

Conventionally, methods to alter the properties of 2D materials, such as via electrostatic gating, chemical functionalization, lithographic (subtractive) patterning, formation of heterostructures, etc. are often permanent (irreversibly changes the structure or chemistry of the material) and homogeneous throughout the entire material. Phenomenological changes in 2D materials caused by deformation and strain uniquely allow for tunability and reconstruction of various morphologies and properties that span from the nano to the micron scale. Such elastic deformations also allow for facile restoration of the original "planar" configuration. This versatile capacity to readily reconfigure the material via elastic deformations leads to a variety interesting applications in tunable surfaces and devices, stretchable electronics, enhanced catalysis, bio-interfaces, and energy storage.

1.2. Ubiquity of instabilities and heterogeneous deformations in 2D materials

Due to their atom thinness, bending and wrinkling of 2D materials are inevitably introduced during materials synthesis, handling, and subsequent processing.[20–22] For example, as graphene or other 2D materials are grown on catalytic substrates via CVD, wrinkles are formed on the metal catalyst substrates (Cu, Ni, Co, etc.) which grow and aggregate during cooling process due to thermal mismatch.[23–25] Particularly, wrinkles formed on terraces tend to be wider and shorter than those on step edges, which make the crystalline structure of the underlying growth substrate critical to the final morphology.[26]

Any practical application of 2D materials also requires their transfer from the synthesis substrate to another surface. This inevitably leads to the formation of wrinkles, especially with transfer onto hydrophilic substrates, where the drainage of residual water (from the aqueous transfer solution) drives wrinkle formation and controls wrinkle orientation via any existing surface topography. The spontaneous formation of wrinkles in graphene may occur due to the removal of hydrostatic pressure after initial conformation to the inevitable atomic roughness of substrates.[27] However, it is found that wrinkles are absent when graphene is transferred onto hydrophobic surfaces, due to intercalation of water between the substrate and graphene/polymer handle layer during wet transfer.[28] As the graphene/polymer film contacts the substrate, pre-existing wrinkles act as drainage channels which remain as standing wrinkles after drying. Since thinner sheets have lower bending stiffness, as graphite film thickness decreases to the minimum possible thickness (approaches monolayer graphene), the wrinkles increase in density and decrease in height.

2D materials are almost always supported on relatively rigid or thick substrates (or at a liquid/air interface). When such substrate is deformed, the 2D material is subjected to a mismatch strain. When the mismatch strain reaches a critical compressive buckling strain, the elastic energy in the film overcomes that of the interfacial adhesion, leading to buckle delamination and/or lateral slipping. The introduction of elastomeric and deformable substrates allows for facile and large-scale synthesis of various types of out of plane morphologies. The most common and accessible method to induce surface wrinkles is by pre-straining an elastomer substrate and transferring the desired 2D material onto the substrate surface prior to releasing the prestrain.

As 2D materials are strongly influenced by their supporting substrates, the local decoupling effect from the substrate (due to delamination or suspension) resulting from out of plane morphologies strongly contribute to local changes in material behaviour.[29] These instability-driven morphologies

may be tuned and guided in their assembly by altering the 2D materials' flexural rigidity (thickness/number of layers), substrate modulus, chemical functionalization, intrinsic defects, surface/interfacial energy (metallic, oxides, viscoelastic layers, etc.), and by controlling the mechanical deformation regimes (simultaneous versus sequential uniaxial or biaxial deformation, etc).[30]

With wrinkled structures, the in-plane strains are highly spatially non-uniform due to elongation, rotation, and bending. While classical mechanics informs us that bending may be described in the semi-infinite case by simple beam/shell theory, the ultimate thinness of 2D materials requires definition of an effective material thickness $t = \sqrt{12K/E_{2D}}$,[1,31] where E_{2D} is the in-plane stiffness (N/m) and K is the bending stiffness (N·m). To connect such 2D relations to the bulk and quantitatively compare with macroscale materials, the intrinsic bulk Young's modulus of 2D materials is defined as $E_{3D} = E_{2D}/t$. The bending energy is defined as a normalized areal bending strain energy, where the total energy difference between the bent and flat sheet is divided by the nominal sheet area (meV/Å^2). Since the bending stiffness is non-linear and changes as a function of the applied deformation for large deformations, there is a large dispersion in the quoted bending stiffness of graphene in literature,[32–35] and shows the relative inaccuracy of the classical beam model for monolayer 2D materials under large deformations.

1.3. Deformation induced heterogeneous local effects in graphene

Much research has been devoted to the effect of tuning electronic properties of 2D materials via strain,[27,36] with specific focus on the effect of strain on the electronic band structure, effective mass, and Fermi energy/density of states. In addition, recent research shows the potential for other

emergent effects due to bending and inhomogeneous strain effects such as flexoelectricity (coupling between strain gradient and charge localization and polarization).[37,38]

As the prototypical 2D material, graphene is intrinsically semi-metallic. Electrical conductance across heterogeneous deformations such as graphene wrinkles is highly dependent on the orientation of the wrinkle relative to current flow and local morphology. Similarly, conductance through collapsed wrinkles is dictated by interlayer tunneling (across the basal plane) and exhibits strong anisotropy.[39] When the excess length of wrinkled graphene exceeds a certain threshold ($\sim 24(\kappa/2\beta)^{0.5} \sim 16$ nm) - where κ is the bending stiffness (1.4 eV for graphene) and β is the vdW binding energy (40 meV) - the excess length of graphene wrinkles tends to pinch together at the base and form a standing collapsed wrinkle.

An upper limit to the height of graphene wrinkles exists as out-of-plane features have a tendency to fold over into collapsed wrinkles. For example, this collapse may be elucidated in graphene by the relative intensities of the in-plane and out-of-plane Raman modes (e.g. G and 2D modes in graphene) as collapsed or folded graphene regions may be identified by the predictable increases in the G band with an increasing number of layers.

Large aspect-ratio single graphene wrinkles tend to fold over into a trilayer arrangement (with negligible hybridization).[39] This collapse results from the vdW binding between the basal planes dominating over the local elastic bending (up to bending angle of 180 degrees). Hall-bar measurements (at zero bias) showed that the resistance along the wrinkles is smaller than across them (~9 kOhm·μm vs. ~12.5kOhm·μm). This anisotropy is attributed to the interlayer tunneling at the collapsed region, which bypasses the large resistance across the density of states bottleneck from the large curvature at the very apex of wrinkles. This basal-plane tunneling effect is further

substantiated by the relative independence of the folded region's resistance from the width or the height of a collapsed wrinkle (i.e. excess material length). This suggests that there may be some upper limit to the extent of wrinkle induced resistance for such morphologies. Nonetheless, these folded regions can also trap surface adsorbates and other impurities, which may act as dopants or scattering sources, further modulating the resistance. In addition, reduced doping/coupling due to detachment from the substrate (backgate) or screening of bottom layers in the case of collapsed wrinkles also present additional sources for unintentional electronic effects.

STM studies have shown that even with relatively low aspect ratio wrinkles (2-5 nm tall, 5-20 nm wide, and 0.1-1 μm long) (Figure 1.1a), local curvature induces a "three-for-six" triangular atomic pattern instead of the typically observed hexagonal graphene lattice, indicative of the broken six-fold symmetry (Figure 1.1b-c).[40] The local scanning tunneling spectroscopy (STS) on the wrinkle apex shows lower electrical conductance and emergence of midgap states, while the ubiquitous presence of small (~0.4 nm) intrinsic ripples was found both on the "flat" portions and also on the wrinkles. Due to local non-uniform strain, the observed triangular pattern is sustained over the entirety of the wrinkle, obscuring observation of the other three of the six carbon atoms in the hexagonal unit cell. The otherwise relatively planar hexagonal lattice takes on a chair/boat-like conformation similar to cyclohexane, where three of the carbon atoms pucker out of plane. Local tunneling conductance measurement to measure the local density of states (LDOS) on the wrinkles exhibits lower conductance for bias voltages within +/-0.2V, and the absence of the otherwise additional local conductance minimum at -0.12V bias, which suggests a finite DOS around the neutrality point.

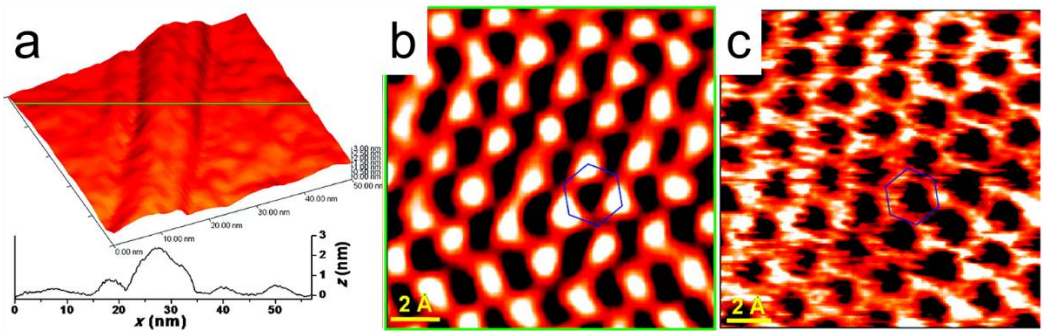

Figure 1.1. (a) STM topography image of wrinkled graphene shows (b-c) transition of the hexagonal carbon structure into a triangular pattern due to strain induced conformation change. Adapted with permission from reference 40. *Copyright 2009 American Chemical Society.*

Spatially-resolved STS studies (i.e., dI/dV transconductance mapping) of individual wrinkles by Lim *et al*. on as-grown graphene from Ni(111) substrates definitively showed the presence of bandgap opening and 1D van Hove singularities (Figure 1.2a-b).[26] The rapid cooling of the graphene immediately following chemical vapor deposition (CVD) synthesis induces the formation of wrinkles, especially on terraces that are few tens of nanometers in width. STS measurements show discrete local electronic states in the LDOS (two peaks on either the valence and conduction band sides), which were not present in the flat graphene regions in contact with the nickel growth substrate. STS mapping showed larger LDOS on the wrinkles for higher bias ranges, but lower conductance for small biases (due to metallic substrate effects), consistent with the findings by Xu *et al.*[40] This illustrates the metal-semiconductor-metal heterojunction nature of the wrinkle. The origin of conductance peaks is attributed to 1D electron confinement (resulting in discrete electronic states called van Hove singularities). Such confinement results in the inverse energy gap dependence on the wrinkle width (or arc length) (Figure 1.2c-d), akin to the bandgap variation effects seen in graphene nanoribbons [41] (GNRs) and semiconducting carbon nanotubes (CNTs).[42,43]

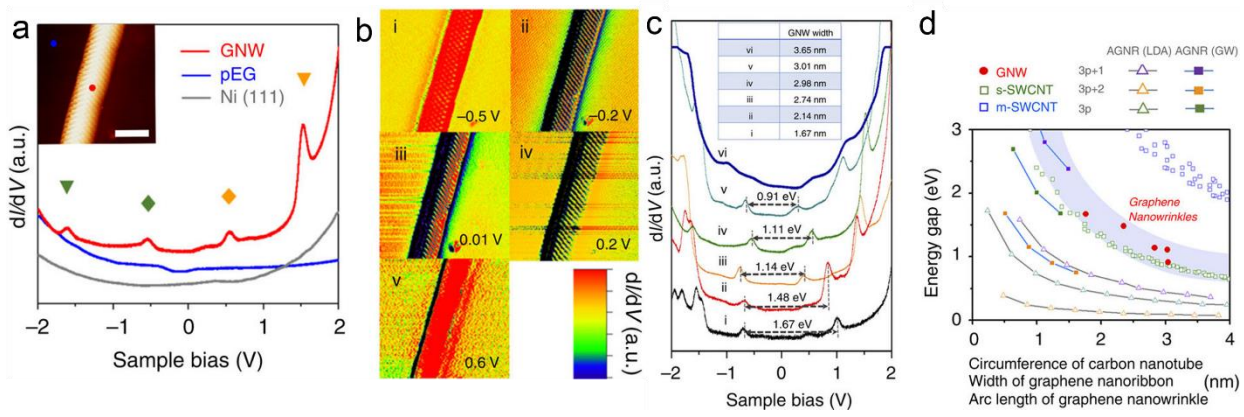

Figure 1.2. (a) STS spectra of graphene wrinkle (red), flat graphene (blue), and bare nickel substrate (grey) and (b) transconductance map of graphene wrinkle region under different biases. (c) dI/dV sweep for +/- 2V sample bias shows broadening of the energy gap in narrower graphene wrinkles, compared for reference with (d) the energy gap size dependence of GNRs and carbon nanotubes. Adapted from reference 26 *under Creative Commons CC-BY license.*

On the device level, Ozymilmaz *et al.* found that the presence of CVD induced wrinkles (~3 nm in height and ~10 nm wide) sets a lower bound for the anisotropic sheet resistance and upper bound for charge mobility.[44] This was characterized by investigating graphene field effect transistors (FETs) with source/drain (S/D) electrodes parallel and perpendicular to the ripples to measure conductivity and mobility. Such limits on the sheet resistance and mobility exist even if all other extrinsic scattering sources are removed, due to electron scattering from flexural/out-of-plane phonons and temperature dependent scattering from remote interfacial phonons.

Guo *et al.* studied the behaviour of wrinkled graphene nanoribbons subjected to charge injection and applied external electric fields (Figure 1.3a). Using density function theory (DFT), they found that increasing the GNR wrinkling aspect ratio (height to width) and the curvature decrease the local electron affinity and ionization potential (Figure 1.3c-d).[45] This enables the possibility of utilizing strained GNR as an efficient field-emission electron source where larger apex curvatures increase the local field enhancement (lower electron affinities and ionization potential).[46] As more

uniaxial compression is applied, the wrinkle height (h) increases while the wavelength and wrinkle width decrease (and the radius of curvature (r) also decreases) (Figure 1.3b), leading to increase in the field enhancement factor proportional to the ratio of h/r.

While the work function of GNR immediately decreases from 4.4 to 4.2 eV upon wrinkling, it does not continue to vary further with changes in wrinkle height, while both the electron affinity and ionization potential continue to decrease. This leads to an increased field emission efficiency (higher emission current and/or lower threshold voltage). When an external electric field is applied, the work function of graphene wrinkles is further decreased. The wrinkled graphene shows a more significant lowering of the work function for larger wrinkle aspect ratios (given the same bias), which results in even higher emission efficiency. Even larger bending curvatures induced by collapsed and folded wrinkles lead to lower work function, ionization potential, and electron affinity than standing wrinkles.[45]

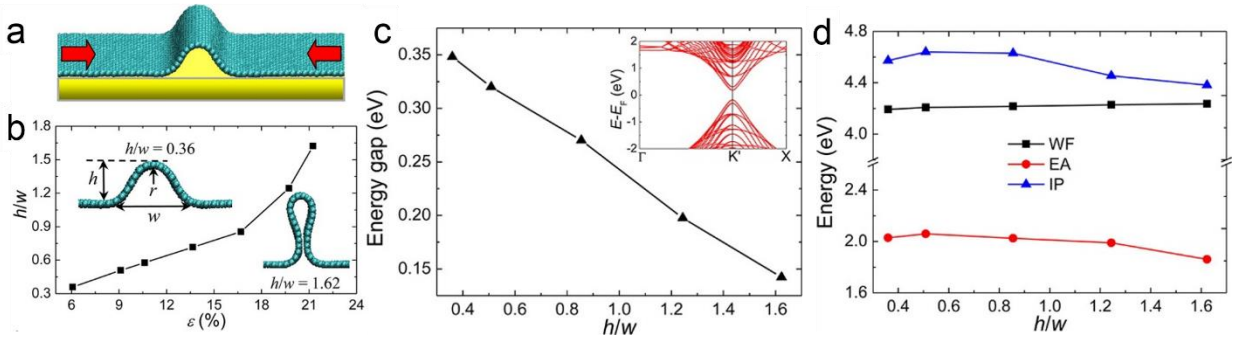

Figure 1.3 (a-b) Evolution of GNR wrinkle aspect ratio (height to width) as a function of uniaxial strain and the resultant redshift in (c) bandgap, (d) ionization potential, and electron affinity. (c) The bandgap decreases for larger aspect ratios along with (d) slight decreases for the ionization potential and electron affinity. The work function stays relatively constant for various aspect ratios. Adapted with permission from reference 45*. Copyright 2012 American Chemical Society.*

Due to the small scale of such deformations (sub-micron), which are approaching or below the diffraction limit, Raman spectroscopy, transmission electron microscopy (TEM), and scanning

probe techniques such as scanning tunneling microscopy (STM) form the basis for quantitative (and complementary) measurements to determine the spatial and temporal strain states of strained 2D materials.[47] Of these techniques, Raman spectroscopy is the most accessible and least intensive in terms of sample preparation. Using diffraction limited Raman spectroscopy, local plane strain states may be related to changes in the characteristic Raman peaks via the Guneisen parameter.[48] For example, in graphene and transition metal chalcogenides (TMDCs), the doubly-degenerate G phonon peak redshifts then splits due to breaking of the E_{2g} phonon symmetry when positive uniaxial strain exceeds a threshold value. Quantitative estimates of the interfacial energy between graphene (and other 2D materials or thin films in general) and their substrates may be obtained from the critical buckle delamination strain.[49] This critical compressive strain is measured by determining the maximum blue-shift/split of the G peak (due to in-plane compression). After the critical compressive strain is reached, slippage and wrinkling and/or buckling induced delamination will allow for heterogeneous strain relaxation and a redshift of the averaged Raman spectra back to the original peak positions.[50] Similar strain (in tension) relaxation phenomena (red-shift then sudden blue-shift in the Raman spectra) due to in-plane slippage have been observed for MoS_2 terrace structures under tension.[51]

1.4. Overview of the thesis

This dissertation presents new methods to manipulate surface instabilities especially in a scalable manner, and elucidates some interesting phenomena uniquely enabled by these structures. Contrary to conventional wisdom, the deterministic control of these features has great implications for the local and overall material properties due to heterogeneous distribution of stresses and strains. We explore the mechanisms behind these instability-driven morphologies and their emergent phenomena. Of particular interest are the deformation mechanics and ramifications of

such “floppy” 2D materials, including how morphological changes as a result of such stresses alter the various coupled material properties, and the mechanistic pathways to manipulate them deterministically.

As a prerequisite to the accessibility and adoption of 2D materials, the speed, cost, and quality at which they can be manufactured will be paramount. In Chapter 2, a more sustainable and clean method to scalable manufacture graphene is presented. This new process isolates graphene via electrochemical using carbon dioxide (CO_2) in the form of benign carbonic acid as the electrolyte solution as opposed to expending the catalyst metal via chemical etching.

Presented in Chapter 3 is a single-step strategy to achieve multi-scale, heterogeneous architecturing of graphene via their buckling delamination on shape-memory polymer substrates. The use of thermally activated substrates also enables the unique capability to selectively pattern crumples from otherwise flat graphene and graphene/graphite in a localized manner by using a focused infrared (IR) source to induce local heating and contraction. The thermoplastic nature of the substrate also confers the ability to mold the substrate onto arbitrary 3D surfaces while maintaining graphene’s conductivity. This enables the development of adaptive and ubiquitous electronics, as demonstrated by the fabrication of a highly aligned, wrinkled graphene FET device.

By expanding the length scales of deformed features through conformal wrinkling techniques, in Chapter 4 we show robust elastic strain engineering of monolayer TMDCs. Here, the atomically-thin semiconductor is tailored into various superlattice morphologies, which exhibit highly uniform, periodic tuning of its electronic band structure and vibrational properties. In addition, at the limits of highly uniform nanometer scale deformed features, we observed emergent linear dichroism in this otherwise highly symmetric material.

Finally in Chapter 5, a new paradigm towards scalable manufacturing of mix-dimensionality 0D/1D/2D nanomaterials via template guided convective/capillary self-assembly is presented. Here, a great variety of 0D nanospheres and 1D nanowires/nanotubes may be readily integrated into highly uniform nanoscale morphologies on the centimeter scale via topographical registration with deformed arbitrary 2D surfaces. This enables facile manufacturing of 0D/1D/2D metamaterials without the need for lithographic definition and allows investigation into novel plasmonic-exciton coupling phenomena with hybrid high-quality noble metal and 2D semiconducting nanostructures.

In addition to the results presented in this dissertation, an ever-expanding variety of exciting phenomena and applications arise from heterogeneous deformations in 2D materials. These include tunable surfaces and coatings, robust devices and electronics, adaptive optoelectronics, material toughening, energy storage, and chemical sensing. This new perspective on an otherwise nuisance thin-film phenomenon enables a new tool for future materials discovery, design, and synthesis with the ever-growing library of 2D atomically thin materials.

While this thesis focuses on the prototypical graphene and increasing so, TMDC materials, there is significant emerging interest in exploring the rich physics of the ever-growing genome of 2D materials. In addition to the vast literature surrounding graphene, there is much ongoing research in wrinkling and related effects surrounding other atomically thin materials such as graphene derivatives (graphane, graphyne, fluorographene, chlorographene, phagraphene, etc),[52–56] monoatomic 2D materials (also known as Xenes, e.g. germanene, phosphorene, silicene, etc),[57–61] diatomic 2D materials (hBN),[62] MXenes (2D metal carbides and nitrides),[63] TMDCs,[64,65] etc. There is a plethora of growing research activity and interest surrounding mechanical instability driven manipulation and architecturing of these diverse 2D materials and their respective emerging

applications in flexible electronics,[66–69] chemical sensing,[70] phase separation,[71] self-assembly,[72] novel actuators,[73] energy harvesting and storage,[74–77] and many others. The possibilities of tailoring novel materials based on 2D heterostructures combined with deterministic 3D morphologies expand the parameter space of materials design and application, making utility out of what was previously thought of as nuisance phenomena.[78]

1.5. Bibliography

(1) Huang, Y.; Wu, J.; Hwang, K. C. *Physical Review B* **2006**, *74*, 245413.

(2) Geim, A. K.; Novoselov, K. S. *Nature Materials* **2007**, *6*, 183–191.

(3) Zhao, Q.; Nardelli, M. B.; Bernholc, J. *Physical Review B* **2002**, *65*, 144105.

(4) Nardelli, M. B.; Yakobson, B. I.; Bernholc, J. *Physical Review Letters* **1998**, *81*, 4656–4659.

(5) Liu, F.; Ming, P.; Li, J. *Physical Review B* **2007**, *76*, 064120.

(6) Lee, C.; Wei, X.; Kysar, J. W.; Hone, J. *Science* **2008**, *321*, 385–388.

(7) Lee, G.-H.; Cooper, R. C.; An, S. J.; Lee, S.; van der Zande, A.; Petrone, N.; Hammerberg, A. G.; Lee, C.; Crawford, B.; Oliver, W.; Kysar, J. W.; Hone, J. *Science* **2013**, *340*, 1073–1076.

(8) Rasool, H. I.; Ophus, C.; Klug, W. S.; Zettl, A.; Gimzewski, J. K. *Nature Communications* **2013**, *4*, 2811.

(9) Zhang, P.; Ma, L.; Fan, F.; Zeng, Z.; Peng, C.; Loya, P. E.; Liu, Z.; Gong, Y.; Zhang, J.; Zhang, X.; Ajayan, P. M.; Zhu, T.; Lou, J. *Nature Communications* **2014**, *5*, 3782.

(10) Bao, W.; Miao, F.; Chen, Z.; Zhang, H.; Jang, W.; Dames, C.; Lau, C. N. *Nature Nanotechnology* **2009**, *4*, 562–566.

(11) Kirilenko, D. A.; Brunkov, P. N. *Ultramicroscopy* **2016**, *165*, 1–7.

(12) Wang, M. C.; Chun, S.; Han, R. S.; Ashraf, A.; Kang, P.; Nam, S. *Nano Letters* **2015**, *15*, 1829–1835.

(13) Leem, J.; Wang, M. C.; Kang, P.; Nam, S. *Nano Letters* **2015**, *15*, 7684–7690.

(14) Kang, P.; Wang, M. C.; Knapp, P. M.; Nam, S. *Advanced Materials* **2016**, *28*, 4639–4645.

(15) Lee, W.-K.; Kang, J.; Chen, K.-S.; Engel, C. J.; Jung, W.-B.; Rhee, D.; Hersam, M. C.; Odom, T. W. *Nano Letters* **2016**, *16*, 7121–7127.

(16) Min, K.; Aluru, N. R. *Applied Physics Letters* **2011**, *98*, 013113.

(17) Duan, W. H.; Gong, K.; Wang, Q. *Carbon* **2011**, *49*, 3107–3112.

(18) Qin, Z.; Taylor, M.; Hwang, M.; Bertoldi, K.; Buehler, M. J. *Nano Letters* **2014**, *14*, 6520–6525.

(19) Wang, C.; Lan, L.; Tan, H. *Physical Chemistry Chemical Physics* **2013**, *15*, 2764.

(20) Superfine, R.; Falvo, M. R.; Clary, G. J.; Taylor, R. M.; Chi, V.; Brooks, F. P.; Washburn, S. *Nature* **1997**, *389*, 582–584.

(21) Levy, N.; Burke, S. A.; Meaker, K. L.; Panlasigui, M.; Zettl, A.; Guinea, F.; Castro Neto, A. H.; Crommie, M. F. *Science* **2010**, *329*, 544–547.

(22) Morimatsu, M.; Mekhdjian, A. H.; Adhikari, A. S.; Dunn, A. R. *Nano Letters* **2013**, *13*, 3985–3989.

(23) Zhang, Z.; Mannix, A. J.; Hu, Z.; Kiraly, B.; Guisinger, N. P.; Hersam, M. C.; Yakobson, B. I. *Nano Letters* **2016**, *16*, 6622–6627.

(24) Sevik, C. *Physical Review B* **2014**, *89*, 035422.

(25) Chae, S. J.; Güneş, F.; Kim, K. K.; Kim, E. S.; Han, G. H.; Kim, S. M.; Shin, H.-J.; Yoon, S.-M.; Choi, J.-Y.; Park, M. H.; Yang, C. W.; Pribat, D.; Lee, Y. H. *Advanced Materials*

2009, *21*, 2328–2333.

(26) Lim, H.; Jung, J.; Ruoff, R. S.; Kim, Y. *Nature Communications* **2015**, *6*, 8601.

(27) Guinea, F.; Horovitz, B.; Le Doussal, P. *Solid State Communications* **2009**, *149*, 1140–1143.

(28) Calado, V. E.; Schneider, G. F.; Theulings, A. M. M. G.; Dekker, C.; Vandersypen, L. M. K. *Applied Physics Letters* **2012**, *101*, 103116.

(29) Locatelli, A.; Wang, C.; Africh, C.; Stojić, N.; Menteş, T. O.; Comelli, G.; Binggeli, N. *ACS Nano* **2013**, *7*, 6955–6963.

(30) Baimova, J. A.; Liu, B.; Zhou, K. *Letters on Materials* **2014**, *4*, 96–99.

(31) Yu, L.; Ruzsinszky, A.; Perdew, J. P. *Nano Letters* **2016**, *16*, 2444–2449.

(32) Cranford, S.; Sen, D.; Buehler, M. J. *Applied Physics Letters* **2009**, *95*, 123121.

(33) Lu, Q.; Huang, R. *International Journal of Applied Mechanics* **2009**, *01*, 443–467.

(34) Kudin, K. N.; Scuseria, G. E.; Yakobson, B. I. *Physical Review B* **2001**, *64*, 235406.

(35) Banhart, F.; Kotakoski, J.; Krasheninnikov, A. V. *ACS Nano* **2011**, *5*, 26–41.

(36) Castro Neto, A. H.; Guinea, F.; Peres, N. M. R.; Novoselov, K. S.; Geim, A. K. *Reviews of Modern Physics* **2009**, *81*, 109–162.

(37) Kvashnin, A. G.; Sorokin, P. B.; Yakobson, B. I. *The Journal of Physical Chemistry Letters* **2015**, *6*, 2740–2744.

(38) Krichen, S.; Sharma, P. *Journal of Applied Mechanics* **2016**, *83*, 030801.

(39) Zhu, W.; Low, T.; Perebeinos, V.; Bol, A. A.; Zhu, Y.; Yan, H.; Tersoff, J.; Avouris, P. *Nano Letters* **2012**, *12*, 3431–3436.

(40) Xu, K.; Cao, P.; Heath, J. R. *Nano Letters* **2009**, *9*, 4446–4451.

(41) Barone, V.; Hod, O.; Scuseria, G. E. *Nano Letters* **2006**, *6*, 2748–2754.

(42) Weisman, R. B.; Bachilo, S. M. *Nano Letters* **2003**, *3*, 1235–1238.

(43) Arnold, M. S.; Green, A. A.; Hulvat, J. F.; Stupp, S. I.; Hersam, M. C. *Nature Nanotechnology* **2006**, *1*, 60–65.

(44) Ni, G.-X.; Zheng, Y.; Bae, S.; Kim, H. R.; Pachoud, A.; Kim, Y. S.; Tan, C.-L.; Im, D.; Ahn, J.-H.; Hong, B. H.; Özyilmaz, B. *ACS Nano* **2012**, *6*, 1158–1164.

(45) Guo, Y.; Guo, W. *The Journal of Physical Chemistry C* **2013**, *117*, 692–696.

(46) Ye, D.; Moussa, S.; Ferguson, J. D.; Baski, A. A.; El-Shall, M. S. *Nano Letters* **2012**, *12*, 1265–1268.

(47) Ortolani, L.; Cadelano, E.; Veronese, G. P.; Degli Esposti Boschi, C.; Snoeck, E.; Colombo, L.; Morandi, V. *Nano Letters* **2012**, *12*, 5207–5212.

(48) Ni, Z. H.; Yu, T.; Lu, Y. H.; Wang, Y. Y.; Feng, Y. P.; Shen, Z. X. *ACS Nano* **2008**, *2*, 2301–2305.

(49) Brennan, C. J.; Nguyen, J.; Yu, E. T.; Lu, N. *Advanced Materials Interfaces* **2015**, *2*, 1500176.

(50) Jiang, T.; Huang, R.; Zhu, Y. *Advanced Functional Materials* **2013**, *24*, 396–402.

(51) McCreary, A.; Ghosh, R.; Amani, M.; Wang, J.; Duerloo, K.-A. N.; Sharma, A.; Jarvis, K.;

Reed, E. J.; Dongare, A. M.; Banerjee, S. K.; Terrones, M.; Namburu, R. R.; Dubey, M. *ACS Nano* **2016**, *10*, 3186–3197.

(52) Si, C.; Sun, Z.; Liu, F. *Nanoscale* **2016**, *8*, 3207–3217.

(53) Wang, Z.; Zhou, X.-F.; Zhang, X.; Zhu, Q.; Dong, H.; Zhao, M.; Oganov, A. R. *Nano Letters* **2015**, *15*, 6182–6186.

(54) Bissett, M. A.; Tsuji, M.; Ago, H. *Physical Chemistry Chemical Physics* **2014**, *16*, 11124.

(55) Naumis, G. G.; Barraza-Lopez, S.; Oliva-Leyva, M.; Terrones, H. **2016**.

(56) Zhang, Z.; Liu, X.; Yu, J.; Hang, Y.; Li, Y.; Guo, Y.; Xu, Y.; Sun, X.; Zhou, J.; Guo, W. *Wiley Interdisciplinary Reviews: Computational Molecular Science* **2016**, *6*, 324–350.

(57) Kistanov, A. A.; Cai, Y.; Zhou, K.; Dmitriev, S. V.; Zhang, Y.-W. *The Journal of Physical Chemistry C* **2016**, *120*, 6876–6884.

(58) Li, Y.; Wei, Z.; Li, J. *Applied Physics Letters* **2015**, *107*, 112103.

(59) Quereda, J.; San-Jose, P.; Parente, V.; Vaquero-Garzon, L.; Molina-Mendoza, A. J.; Agraït, N.; Rubio-Bollinger, G.; Guinea, F.; Roldán, R.; Castellanos-Gomez, A. *Nano Letters* **2016**, *16*, 2931–2937.

(60) Zhou, Y.; Yang, L.; Zu, X.; Gao, F. *Nanoscale* **2016**, *8*, 11827–11833.

(61) Cahangirov, S.; Sahin, H.; Le Lay, G.; Rubio, A. Springer International Publishing, 2017; pp. 87–96.

(62) Zhang, H. X.; Feng, P. X. *ACS Applied Materials & Interfaces* **2012**, *4*, 30.

(63) Anasori, B.; Lukatskaya, M. R.; Gogotsi, Y. *Nature Reviews Materials* **2017**, *2*, 16098.

(64) Roldán, R.; Castellanos-Gomez, A.; Cappelluti, E.; Guinea, F. *Journal of Physics: Condensed Matter* **2015**, *27*, 313201.

(65) Maniadaki, A. E.; Kopidakis, G.; Remediakis, I. N. *Solid State Communications* **2016**, *227*, 33–39.

(66) Cui, Y. *IEEE Transactions on Electron Devices* **2016**, *63*, 3372–3384.

(67) Lee, S.-M.; Kim, J.-H.; Ahn, J.-H. *Materials Today* **2015**, *18*, 336–344.

(68) Tang, J.; Guo, H.; Zhao, M.; Yang, J.; Tsoukalas, D.; Zhang, B.; Liu, J.; Xue, C.; Zhang, W. *Scientific Reports* **2015**, *5*, 16527.

(69) Donaldson, L. Wrinkles and folds could benefit flexible electronics. *Materials Today*, 2013, *16*.

(70) Schedin, F.; Geim, A. K.; Morozov, S. V.; Hill, E. W.; Blake, P.; Katsnelson, M. I.; Novoselov, K. S. *Nature Materials* **2007**, *6*, 652–655.

(71) Amadei, C. A.; Stein, I. Y.; Silverberg, G. J.; Wardle, B. L.; Vecitis, C. D. *Nanoscale* **2016**, *8*, 6783–6791.

(72) Wang, Z.; Tonderys, D.; Leggett, S. E.; Williams, E. K.; Kiani, M. T.; Spitz Steinberg, R.; Qiu, Y.; Wong, I. Y.; Hurt, R. H. *Carbon* **2016**, *97*, 14–24.

(73) Mu, J.; Hou, C.; Wang, G.; Wang, X.; Zhang, Q.; Li, Y.; Wang, H.; Zhu, M. *Advanced Materials* **2016**, *28*, 9491–9497.

(74) Luo, J.; Jang, H. D.; Huang, J. *ACS Nano* **2013**, *7*, 1464–1471.

(75) Jiang, J.-W. *Nanotechnology* **2016**, *27*, 405402.

(76) Zang, J.; Cao, C.; Feng, Y.; Liu, J.; Zhao, X. *Scientific Reports* **2014**, *4*, 6492.

(77) Lee, C.; Jo, E. H.; Kim, S. K.; Choi, J.-H.; Chang, H.; Jang, H. D. *Carbon* **2017**, *115*, 331–337.

(78) Koskinen, P. *Applied Physics Letters* **2014**, *104*, 101902.

Chapter 2. Clean and sustainable transfer of graphene and recycle of the copper substrate

The work presented in this chapter was published in *Journal of Materials Chemistry C,* 17 (3), 1756-1761 (2017).

2.1. Introduction

Graphene, the prototypical two-dimensional material, has been the subject of much interest and study for the past decade and more. Carbon dioxide, on the other hand, has gained infamy over global climate change concerns. In this chapter, we demonstrate an unlikely but useful marriage between these two ostensibly juxtaposing carbon-containing compounds.

Specifically, we address the challenges in sustainable graphene manufacturing by developing a new route for graphene transfer and reuse of the copper catalyst substrate via carbonic acid enabled electrochemical under-etching delamination. Electrochemical reduction of the cuprous oxide (Cu_2O) interlayer between the copper catalyst substrate and the chemical vapour deposition (CVD) synthesized surface layer graphene is achieved by using carbon dioxide as the precursor for making conductive carbonic acid electrolyte. This under-etching delamination approach to graphene transfer mitigates the conventional need for harsh chemical etchants that otherwise expends the copper catalyst.

This approach also removes the need for the concomitant multiple subsequent rinsing steps typically needed for chemical etching or delamination via salt/alkali-based electrolytes, thereby significantly reducing process water usage. In addition, we also show the application of using food-grade ethyl cellulose (EC) as the thin film handle layer for the transfer process. This inexpensive and environmentally benign alternative for polymeric thin film replaces the conventionally used high grade polymers that are typically solvated in harsh solvents. We expect our development to

enable more environmentally sustainable and cost-effective strategies for large-scale integration of graphene and analogous 2D materials and their devices, and to also generate new application streams for value added uses of industrially captured carbon dioxide.

2.2. Green nano-manufacturing of prototypical 2D material: graphene

As graphene and the ever growing family of two-dimensional (2D) materials move from the laboratory to large scale and high volume applications and production, there exists a critical need to improve their yield and manufacturability.[1] Aside from the synthesis quality and intrinsic crystallinity of 2D materials, the material properties and final device performance of such atomically thin materials are especially susceptible to cracks, voids, wrinkles and residues from polymer handle layers and etchant solutions. While there have been many techniques developed to synthesize and transfer the most prototypical and prolific 2D material, graphene, they almost all involve some use of harsh chemical etchants or strong organic solvents and require expenditure of the high purity metal catalyst.[2,3] In particular, recent progress on synthesis of large grain, epitaxial graphene on relatively expensive single crystal Cu (111) substrates urgently necessitates the conception of an efficient and clean method to reuse the high purity copper growth substrate.[4] An established technique to completely transfer and reuse the synthesis substrate is through electrochemical delamination.

The earliest works on delamination transfer of graphene were based on electrolysis induced hydrogen bubble delamination of poly(methyl methacrylate) (PMMA) supported graphene from the copper or platinum growth substrate biased as the cathode.[5,6] These and many other subsequent works all function on the basis of electrolysis-induced bubble generation at the cathode (i.e. underneath the delaminated or delaminating graphene) in the presence of a conductive aqueous

electrolyte (ionic solution) or bubble generation as a result of chemical etching.[7–14] While the bubbles assist with accelerating the delamination rate, they tend to damage the graphene during the delamination process and also trap bubbles underneath the graphene upon transfer (Figure 2.1), ultimately preventing conformal contact and complete coverage.

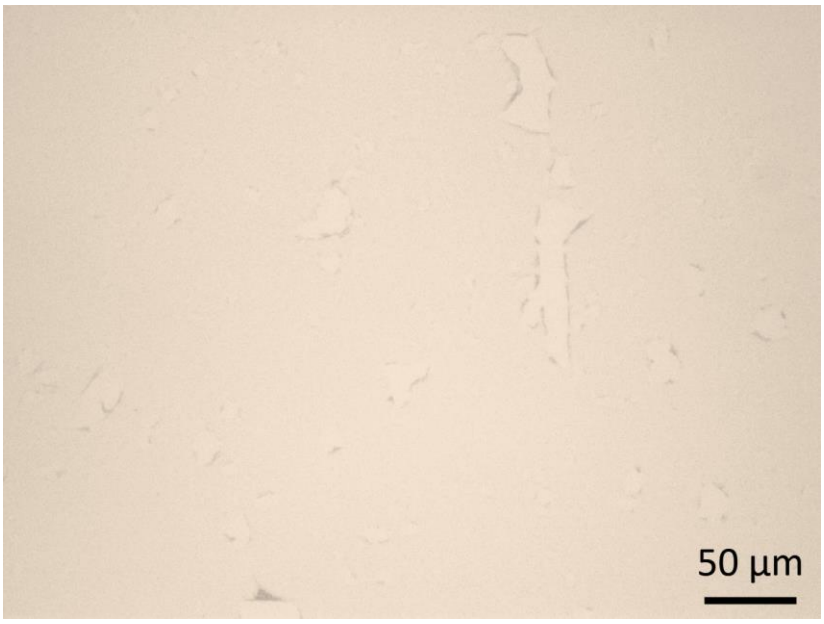

Figure 2.1. Optical microscope image of bubbling-damaged graphene with voids transferred onto SiO_2 via bubbling-delamination in 0.1M NaCl electrolyte.

One interesting strategy to mitigate cathode bubbling induced graphene degradation is to forego hydrolysis for electrochemical etching of the cuprous oxide (Cu_2O) under-layer that forms underneath the graphene.[15] While these delamination schemes are simple and prototypical of electrochemical setups, there remains challenges in terms of the need to completely remove the ionic contaminants due to the electrolyte residue. In addition, their requirement for a referenced three-terminal electrochemical arrangement increases their cost and complexity beyond the capabilities of many laboratory and manufacturing settings.

To rectify these aforementioned barriers to large scale manufacturability of high quality graphene, we propose a green chemistry route. Here we introduce an improved technique based on two-terminal under-etching electrochemical delamination that uses only weak carbonic acid as the electrolyte, inspired by the "bubble-free" delamination technique developed by Cherian et al.[15] The use of carbonic acid, which simply evaporates as water and dissolved carbon dioxide during the drying process after delamination, simplifies the transfer process into a single step compared with previous methods using salt or alkali based electrolytes such as NaCl or NaOH. The use of these conventional electrolytes necessitates the repeated rinsing and associated dwell time to dilute the chemical residue from underside of the graphene that in contact with the electrolyte solution. Often times, complete removal of chemical residue might not be possible. In using carbonic acid, on the other hand, the equilibrium reaction allows for the carbon dioxide to simply evaporate away with the water as the handle layer/graphene stack dries down and adheres to the target substrate.

2.3. Experimental procedure

Graphene was synthesized via low-pressure chemical vapour deposition (CVD; Rocky Mountain Vacuum Tech Inc.) on a 25 um thick 99.8% purity copper foil (Alfa Aesar). During the CVD process, the copper foil is ramped to 1050 °C within 45 mins and then held at 1050 °C for 1 hour of annealing under hydrogen. The synthesis step is completed for 2 mins where a 2:1 ratio of methane and hydrogen is introduced. After synthesis, the sample is left to cool slowly to room temperature inside the chamber under an argon flush. The details of the synthesis process were published previously.[16]

Carbonic acid was made via introducing carbon dioxide to fresh deionized (DI) water inside of a consumer-grade soda maker bottle (SodaStream). The source of the CO_2 was either via compressed

CO_2 gas (as per manufacturer recommended soda making procedure) or by simply adding fresh dry ice pellets (Continental Carbonic Products) into the bottle rinsed and then filled with DI water. Conductivities of the solutions were measured using a handheld conductivity meter (HM Digital).

To assist in delaminating the graphene from the copper surface via under-etching the Cu_2O layer (Figure 2.2, Figure 2.3), we first subject the as-synthesized graphene sample to a humidified environment (e.g., sealed inside a plastic bag with wet cleanroom wipes) to induce rapid oxidation of the copper substrate. The graphene samples are then coated with an EC (Sigma-Aldrich) handle layer film. A solution recipe of 2 wt% EC (46% ethoxyl content, standard 100,000 cps for 5% in 80/20 toluene-ethanol blend) solvated only in ethanol were spun-coated at 500 rpm for 90s. To prevent the unwanted backside graphene from contaminating the solution during transfer, the underside of the sample is subjected to a 30s oxygen plasma to remove the backside graphene.

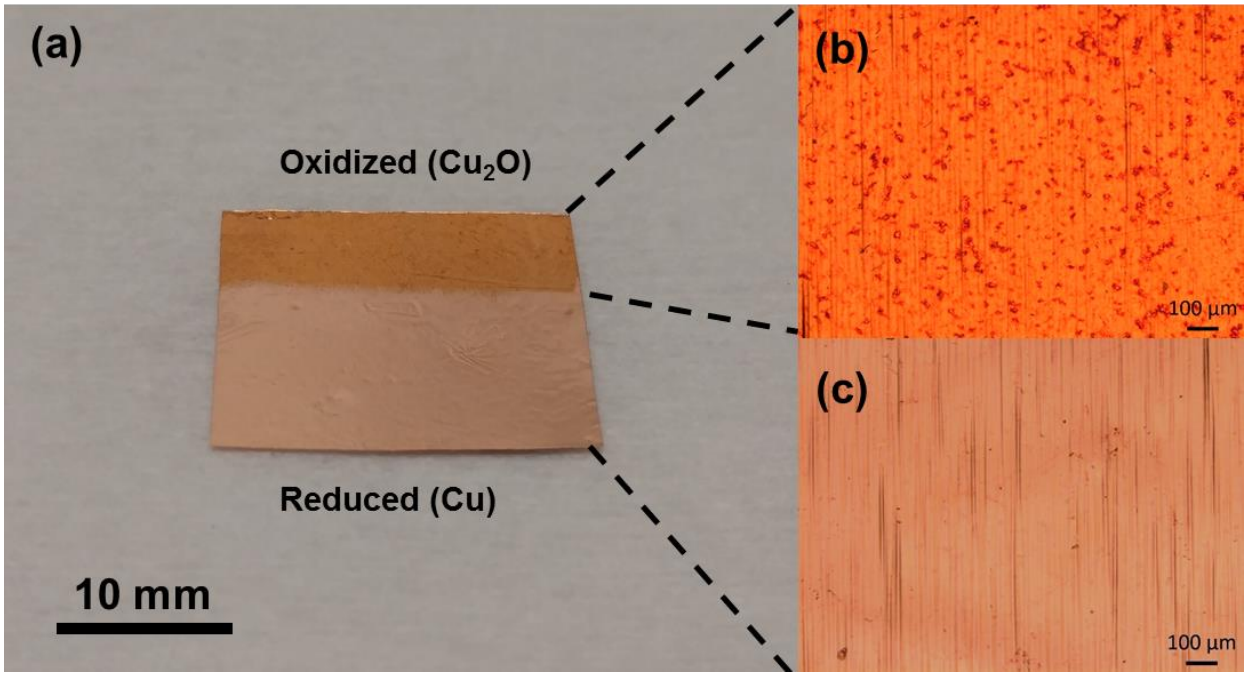

Figure 2.2. (a) Partially delaminated ethyl cellulose (EC)/graphene/copper sample showing interface between the (b) oxidized cuprous oxide surfaces (top) where the EC/graphene still remain and (c) the exposed/reduced native copper foil substrate (bottom) where the EC/graphene has been delaminated.

Two terminal electrochemical delamination was conducted either inside an open beaker or a custom-made vessel filled with freshly prepared carbonated DI water. Electrical contact between the copper foil and the negative terminal of the DC power supply (Circuit Specialists) is established by both mechanical contact and double sided Kapton tape to a strip of copper connected to the DC source. The foil is biased at ~10 V relative to a platinum electrode placed ~10 mm away. To initiate the under-etching process, it is advantageous to remove the spin-coat edge bead by trimming the leading edge and side edges of the sample to expose a clean interface where the solution can access the Cu_2O layer.

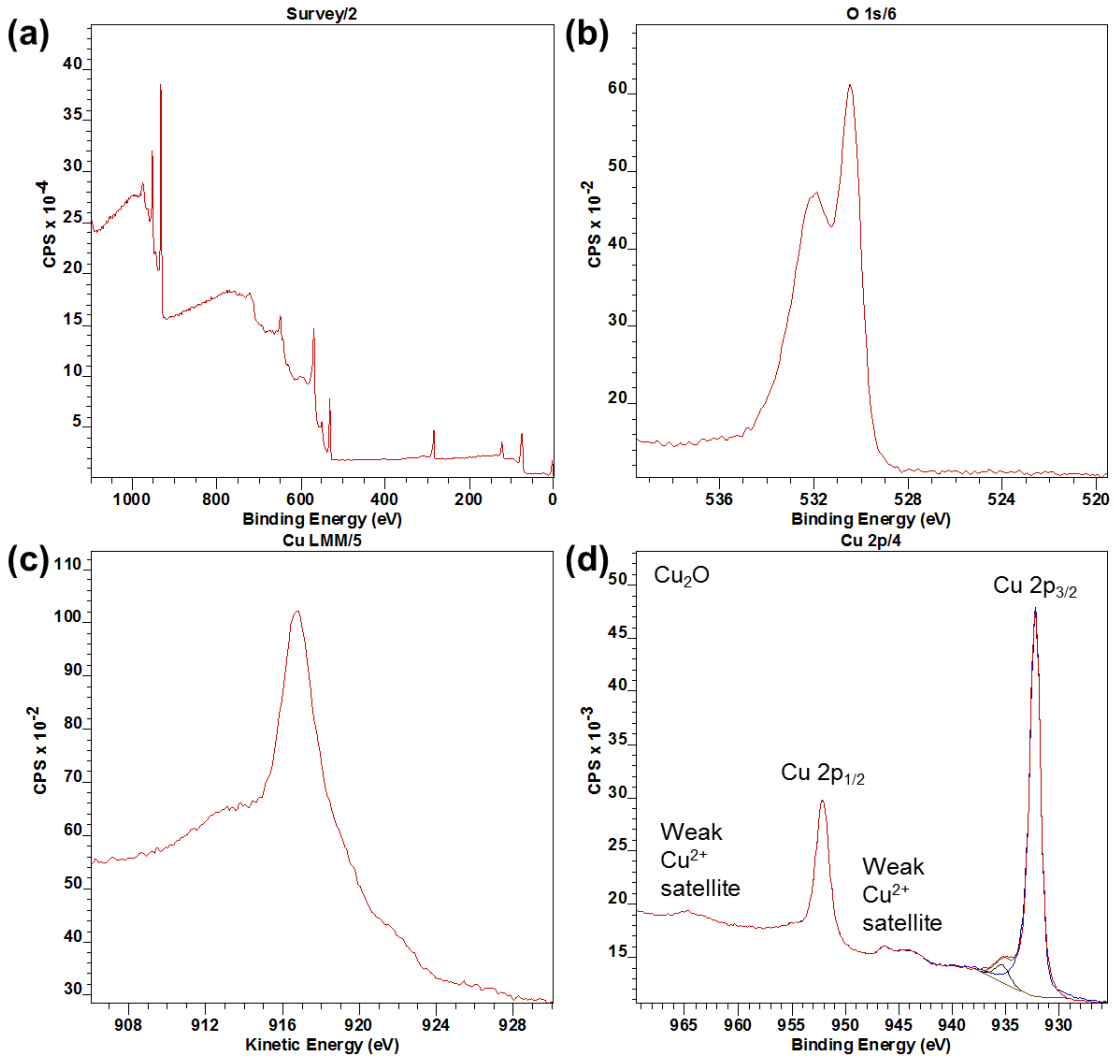

Figure 2.3. (a-d) XPS characterization of as-synthesized graphene on copper foil with Cu_2O interlayer due to ambient oxidation. The (c) Cu LMM peak position at less than 917 eV and (d) the weak Cu2+ satellites and narrow Cu $2p_{1/2}$ and Cu $2p_{3/2}$ peaks suggest that the oxide layer is predominantly Cu_2O rather than CuO.

The sample is lowered at a 45° angle into the carbonic acid solution and then progressively submerged further as the delamination progresses (~3 mins/mm). We chose the delamination angle to be at 45° so as to mitigate excessive bending of the EC/graphene layer at the delamination front, while providing a steep enough angle from the horizontal to easily visually monitor the delamination of the nearly transparent film from the periphery. Shallower angles (more horizontal)

can also be utilized, as it would provide sufficient buoyancy for the graphene/EC stack to float. However, shallower angles would make it more difficult to visualize regions of the sample that have been delaminated as the delaminated film would be very close to the copper substrate. In addition, from our experience, angles greater than ~60° tended to result in the sample breaking the surface tension of the solution, thus preventing graphene delamination when the sample is too vertical.

After the EC/graphene stack has fully delaminated from the graphene, the sample is either left idle in the solution as the carbonated solution is no longer effervescent or is picked up with a clean glass slide and then placed back into the solution to remove any large CO_2 bubbles. Finally, the EC/graphene stack is transferred onto a clean 285 nm SiO_2/Si wafer and left to dry. After the film has adhered to the wafer, it is placed inside a 100 °C oven for 10 mins to improve adhesion and to drive off interstitial water. Finally, the sample is rinsed in a covered warm ethanol bath (~50 °C for 2 minutes) to remove the EC handle layer and then immediately dried under dry nitrogen.

Samples transferred via conventional chemically etching of the copper foil and also NaCl delamination were prepared via CVD synthesis and spin-coated with EC handle layer in the same manner. Chemically etched samples were floated on top of a saturated sodium persulphate solution until the copper foil substrate was completely removed. Experiments conducted with NaCl (0.1M in DI water) were performed in the same manner as with carbonic acid delamination. Both chemically etched and NaCl delamination samples were transferred successively onto five baths of DI water (~20 mins dwell time for each rinse) to remove the chemical residue. The EC layers for chemically etched and NaCl delaminated samples are removed in the same manner as CO_2 delamination.

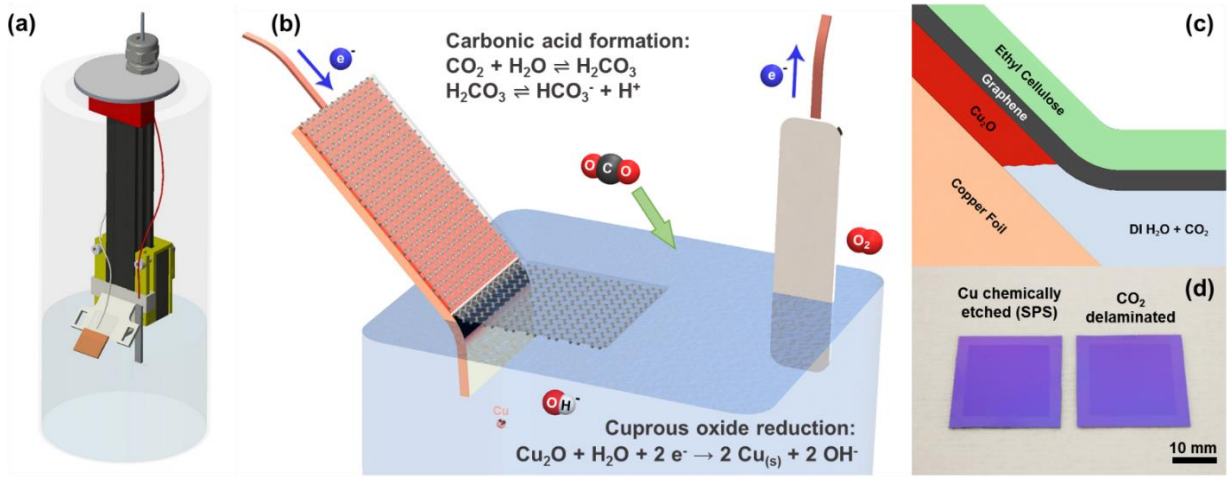

Figure 2.4. Schematic diagram and mechanism of cuprous oxide under-etch delamination of graphene in carbonic acid solution. (a) Self-pressurized vessel with contained vertical mechanism for (b) gradual immersion and delamination of EC coated graphene on copper foil into a carbonic acid solution. The copper foil substrate cathode is biased at ~10 V in a two terminal DC setup to allow for (c) under-etching of the cuprous oxide interlayer between graphene and the copper foil. (d) This setup is capable of transferring inch scale graphene without the use of any chemical etchants such as sodium persulphate (SPS) nor does the sample require subsequent rinsing in DI water.

The custom-built delamination vessel was fabricated from a combination of purchased and 3D printed parts (Figure 2.4a, Figure 2.5). The copper foil is attached onto an angled platform, which travels vertically on a plastic rail. A magnet is installed to a 3D printed carriage attachment where the platform sits, which allows for vertical actuation of the platform using another magnet from outside the vessel. The rail is attached onto the stainless steel sealing plate via two custom made plastic parts: one secured to the plate and the other to the rail to ease servicing and disassembly. A pressure-tight cord grip is attached through the plate to allow pass-through of the electrical wires. The sealing plate and a silicone seal are fixed to the vessel top by a screw-on collar. The body of the vessel itself is a typical, commercially available 64 oz. wide-mouth canning jar.

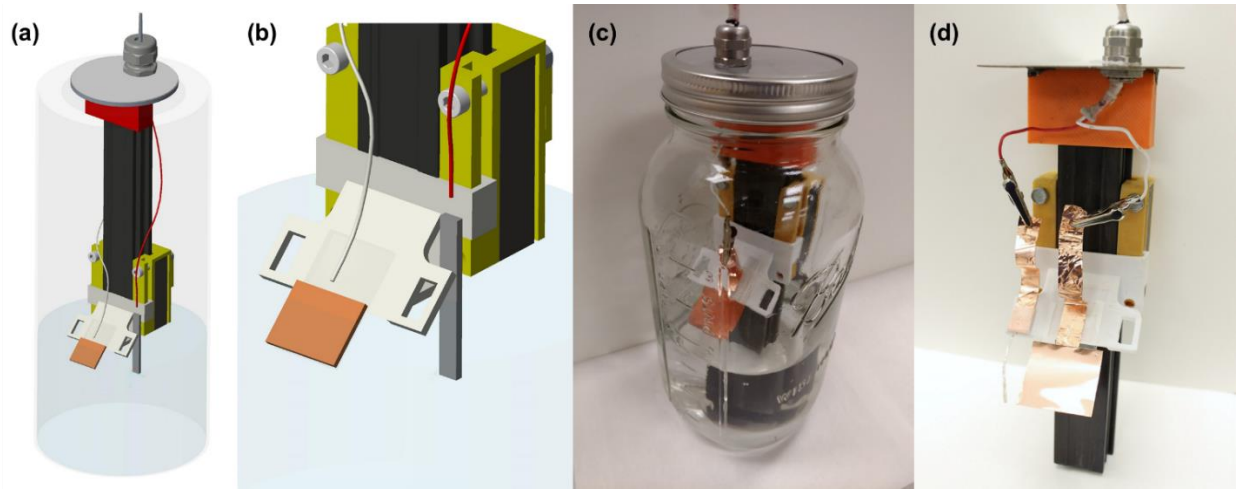

Figure 2.5. (a, b) Schematic renderings and (c, d) photos of pressured gradual immersion device for graphene delamination.

2.4. Materials characterization

Raman spectra were obtained with a 532 nm laser on Nanophoton Raman-11 instrument with a 600 grooves/mm grating. To obtain area averaged spectra (and to verify material uniformity), line scan xy_imaging mode was used with a 100x, 0.9NA objective lens to average over 25x25μm regions.

To characterize the amount of residual elements for each transfer technique, X-ray photoelectron spectroscopy (XPS) measurements were performed with a Kratos Axis Ultra X-ray photoelectron spectrometer (Kratos Analytical, Inc., Manchester, UK) using monochromatic Al Kα radiation (1486.6 eV). Survey spectra were collected using a pass energy of 160 eV and high-resolution spectra using a pass energy of 40 eV at a take-off angle of 90˚ from a 0.7 mm x 0.3 mm area using the hybrid (electrostatic and magnetic immersion) lens mode. Fresh samples were prepared and preserved in isopropanol before XPS measurement by affixing onto the sample holder using double-sided copper tape. The binding energy scale was referenced to the C 1s signal at 284.5 eV,

which originates from the graphene and also adventitious carbons (Figure 2.6). The pressure during analysis was ca. 7 x 10^{-7} Pa.

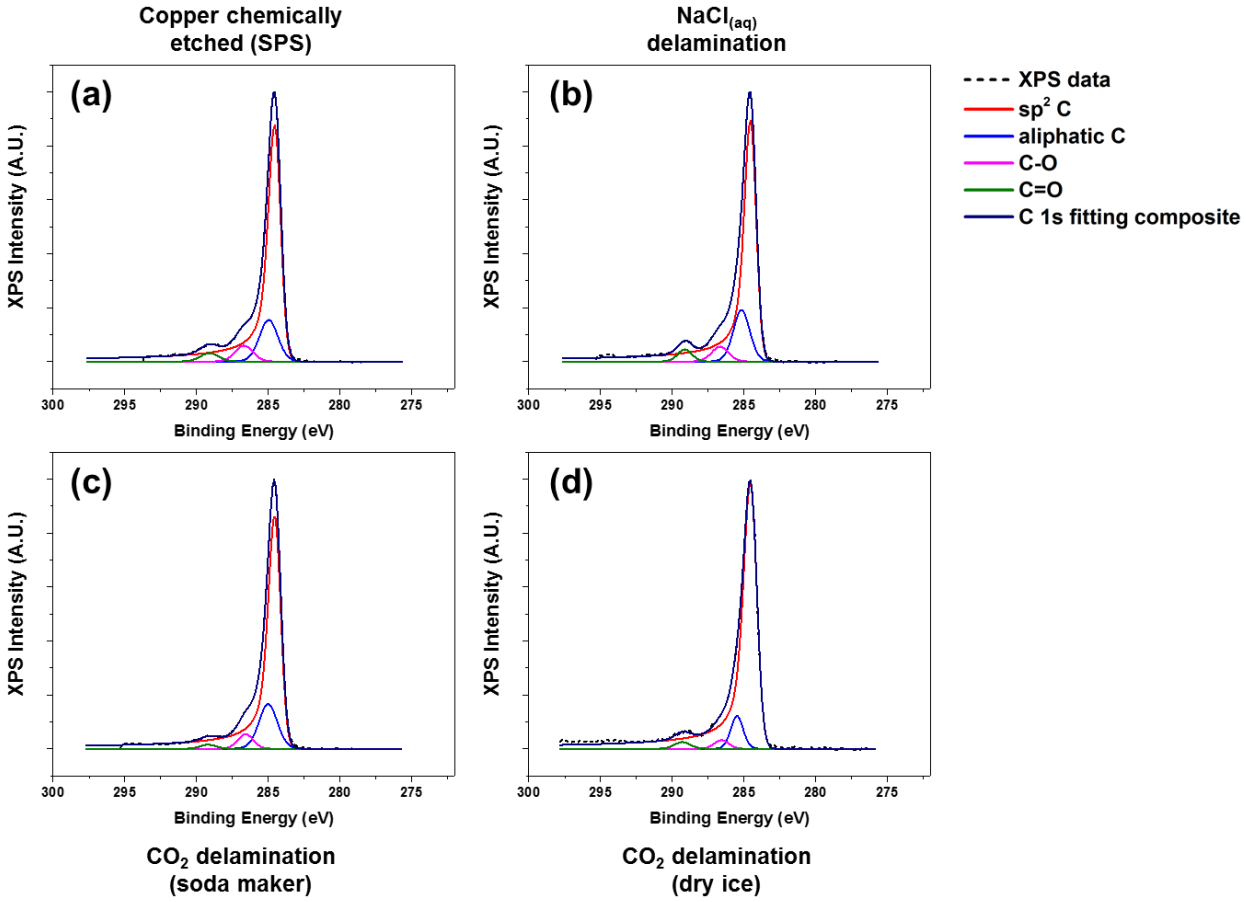

Figure 2.6. XPS characterizations of the C 1s peak indicative of graphene and adventitious carbon on the surface of SiO_2 wafer for graphene samples transferred via (a) sodium persulphate chemically etched copper, (b) 0.1M NaCl delamination, (c) CO_2 delamination carbonated with soda maker, and (d) CO_2 delamination carbonated with dry ice.

Atomic force microscopy (AFM) topography images were obtained in tapping mode on Asylum MFP-3D using TAP300AL-G tips (Budget Sensors). Copper foil roughness were extracted based on sampling four arbitrary regions on each copper foil each of 8100 μm^2 in planar area. The images were post-processed by first order flattening and the root mean square (RMS) roughness values were calculated in Igor.

2.5. Results and analysis

Inch scale electrochemical delamination transfer of as-grown graphene on copper foil was realized via (1) carbonic acid as the conductive electrolyte, (2) Cu_2O as the sacrificial under etch layer, and (3) EC transfer handle layer (Figure 2.4b,c). We opted for such an under-etch delamination scheme as opposed to the well documented bubbling delamination techniques reported by numerous groups due to the higher yield and less damage as compared to bubble delaminated graphene.[15] The suppression of bubbling reduces pore formation and fracture during the delamination process and also subsequently drying on substrate. In this study, standard 25 μm polycrystalline copper foils were used for graphene synthesis. However this under-etching technique can be easily extended to any copper or oxide forming substrate. Due to the expense of high purity copper and monocrystalline Cu (111) substrates which have been shown to yield high quality large grains of epitaxial graphene, this technique will prove useful in the reuse of these substrates as well.

To impart conductivity into the solution, we rely on the equilibrium between CO_2 and water hydration to form carbonic acid with a hydration constant of about 1.7E-3.[17–19] While it is a diprotic acid, the bicarbonate formation dominates over the carbonate formation by about three orders of magnitude (dissociation constants of 2.5E-4 and 4.47E-7 for bicarbonate and carbonate formations, respectively), resulting in the bicarbonate being the majority anion in the carbonic acid solution. The dissociation of bicarbonate (HCO_3^-) and hydronium (H^+) imparts conductivity to the otherwise highly resistive DI water and allows for the electrochemical reduction and under-etching of the Cu_2O layer to occur (Figure 2.4b,c). While the carbonic acid solution is not as conductive as other conventionally used salt and alkali electrolytes, its main advantage lies in being able to readily evaporate away as water and carbon dioxide subsequent to the graphene transfer and drying on a target substrate, leaving a completely clean interface.

To characterize the increase in solution conductivity due to carbonation, we performed several controlled measurements (Table 2.1). While fresh DI water measured a conductivity of only 0.1 μS, the addition of compressed CO_2 gas (using soda maker) and dry ice pellets (added directly to fresh DI water in the bottle) increased the conductivity to 72.8 μS and 71.9 μs respectively. To gauge the contribution of the conductivity due to the addition of CO_2 compared with the incorporation of ambient CO_2 (~0.04%), we agitated fresh DI water by repeatedly shaking vigorously and then letting fresh air into the bottle (~20 times). By this method of incorporating ambient CO_2 into the solution only increased the conductivity of DI water from 0.1 μS to 0.7 μS. These controlled experiments demonstrated the importance of additional CO_2 to impart conductivity into the carbonic acid solution that is significantly higher than that of incorporation of atmospheric CO_2 alone.

Table 2.1. Solution conductivities.

Solutions	**Conductivity (μS)**
Fresh DI water	0.1
Fresh DI water + vigorously shaken 20 times	0.7
0.1M NaCl in DI water	9650
DI water + soda maker	72.8
DI water + dry ice	71.9
DI water + dry ice + outgassed 48 hours	33.6
DI water + dry ice + vigorously shaken 20 times	20.9
DI water + dry ice + sonicated 10 minutes	41.2
DI water + dry ice + vigorously shaken 20 times + sonicated 10 minutes	19.8

Since the delamination process occurs over several minutes, it is important to gauge the level of conductivity changes in the carbonic acid over time and during delamination, we performed several additional controlled experiments. In particular, repeatedly shaking the bottle and venting the pressure (~20 times) lowered the conductivity to 20.9 μS from 71.9 μS. With the addition of 10 minutes sonication, the conductivity decreased further to 19.8 μS. However, when left

undisturbed (with the bottle cap opened) for 48 hours, the conductivity only dropped to 33.6 μS. As corroborated with successful delamination experiments using carbonated solutions that were left out for several hours, the relative stability of the solution conductivity allows for electrochemical delamination over long periods of time without having to replenish the solution. These conductivity measurements are tabulated in Table 2.1.

In addition to the specific detachment and transfer process of graphene from the growth substrate to target substrates, the selection of an appropriate and sacrificial handle layer is also critical to the final material quality and device performance.[20] This role has conventionally been served by high-grade polymers and photoresists such as PMMA, poly(bisphenol A carbonate) (PC), SU-8, thermal release tape, etc. While these specialized polymers have performed well in a research and development setting, their relative high cost and their form factor being dispersed in volatile aromatic and ketone solvents such as chlorobenzene, chloroform, anisole, etc. present environmental emissions, workplace health, and materials handling complications.

To find a more sustainable option for the graphene handle layer, we used a 2 wt% EC (a common polymer used in food additives and packaging, etc.) in ethanol as the spin-coat solution. We found an optimal film thickness (~700 nm) was achieved for 2 wt% EC in ethanol spun coated at 500 rpm for 90 s. Very thin EC films (and also PMMA) failed to have enough mechanical integrity to allow for a cohesive film of the handle layer adhered with the graphene to delaminate and did not provide a sufficient pulling force due to surface tension to progress the delamination front. However, too thick of a handle layer film also tends to prevent conformal contact to the target transfer and subsequent large-area transfer.

This EC handle layer film recipe ensures that the film is robust enough for manual handling and bending during the delamination process. The film should be sufficiently thick to be impermeable

to fracture against the occasional bubbles that form on the underside of the graphene due to CO_2 off-gassing. Simultaneously, the film needs to be sufficiently thin to conform to the target substrate after drying. Thinner EC films failed to initiate delamination while thicker EC films tended to not allow graphene to properly adhere to the SiO_2 substrate after drying. In addition to the cost and environmental advantages, the use of EC as an ethanol soluble polymer handle layer also makes this process compatible for transfer onto a variety of soft or polymeric substrates that would otherwise not tolerate many types of commonly used solvents (acetone, anisole, chlorobenzene, etc.).[21–25]

The electrochemical under-etching delaminations of graphene were performed in a two electrode setup using carbonic acid as the electrolyte. By biasing the graphene/Cu_2O/copper foil stack with a negative voltage relative to the platinum counter electrode, the Cu_2O layer between the graphene and copper foil is electrochemically reduced to metallic copper (Figure 2.4b,c).[26]

$$Cu_2O + H_2O + 2\ e^- \rightarrow Cu + 2\ OH^-$$

The anodic reaction that takes place at the platinum electrode is the oxidation of water.

$$2\ H_2O \rightarrow O_2 + 4\ H^+ + 4\ e^-$$

As the electrochemical delamination progresses over time, continuous reduction of cuprous oxide to copper at the cathode electrode gradually releases the graphene layer from the copper foil. In our experiments, complete delamination of graphene was achieved at a rate of about 3 mins/mm by applying a constant voltage of -10V to the cathode electrode. We note that higher bias voltages maybe applied to evolve hydrogen bubbles at the copper cathode to aid in the delamination process (Table 2.2), however these bubbles tend to damage the graphene by forming voids.

Table 2.2. Electrolytes type and applied voltages for various graphene delamination techniques

Authors	**Electrolyte**	**Applied voltage (cathodic)**	**Reference**
Y. Wang et al.	$K_2S_2O_8$ (0.05mM)	5V	5
L. Gao et al.	NaOH (1M)	5-15V	6
T. Ciuk et al.	NaCl/KCl (2mM-2M)	4-100V	12
X. Wang et al.	Na_2SO_4 (0.5M)	15V	7
C. Cherian et al.	NaCl (0.5M)	2.6V	15
Z. Zhan et al.	NaOH (0.2M)	8V	8
This work	Carbonic acid	7-10V	This work

To confirm the successful transfer of graphene onto the SiO_2 substrate (Figure 2.4d), we performed optical microscopy, scanning electron microscopy (SEM), and Raman spectroscopy. Bright field images (Figure 2.7a,b) showed the same level of metrology between graphene derived from carbonic acid delamination and chemically etching the copper, with negligible voids and defects, including at the graphene grain boundaries. From the SEM image (Figure 2.7c), it can be seen that the small size bilayer islands formed during CVD transferred monolithically with the monolayer regions and grain boundaries without any obvious defects. The Raman spectra (Figure 2.7d) averaged over 25 μm^2 show a 2D/G ratio of ~2, suggesting predominantly monolayer graphene, and a negligible amount of defects (D peak).[27] The three different Raman spectra between chemically etched copper, 0.1M NaCl delamination, and carbonic acid all showed similar spectral features and peak intensities.

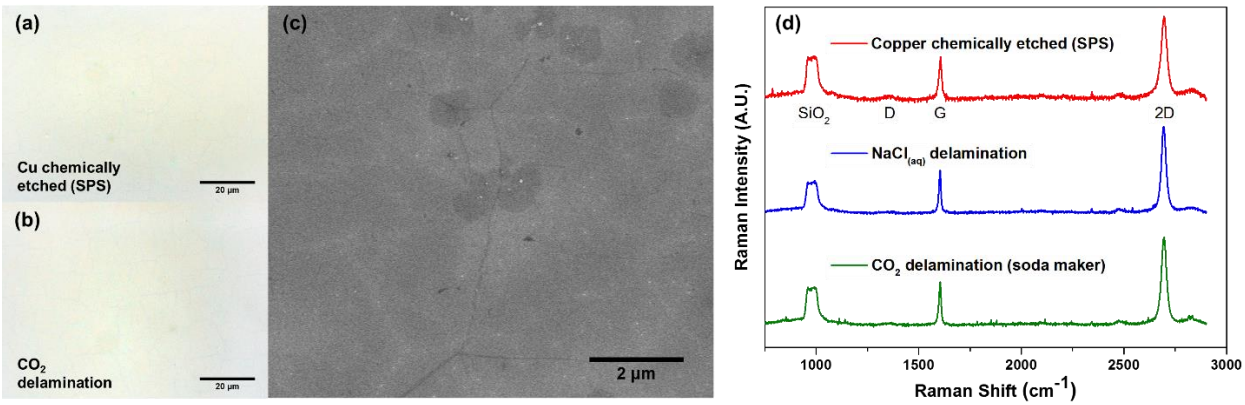

Figure 2.7. Optical microscopy, SEM and Raman spectroscopy characterization and comparison between chemical etching and delamination transferred graphene. Optical microscope images of (a) large area chemical etching (sodium persulphate) transferred and (b) carbonic acid delamination transferred graphene on SiO_2 substrate both show negligible voids and defects. (c) SEM image of carbonic acid delamination transferred graphene on SiO_2 substrate show that the under-etch delamination is independent of the graphene film thickness and allows for monolayer regions with bilayer islands to be transferred monolithically. (d) Raman spectra of graphene transferred using the different techniques (chemically etched (red), NaCl solution delaminated (blue), carbonic acid delaminated (green)) show the absence of any D peak and demonstrate good monolayer thickness uniformity from the area-averaged 2D/G peak ratio of ~2.

To further confirm the presence of graphene and also to assess the level of contamination between the various processes, we conducted XPS analysis of the as-transferred sample on 285 nm SiO_2/Si substrates. As expected, all of the samples (chemically etched via sodium persulphate, bubble delamination in 0.1M NaCl, and CO_2 delamination) showed characteristic carbon peaks around 285 eV (Figure 2.6) from the monolayer graphene as well as adventitious carbon. All of the samples showed an absence of copper signature in the XPS survey scans (Figure 2.8a), suggesting complete delamination and detachment from the copper substrate. The surveys are also absent of any characteristics peaks due to iron or chlorine, elements that are associated with conventional copper etchants for graphene transfer such as ammonium persulfate, sodium persulphate, ferric chloride, or hydrochloric acid.[28]

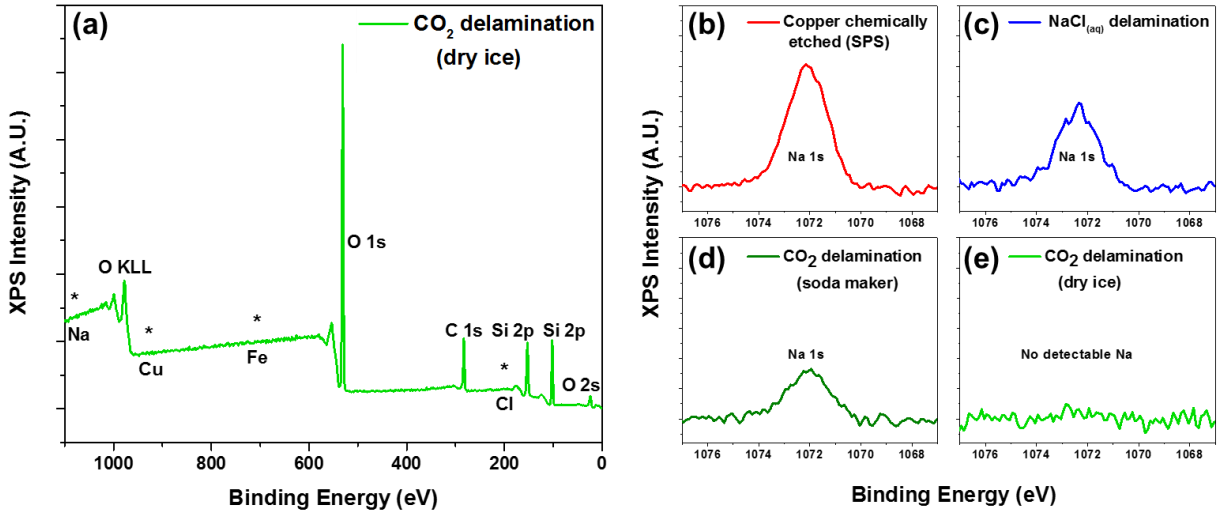

Figure 2.8. XPS characterizations of contaminants. (a) XPS survey of the CO_2 delamination (from dry ice) is absent of signatures from sodium, copper, iron, chlorine, or sulphur species associated with conventional chemical etching techniques. High resolution XPS spectra (b-e) indicate presence of sodium contamination in (b) chemically etched (sodium persulphate), (c) NaCl electrolyte delaminated, and also (d) CO_2 delaminated samples using compressed CO_2 from the soda maker. (e) Delaminations done using carbonic acid generated from dry ice pellets did not show any sodium residue in the XPS spectra.

Interestingly, only the dry ice derived carbonic acid delamination showed an absence of sodium in the XPS spectra. In spite of the repeated rinsing in DI water subsequent to chemically etching the copper foil or delamination using the 0.1 M NaCl solution, we still found presence of sodium in the XPS spectra (Figure 2.8b,c). Incidentally, we also found that regardless of the well-controlled processing condition and handle layer used, there were always the presence of sodium for graphene delaminated using carbonic acid derived from the commercially available gas canister. Conversely, the samples that were delaminated with carbonic acid derived from dry ice pellets did not yield any sodium residue detectable in the XPS (Figure 2.8d).

Thereafter, we have transitioned to solely using dry ice pellets for concerns about this aforementioned sodium contamination but also for its relatively lower cost. For approximate comparison, the gas canister costs $15 per refill at retailers enough to make 60 litres of carbonated

DI water whereas each litre of DI water requires only about ~20 g of dry ice (at ~$2/kg). A more ideal configuration of in-situ bubbling dry CO_2 is currently being developed to afford the convenience of using pressurized CO_2 gas (as opposed to dry ice) while mitigating the sodium contamination from these consumer product sources.

One of the most important aspects of graphene delamination is to reuse the copper catalyst substrate for repeated synthesis. After the EC/graphene stack has completely been delaminated from the copper foil, the surface is cleaned for the next iteration of synthesis and delamination. Once the copper foil surface has been completely reduced (i.e. only metallic copper remains on the surface after the delamination), it is cleaned in a warm ethanol bath. Finally, 30 s of oxygen plasma is applied to remove any remaining adsorbates or other polymeric contaminants during the rinsing process and to prepare the surface for the next CVD process. The subsequent graphene CVD processes are the same for every iteration of delamination and synthesis.

For each iteration of CVD synthesis and delamination, we verified the graphene quality with Raman spectroscopy and also characterized the morphological changes to the copper substrate (Figure 2.9). Due to the repeated annealing at high temperatures during CVD synthesis, subsequent surface oxidation to cuprous oxide, and reduction thereof, the surface becomes progressively smoother (from RMS roughness reduction from 181.56 nm to 58.89 nm after three cycles) (Figure 2.9a,b, Figure 2.10). In addition to the progressive smoothing of the machining striations on the copper foil during the vendor manufacturing process, the graphene quality remained constant with each iteration as with the initial growth as confirmed by Raman spectroscopy (Figure 2.9c). This demonstrates the capability to repeatedly reuse the copper foil substrate for successive re-synthesis and delamination transfer of graphene while maintaining the same level of material quality and operating conditions.

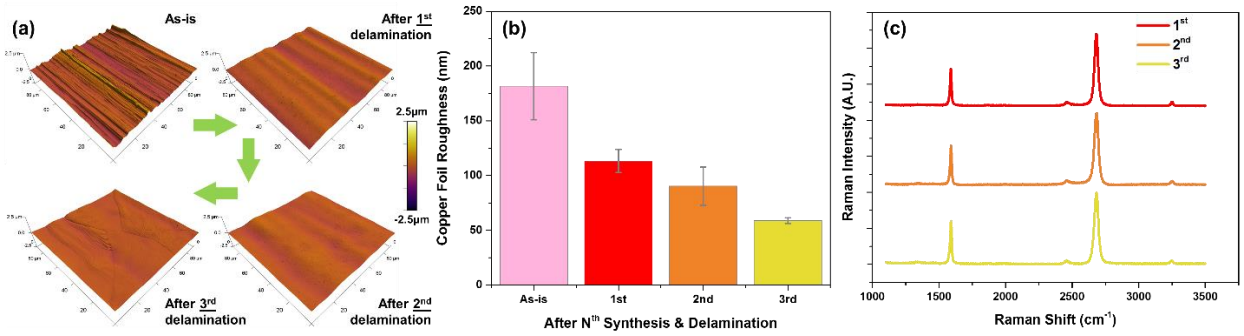

Figure 2.9. Iterative delamination and re-synthesis of graphene. (a) AFM topography images of the surface of the copper catalyst after successive graphene synthesis and delamination steps up to the third synthesis and delamination. (b) The roughness of the copper surface progressively becomes smoother with more synthesis and delamination steps. (c) The resultant graphene quality was consistent between the numerous synthesis steps with negligible Raman defect signature and good monolayer coverage.

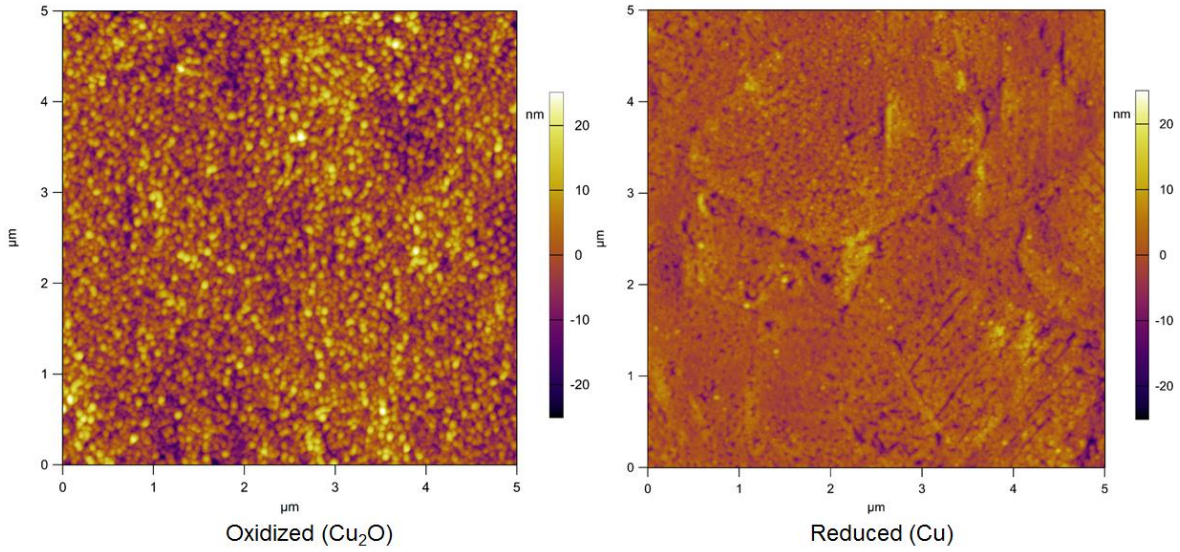

Figure 2.10. AFM morphology of oxidized (Cu_2O, left) and reduced (metallic copper, right) copper substrate surfaces, before and after electrochemical reduction in carbonic acid, respectively. Averaged across five random areas of 25μm^2 each, the Cu_2O measured a RMS roughness of 6.12±0.03nm whereas the reduced metallic copper surface measured 2.88±0.06nm.

2.6. Conclusion

We report the successful development of a method for under-etching delamination transfer of inch-scale monolayer graphene from its native copper substrate that is residue free and environmentally

benign. Specifically, the use of carbonic acid as the conducting electrolyte mitigates the contamination issues associated with conventional methods of chemically etching the copper foil substrate and also other previously reported delamination schemes using conventional etchants and electrolytes. In contrast, our transfer process allows for a clean interface between graphene and target substrate without the need for repeated rinsing since the carbonic acid electrolyte simply evaporates away as water and carbon dioxide upon drying, realizing significant savings in process water usage and also allows for the recycle of the copper substrate for subsequent graphene synthesis. We have also demonstrated the use of EC solvated in ethanol as a more sustainable and environmentally benign alternative to conventional graphene transfer polymers. As a ubiquitous food-grade polymer solvable simply in ethanol, its utility in 2D materials processing affords many cost, health, and environmental advantages compared with conventionally used polymers which require the use of harsh solvents.

As a ubiquitous and physiologically important compound, carbon dioxide has much potential for value added applications such as that demonstrated here as a residue-free electrolyte for electrochemical materials processing. We envision a breadth of novel developments in scientific and industrial uses for carbonic acid, especially with possible routes to further catalyze its dissociation to increase conductivity and acidity. In addition to creating a value-added application for otherwise nuisance captured carbon dioxide, the developments presented enables reuse of high purity copper foil substrate for CVD graphene synthesis. This new method also minimizes water usage and substitutes conventional polymers with biomass derived ethyl cellulose, which opens up new possibilities for cleaner, scalable, and less energy intensive sustainable manufacturing for a host of 2D materials.

2.7. Bibliography

(1) Novoselov, K. S.; Fal′ko, V. I.; Colombo, L.; Gellert, P. R.; Schwab, M. G.; Kim, K. *Nature* **2012**, *490*, 192–200.

(2) Kang, J.; Shin, D.; Bae, S.; Hong, B. H. *Nanoscale* **2012**, *4*, 5527.

(3) Chen, Y.; Gong, X.-L.; Gai, J.-G. *Advanced Science* **2016**, *3*, 1500343.

(4) Gao, L.; Guest, J. R.; Guisinger, N. P. *Nano Letters* **2010**, *10*, 3512–3516.

(5) Wang, Y.; Zheng, Y.; Xu, X.; Dubuisson, E.; Bao, Q.; Lu, J.; Loh, K. P. *ACS Nano* **2011**, *5*, 9927–9933.

(6) Gao, L.; Ren, W.; Xu, H.; Jin, L.; Wang, Z.; Ma, T.; Ma, L.-P.; Zhang, Z.; Fu, Q.; Peng, L.-M.; Bao, X.; Cheng, H.-M. *Nature Communications* **2012**, *3*, 699.

(7) Wang, X.; Tao, L.; Hao, Y.; Liu, Z.; Chou, H.; Kholmanov, I.; Chen, S.; Tan, C.; Jayant, N.; Yu, Q.; Akinwande, D.; Ruoff, R. S. *Small* **2014**, *10*, 694–698.

(8) Zhan, Z.; Sun, J.; Liu, L.; Wang, E.; Cao, Y.; Lindvall, N.; Skoblin, G.; Yurgens, A.; Novoselov, K. S.; Roth, S.; Geim, A. K.; Wu, H. A.; Geim, A. K.; Ahn, J.-H.; Hong, B. H.; Iijima, S. *Journal of Materials Chemistry C* **2015**, *3*, 8634–8641.

(9) Koefoed, L.; Kongsfelt, M.; Ulstrup, S.; Čabo, A. G.; Cassidy, A.; Whelan, P. R.; Bianchi, M.; Dendzik, M.; Pizzocchero, F.; Jørgensen, B.; Bøggild, P.; Hornekær, L.; Hofmann, P.; Pedersen, S. U.; Daasbjerg, K. *Journal of Physics D: Applied Physics* **2015**, *48*, 115306.

(10) Liu, L.; Liu, X.; Zhan, Z.; Guo, W.; Xu, C.; Deng, J.; Chakarov, D.; Hyldgaard, P.; Schröder, E.; Yurgens, A.; Sun, J. *Advanced Materials Interfaces* **2016**, *3*, 1500492.

(11) de la Rosa, C. J. L.; Lindvall, N.; Cole, M. T.; Nam, Y.; Löffler, M.; Olsson, E.; Yurgens, A. *Applied Physics Letters* **2013**, *102*, 022101.

(12) Ciuk, T.; Pasternak, I.; Krajewska, A.; Sobieski, J.; Caban, P.; Szmidt, J.; Strupinski, W. *The Journal of Physical Chemistry C* **2013**, *117*, 20833–20837.

(13) Wang, X.; Kholmanov, I.; Chou, H.; Ruoff, R. S. *ACS Nano* **2015**, *9*, 8737–8743.

(14) Gao, L.; Ni, G.-X.; Liu, Y.; Liu, B.; Castro Neto, A. H.; Loh, K. P. *Nature* **2013**, *505*, 190–194.

(15) Cherian, C. T.; Giustiniano, F.; Martin-Fernandez, I.; Andersen, H.; Balakrishnan, J.; Özyilmaz, B. *Small* **2015**, *11*, 189–194.

(16) Wang, M. C.; Chun, S.; Han, R. S.; Ashraf, A.; Kang, P.; Nam, S. *Nano Letters* **2015**, *15*, 1829–1835.

(17) Gibbons, B. H.; Edsall, J. T. *The Journal of Biological Chemistry* **1963**, *238*, 3502–3507.

(18) Berg, D.; Patterson, A. *Journal of the American Chemical Society* **1953**, *75*, 5197–5200.

(19) Garg, L. C.; Maren, T. H. *Biochimica et Biophysica Acta (BBA) - General Subjects* **1972**, *261*, 70–76.

(20) Wood, J. D.; Doidge, G. P.; Carrion, E. A.; Koepke, J. C.; Kaitz, J. A.; Datye, I.; Behnam, A.; Hewaparakrama, J.; Aruin, B.; Chen, Y.; Dong, H.; Haasch, R. T.; Lyding, J. W.; Pop, E. *Nanotechnology* **2015**, *26*, 055302.

(21) Choi, J.; Kim, H. J.; Wang, M. C.; Leem, J.; King, W. P.; Nam, S. *Nano Letters* **2015**, *15*, 4525–4531.

(22) Kang, P.; Wang, M. C.; Knapp, P. M.; Nam, S. *Advanced Materials* **2016**, *28*, 4639–4645.

(23) Leem, J.; Wang, M. C.; Kang, P.; Nam, S. *Nano Letters* **2015**, *15*, 7684–7690.

(24) Ashraf, A.; Wu, Y.; Wang, M. C.; Yong, K.; Sun, T.; Jing, Y.; Haasch, R. T.; Aluru, N. R.; Nam, S. *Nano Letters* **2016**, *16*, 4708–4712.

(25) Wang, M. C.; Leem, J.; Kang, P.; Choi, J.; Knapp, P.; Yong, K.; Nam, S. *2D Materials* **2017**, *4*, 022002.

(26) Bard, A. J.; Faulkner, L. R. *Electrochemical methods : fundamentals and applications*; Wiley, 2001.

(27) Ferrari, A. C.; Basko, D. M. *Nature Nanotechnology* **2013**, *8*, 235–246.

(28) Lupina, G.; Kitzmann, J.; Costina, I.; Lukosius, M.; Wenger, C.; Wolff, A.; Vaziri, S.; Östling, M.; Pasternak, I.; Krajewska, A.; Strupinski, W.; Kataria, S.; Gahoi, A.; Lemme, M. C.; Ruhl, G.; Zoth, G.; Luxenhofer, O.; Mehr, W. *ACS Nano* **2015**, *9*, 4776–4785.

Chapter 3. Heterogeneous, three-dimensional texturing of graphene

The work presented in this chapter was published in *Nano Letters*, 15 (3), 1829-1835 (2018) and disclosed in US Patent 9,908,285.

3.1. Introduction

Graphene, a single atomic layer of sp^2-bonded carbon atoms, has been a material of intensive research and interest over recent years.[1,2] The combination of its exceptional mechanical properties[3], high carrier mobility[4], thermal conductivity[5], and chemical inertness make it a candidate material for next generation optoelectronic, electromechanical and bio-electronic applications.[6–8] Particularly, graphene's large surface-to-volume ratio, low detection limit, and high sensitivity have enabled graphene-based field-effect transistor (FET) sensors[7] with single molecule detection limit.[6] As a prerequisite to these achievements, significant progress has already been made in realizing large-area graphene synthesis[9], transferability onto various substrates[10], and device integration with other low-dimensional and conventional materials. Recent efforts have also focused on controlling graphene's material properties by altering its morphology.[11,12] In particular, electrical properties can be modulated via elastic strain engineering whereby localized bending of graphene alters the electronic band structures and can induce pseudo-magnetism.[13–17]

In addition to the aforementioned phenomena, mechanical straining of graphene can also be exploited to intentionally induce three-dimensionality (3D) to this otherwise 2D material[18], whereby textured graphene may serve as a candidate material platform for 3D electrodes and sensors.[19] Notably, physical deformation by texturing graphene amplifies its surface area[20,21], thereby increasing the degree of functionalization[22,23] and alters chemical reactivity[24], which is desirable for applications such as electrode materials in electrochemical cells and

supercapacitors.[18,25,26] In addition, crumpling of surface films in general has been well established as a means to confer or enhance the stretchability and flexibility to otherwise stiff films[27] and numerous novel applications have already been reported for various textured graphene and graphitic films such as tunable wettability and optical properties.[11]

A single-step strategy was developed to achieve heterogeneous, three-dimensional (3D) texturing of graphene and graphite by using a thermally-activated shape-memory polymer substrate. Uniform arrays of graphene crumples can be created on the centimeter scale by controlling simple thermal processing parameters without compromising the electrical properties of graphene. In addition, we showed the capability to selectively pattern crumples from otherwise flat graphene and graphene/graphite in a localized manner, which has not been previously attainable using other methods. Finally, we demonstrated 3D crumpled graphene field-effect transistor arrays in a solution-gated configuration. The presented approach has the capability to conform onto arbitrary 3D surfaces, a necessary prerequisite for adaptive electronics, and will enable facile large-scale topography engineering of not only graphene but also other thin-film and 2D materials in the future.

3.2. Three-dimensional (3D) texturing of two-dimensional (2D) graphene

We report a novel method for controlled crumpling of graphene and graphite via large heat-induced contractile deformation of the underlying substrate. While graphene intrinsically exhibits tiny ripples in ambient conditions[28], we seek to intentionally create large and tunable crumpled textures in a deterministic and scalable fashion. As a simpler, more scalable and spatially selective method unique from previous aforementioned techniques, this texturing of graphene and graphite exploits the thermally-induced transformation of shape-memory thermoplastics, which has been previously applied to microfluidic device fabrication, metallic film patterning, nanowire assembly and robotic self-assembly applications.[29–34] More notably, we explore a novel localized 3D texturing scheme,

enabling creation of a mixture of flat and crumpled heterogeneous morphologies based on graphene/graphite alone, which has been unattainable with previous methods to date. Furthermore, we carry out systematic investigations of electrical, morphological and materials characterizations as graphene/graphite crumples are progressively generated and demonstrate their application as a solution-gated, crumpled graphene FET device. This is a new direction compared to previous studies which have utilized either pre-patterned growth substrates, pre-strained flexible polymeric substrates (mechanically deformed elastomers such as polydimethylsiloxane (PDMS) and polyethylene terephthalate (PET)), swelled hydrogels, or thermal expansion mismatch to yield overall global crumpling of thin metallic films and also graphene upon relaxation of the pre-deformed or pre-swelled substrates.[11,35–37]

3.3. Experimental procedure

Graphene and graphite samples were synthesized using established chemical vapor deposition (CVD) techniques on copper foils and cobalt-copper (Co-Cu) catalyst thin films, respectively. Copper has negligible carbon solubility and thus yields only one to three layers of graphene on the catalyst surface whereas Co-Cu thin films with a higher carbon solubility can be used to synthesize graphite with tunable thicknesses.[19] To minimize contamination and ensure material compatibility with the target polymeric substrate, a direct solution-based transfer approach was used to apply the centimeter-scale graphene films onto the target polymer substrate without the use of a carrier film such as poly(methyl methacrylate) (PMMA) or metallic films which would otherwise require subsequent chemical treatment (see Methods).

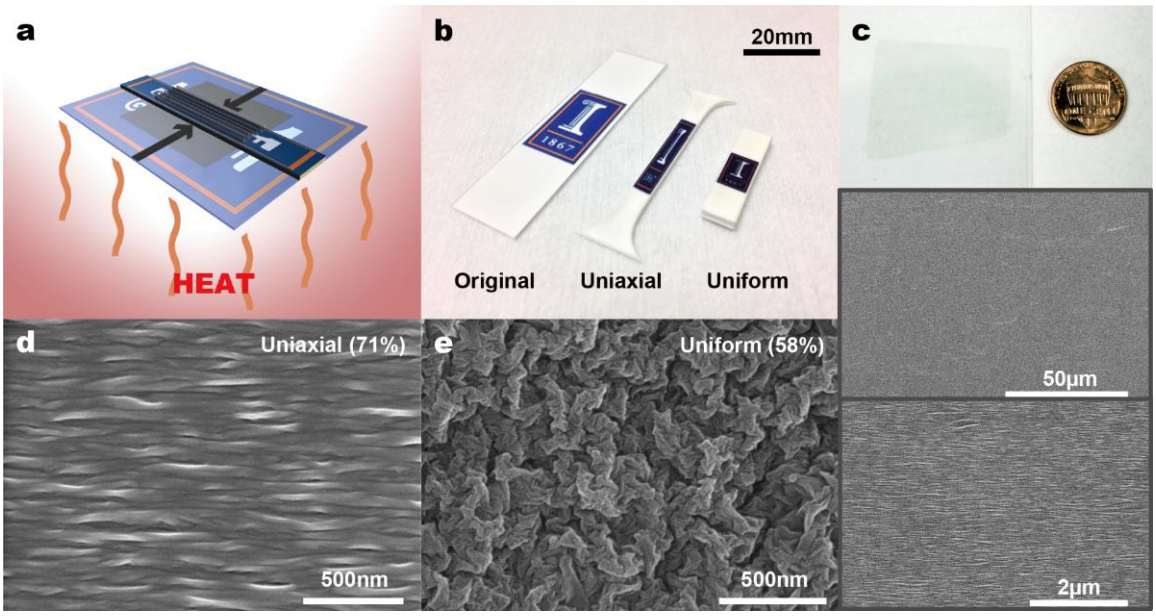

Figure 3.1. Fabrication and characterization of large-scale, thermally-induced graphene crumples on PS. (a) Schematic of thermally-induced PS substrate transformation to affect crumpling of graphene/graphite. (b) Photograph illustrating the original untreated sample (original, left) versus samples subjected to different texturing schemes of uniaxial strain (middle) and uniform/equi-biaxial strain (right). (c) Photograph and SEM show the centimetre scale transfer and texturing capability of our direct solution transfer technique onto PS with good uniformity. High-magnification SEM reveals the unique resultant graphene crumple morphologies due to uniaxial (71%) (d) and equi-biaxial/uniform (58%) (e) strains, respectively.

Graphene was synthesized by chemical vapor deposition (CVD) (Rocky Mountain Vacuum Tech Inc., CO) using 25 μm thick copper foil (Alfa Aesar, MA) in a methane (100 sccm) and hydrogen (50 sccm) atmosphere at 1050 °C, 520 mTorr for 2 minutes. The copper foil had been cleaned with acetone, isopropyl alcohol (IPA), and hydrochloric acid and then annealed at 1050 °C prior to synthesis for ~60 minutes in 150 mTorr hydrogen atmosphere.

To minimize contamination and ensure material compatibility with the polystyrene (PS) substrate (i.e. solvent free process), a novel direct aqueous solution transfer approach was devised to apply the centimeter-scale graphene films onto target substrates (PS or SiO_2) without the use of a carrier

film such as poly(methyl methacrylate) (PMMA), which is typical of conventional transfer techniques.

Following CVD synthesis, the as-grown graphene on copper foil was subsequently carefully floated onto the surface of prepared sodium persulphate ($Na_2S_2O_8$) etchant solution (Sigma Aldrich, MA) for several hours without the use of any carrier film/medium. Complete removal of copper is verified visually and immediately after complete copper dissolution has occurred, the resulting free-floating graphene film was then twice transferred to deionized (DI) water surface to remove residual etchant and finally transferred onto cleaned oriented PS sheets (K&B Innovations, WI) (Figure 3.1c). To minimize breakage of the delicate graphene film, extreme care was exercised to minimize any disturbance to the setup and liquid interface, with measures including securing the container to the lab bench and sealing the container to prevent air entrainment and turbulence. Furthermore, both the glass slides used to transfer the graphene for DI water rinsing and the PS target substrate were pre-wetted in DI water to minimize surface tension disturbances to the liquid interface when retrieving the graphene film. During the retrieval process, the target substrate was kept at a constant angle of ~45deg and held very steadily while being raised out of the liquid.

Graphite and graphene-graphite heterostructure pattern samples were prepared similarly via CVD synthesis on cobalt and copper thin film catalyst substrates, which were deposited via plasma sputtering (AJA International, MA) on a 285nm SiO_2 wafer. Following established CVD techniques, the as-grown surface graphite and graphene-graphite films were carefully transferred onto the same aforementioned sodium persulphate solution surface for etching of the catalyst metallic layer with the aid of a spun-on PMMA (Sigma Aldrich, MA) carrier top layer film. The graphite and graphene-graphite heterostructure patterns with PMMA film slowly cleaves away from the wafer as the metallic layers are etched and were subsequently twice transferred similarly

to DI water for cleaning and finally onto clean PS and SiO_2 substrates. The PMMA carrier top layer was finally removed with glacial acetic acid (compatible with PS) and subsequently rinsed in DI water.

The graphene texturing is realized via thermally-inducing contractile deformation of the underlying oriented polystyrene (PS) substrate by heating above its glass transition temperature (~120°C) as schematically shown in Figure 3.1a. The resultant compressive strain forms well-defined crumpled texturing of the graphene/graphite surface layer without any prior patterning such as with photo- or nano-imprint- lithography.[38,39]

Graphene and/or graphite on PS sheets were thermally activated in a standard lab oven (BINDER, Germany) at 120°C. The uniaxial samples were made by securing two ends of a PS sheet with a custom-made aluminum fixture while the equi-biaxial/uniform samples were simply laid on a clean glass slide during thermal treatment. Varying amounts of induced strain were achieved by adjusting the duration of heat treatment, which varied from 35 to 90 minutes. The resultant crumpled morphology were consistent throughout the entire surface sample, irrespective of position on the surface or proximity to edges with the bare PS substrate.

The resulting percentage strains are calculated as:

$$\%\, strain = \frac{l_o - l_i}{l_o}$$

where l_o and l_i represent the linear sample dimensions before and after thermal activation, respectively (i.e. a reduction from 15 mm to 4 mm is equivalent to a strain of 73%) consistent with the linear percentage change definition in ASTM D1204-02.

In general, three texturing schemes were realized (Figure 3.1b): (1) uniaxial, (2) equi-biaxial or uniform, and (3) localized. In the uniaxial texturing case, boundary conditions are applied whereby two ends of the PS substrate are held stationary to restrict contraction in the longitudinal direction (i.e. only the lateral width decreases). In the case of uniform contraction, the constraint was removed, and the PS substrate was allowed to freely move on a clean and rigid flat surface such as a glass slide.

3.4. Materials characterization

To systematically investigate the evolution of graphene crumples (i.e., roughness and coherence of the crumples) as a function of macroscopic compressive strain (i.e. amount of PS contraction), we obtained scanning electron microscope (SEM) (Figure 3.1c-e and Figure 3.4a insets) and atomic force microscope (AFM) images (Figure 3.2) and conducted 2D fast Fourier transform (FFT) analysis.

Optical microscope images were captured in darkfield transmission and reflection modes (Axio Imager M2m, Carl Zeiss, Germany). Scanning electron microscopy (SEM) images (S-4800, Hitachi, Japan) were obtained for graphene samples after being coated with 2.5 nm of AuPd to improve imaging contrast; graphite and graphene-graphite heterostructure samples were not coated.

SEM images (Figure 3.4a inset) show the development of linear crumples with concomitant observable increase in wrinkle alignment and coherence for the uniaxial case as the strain increases. Occasionally, sparse cracks develop during heat treatment (Figure 3.3), which allows visual distinction of crumple formation on an otherwise flat PS substrate, indicating that the crumples are intrinsic to the graphene and not due to corrugation of the substrate. Atomic force microscopy (AFM) surface data were recorded in tapping mode (MFP-3D, Asylum Research, CA) using a tip

with a tip radius of ≤10 nm and high aspect ratio (7:1), and subsequently second order flattened; RMS roughness and 2D fast Fourier transform were calculated using IGOR Pro (WaveMetrics, OR) and Gwyddion 2.38, respectively.

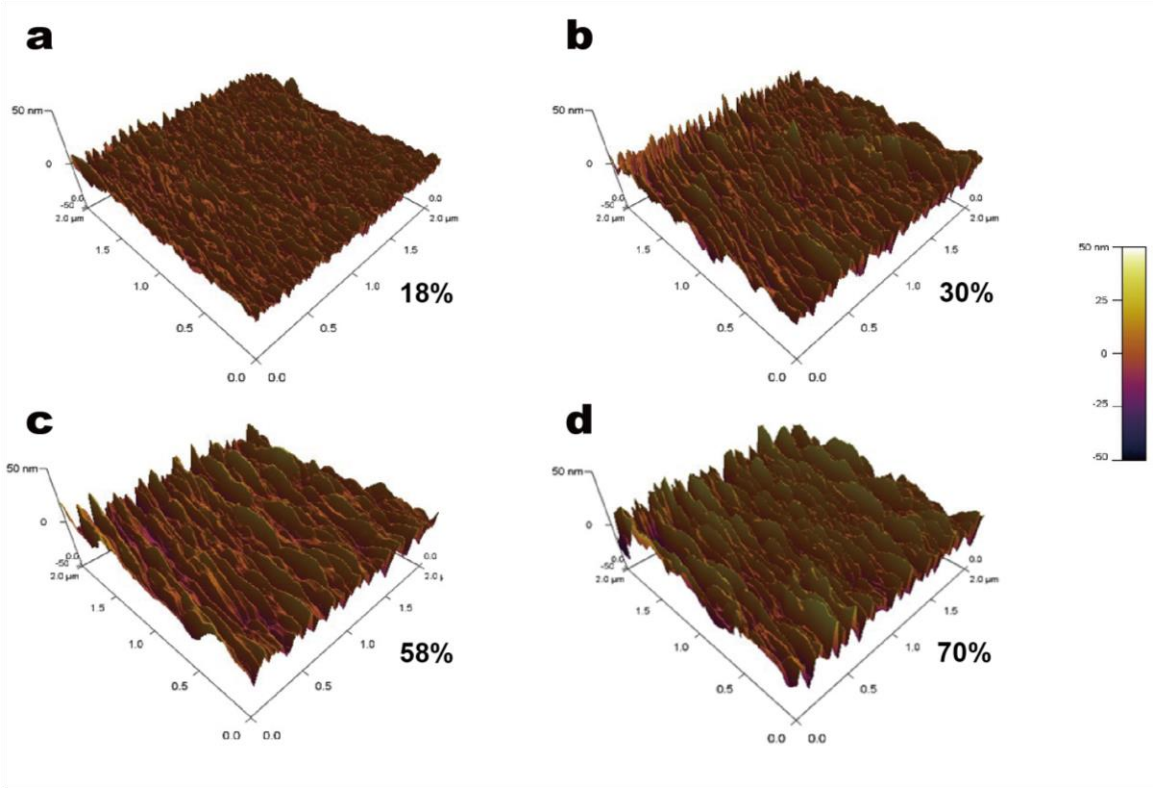

Figure 3.2. AFM topography render of uniaxially textured graphene crumples. Increased crumple coherence, roughness and alignment is observed as strain increases from (a) 18% to (b) 30%, (c) 58%, (d) 70%. Vertical full-scale: 100 nm.

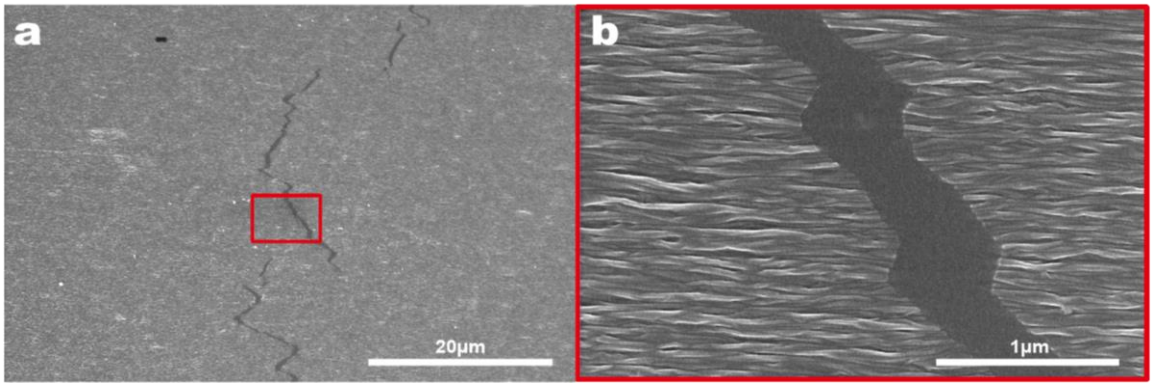

Figure 3.3. Interface between graphene crumples and flat PS substrate. SEM image of interface between crumpled graphene (58%) and flat PS substrate at a particular location where one of the sparse cracks developed during heat treatment, revealing the underlying flat PS substrate. Graphene remains mostly continuous even under high strains with few sparse cracks that develop during heat treatment which are entirely contained within the film (i.e. crack begins and ends within the interior of the graphene film and does not originate from the edge).

For the equi-biaxial case, on the other hand, patterns resembling disorganized herringbone structures are developed (Figure 3.1e).[40] AFM derived topography data for uniaxially crumpled graphene (Figure 3.4a and Figure 3.2) shows monotonic increase in the measured root mean square (RMS) surface roughness and crumple pitch (obtained by 2D FFT analysis) as the strain increases. The average measured RMS roughness of graphene crumples reaches up to ~8 nm with a macroscopic compressive strain of ~70%, where the percentage strain is defined as the linear percentage change of the PS. We note that the measured RMS roughness values may be underestimated and are limited to the inherent resolution of the AFM tips (see Methods) due to their ultrafine nature of the crumples.

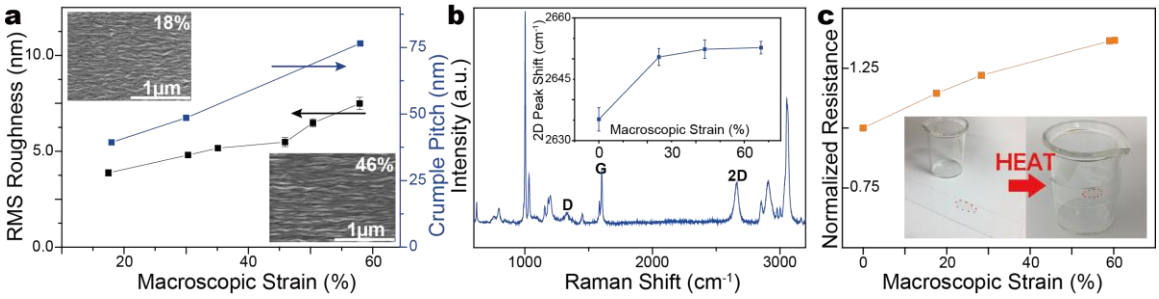

Figure 3.4. Characterization of graphene crumples. (a) Both the RMS roughness and crumple pitch increase monotonically with larger uniaxial compressive strains. Inset SEM images show uniaxial crumples (18% and 46%). The error bars represent one standard deviation. (b) Raman spectrum of uniaxially strained (71%) graphene crumples. Inset shows the 2D peak position shift as a function of increasing uniaxial strain. Raman spectrum of uniformly textured graphene is presented in Figure 3.5. The error bars represent one standard deviation. (c) Two terminal resistance shows no significant increase as uniaxial strain increases, indicating that graphene integrity is preserved. Inset shows the capability of this material configuration to integrate onto arbitrary curvilinear and 3D surfaces such as a beaker.

Raman spectroscopy characterization confirms the presence of quality graphene as compressive strain increases (Figure 3.4b and Figure 3.5). The Raman D-to-G peak intensity ratio does not change significantly as the strain increases, which demonstrates that the material integrity of crumpled graphene is preserved, and that deformation of graphene is highly elastic in both uniaxial and equi-biaxial cases. To infer the intrinsic strain developed, we observed a consistent blue shift of the 2D band as the macroscopic compressive strain increases (Figure 3.4b inset), consistent with observations from earlier literature.[41] Raman spectra were obtained with a 633 nm laser source (InVia microPL, Renishaw, UK) at 1800/mm grating and 1 second accumulation.

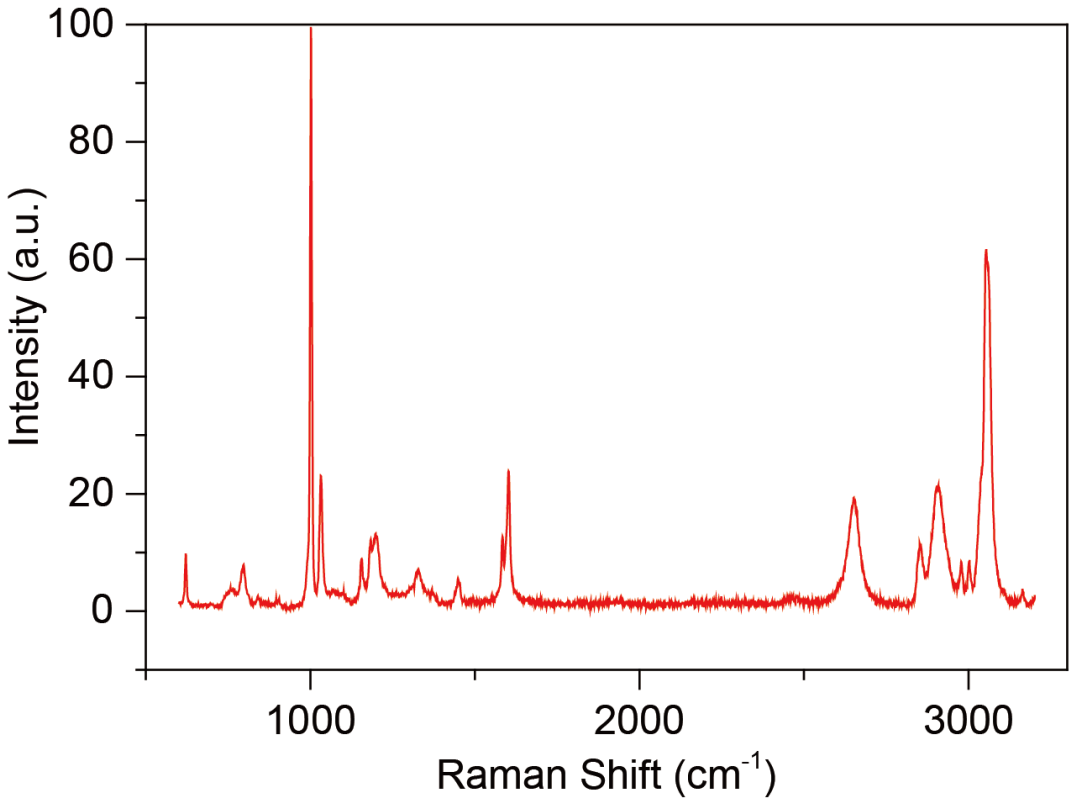

Figure 3.5. Raman spectrum of equi-biaxially/uniformly textured graphene crumples. Raman spectroscopy confirms presence of graphene for equi-biaxially (58%) textured graphene crumples. Sample spectra are flattened against the PS baseline spectra and normalized to the most prominent peak.

Due to the vicinity of the graphene Raman G peak to the background peaks of PS and the susceptibility of G peak position to doping effects, the shift in 2D peak position is considered as an indicator of the intrinsic amount of strain developed inside the crumples. Up to a macroscopic uniaxial strain of 67%, the 2D peak position (as fitted by a single Lorentzian function) blue shifts from ~2636cm^{-1} to ~2653cm^{-1} (Figure 3.4b inset). Considering previous estimates of a -64cm^{-1}/% blue-shift arising from intrinsic uniaxial compressive strain, the ~17cm^{-1} blue-shift measured would correspond to an intrinsic compressive strain of ~0.27% which is on the same order of magnitude with previously reported values for compressively wrinkled patterned graphene ribbons.[35,42,43] The PS background Raman spectrum is shown in Figure 3.6.

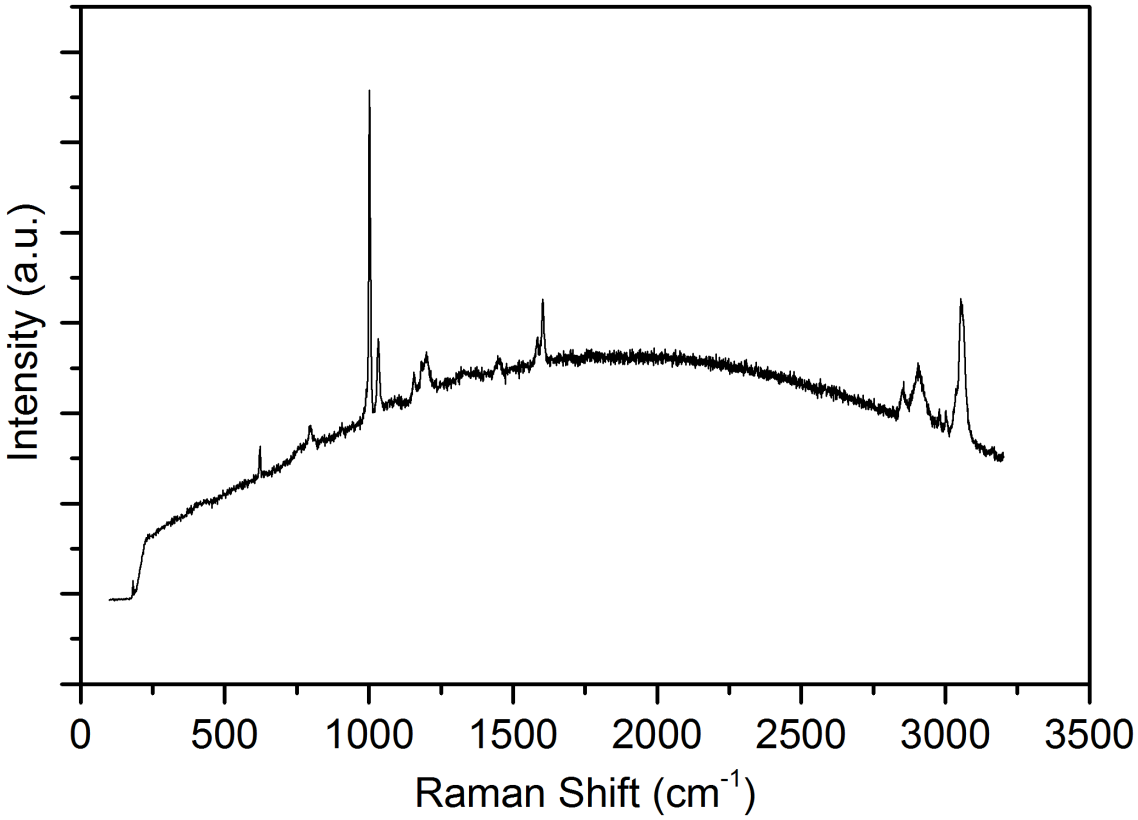

Figure 3.6. Raman spectrum of as-is PS substrate.

3.5. Robustness, material integrity, and reversibility of crumpled graphene

To substantiate that crumpled texturing will not adversely affect graphene's electrical properties, two-terminal electrical resistance (Figure 3.4c) measurement was performed by successively increasing the uniaxial strain and measuring transverse to the crumples. No significant increase in the resistance was observed even up to the maximum attainable 73% compressive strain, with the modest increase (~36%) in resistance attributable to physical damage from repeated probe contact and also successive environmental exposure during each heat treatment step necessary to increase the strain.

From both Raman and two-terminal electrical measurements, we deduce that graphene's integrity has been preserved while increasing compressive strains and that there has been little plastic deformation or damage of the graphene. Sheet resistance was also recorded as a function of increasing strain for both uniaxial and biaxial texturing (Figure 3.7 and Figure 3.8) and were consistent with values from earlier studies of graphene transferred onto a variety of similar polymeric substrates.[44] Sheet resistance measurements were conducted using a linear four-point probe head (RM3-AR, Jandel Engineering, UK) on the lowest probe pressure dial setting in order to minimize contact and puncture damage to the sample.

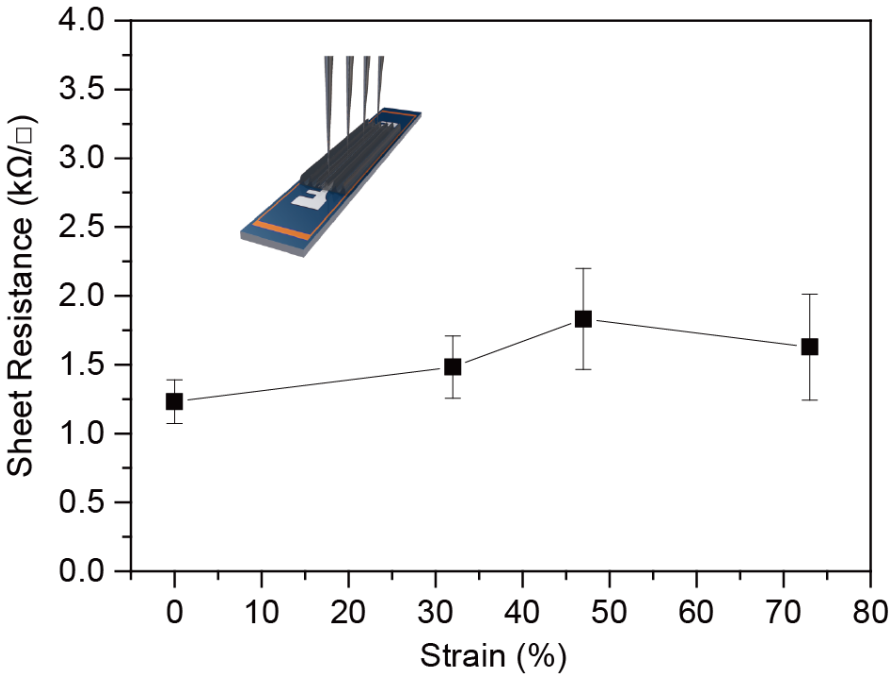

Figure 3.7. Sheet resistance of uniaxial graphene crumples. Four-point probe measurement on uniaxially textured graphene crumples as compressive strain increases shows no significant corresponding change in the sheet resistance, indicating that material integrity is preserved. Inset shows the four linear probes' measurement orientation with respect to the crumple direction. The error bars represent one standard deviation.

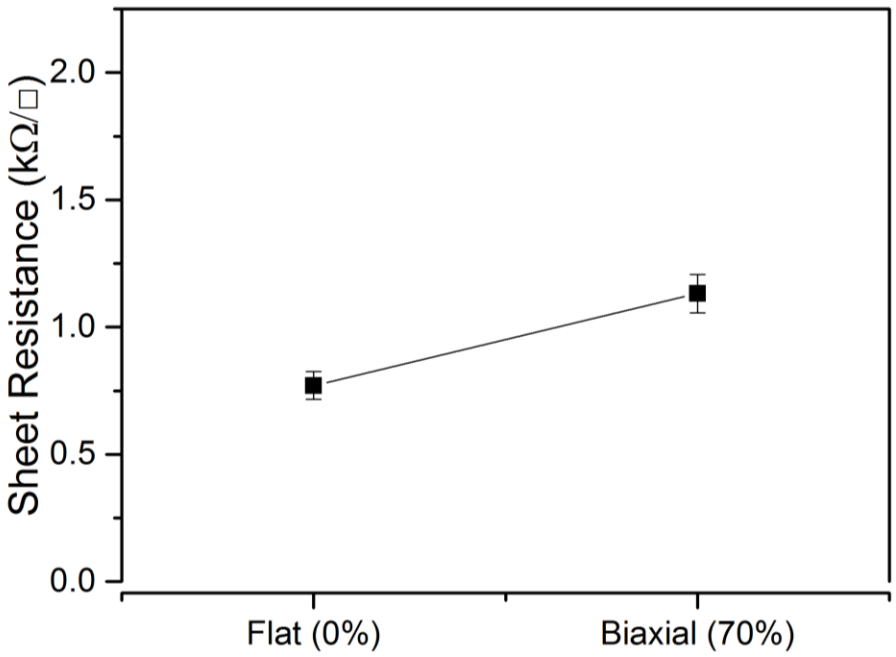

Figure 3.8. Sheet resistance of biaxial graphene crumples. Sheet resistance of graphene on PS before and after 70% biaxial crumpling. The error bars represent one standard deviation.

The use of a thermoplastic such as PS allows for facile integration with other materials in unconventional ways such as conformity and interfacing with arbitrary geometries. This is demonstrated by the fact that the PS substrate with crumpled graphene can be molded onto curved and 3D objects such as a small glass beaker (Figure 3.4c inset). Additionally, graphene crumples formed with this approach are amenable to subsequent transfer onto arbitrary substrates as PS is easily removable in contrast to elastomers such as PDMS. This allows for the integration of the crumpled structures onto various substrates via simple solvent treatment of PS followed by a solution based transfer. We have shown preliminary progress towards the transfer of the crumpled graphene from PS onto silicon oxide substrates whilst preserving the crumpled morphology (Figure 3.9).

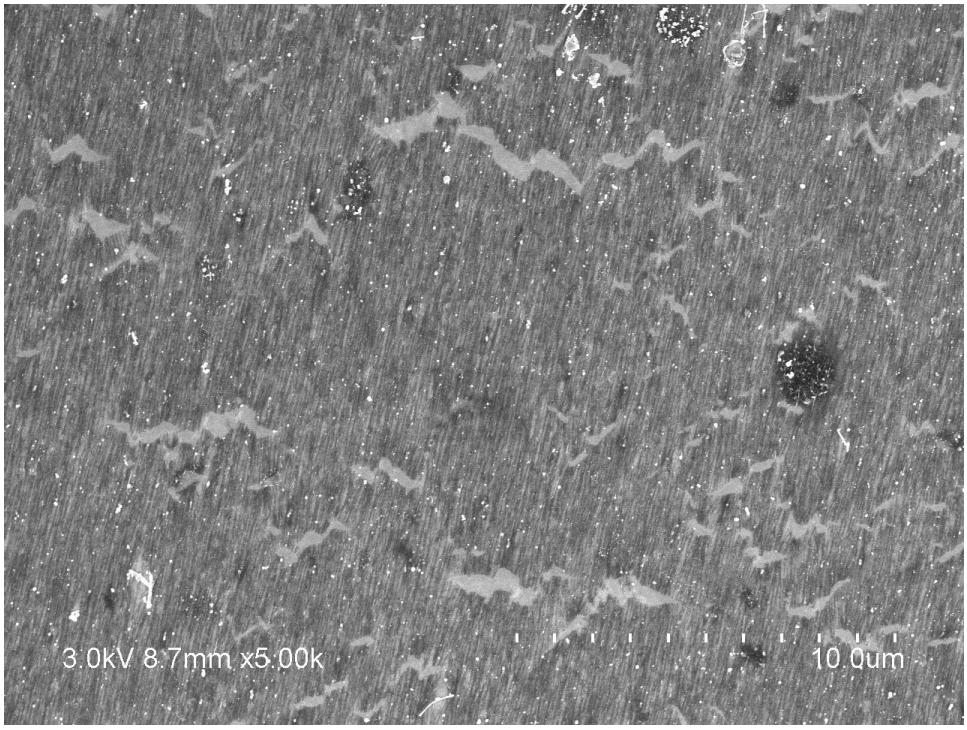

Figure 3.9. Crumpled graphene transferred onto a flat SiO_2 substrate. Uniaxially crumpled graphene transferred onto a 285 nm SiO_2 substrate via solvent removal of the PS substrate. Cracks arise from the imperfect transfer with some residual polymeric contamination.

The thermoplastic nature of the PS substrate also allows for the crumpled graphene morphology to be arbitrarily re-flattened by reshaping the polymer at the same elevated temperature for the crumpling process. SEM shows the various graphene morphology subjected to six cycles of uniaxial crumpling and re-flattening, which demonstrates that the graphene can be almost completely re-flattened (Figure 3.10). Corresponding Raman spectra (Figure 3.11) further substantiate that the quality of graphene does not deteriorate during the successive crumpling and re-flattening process.

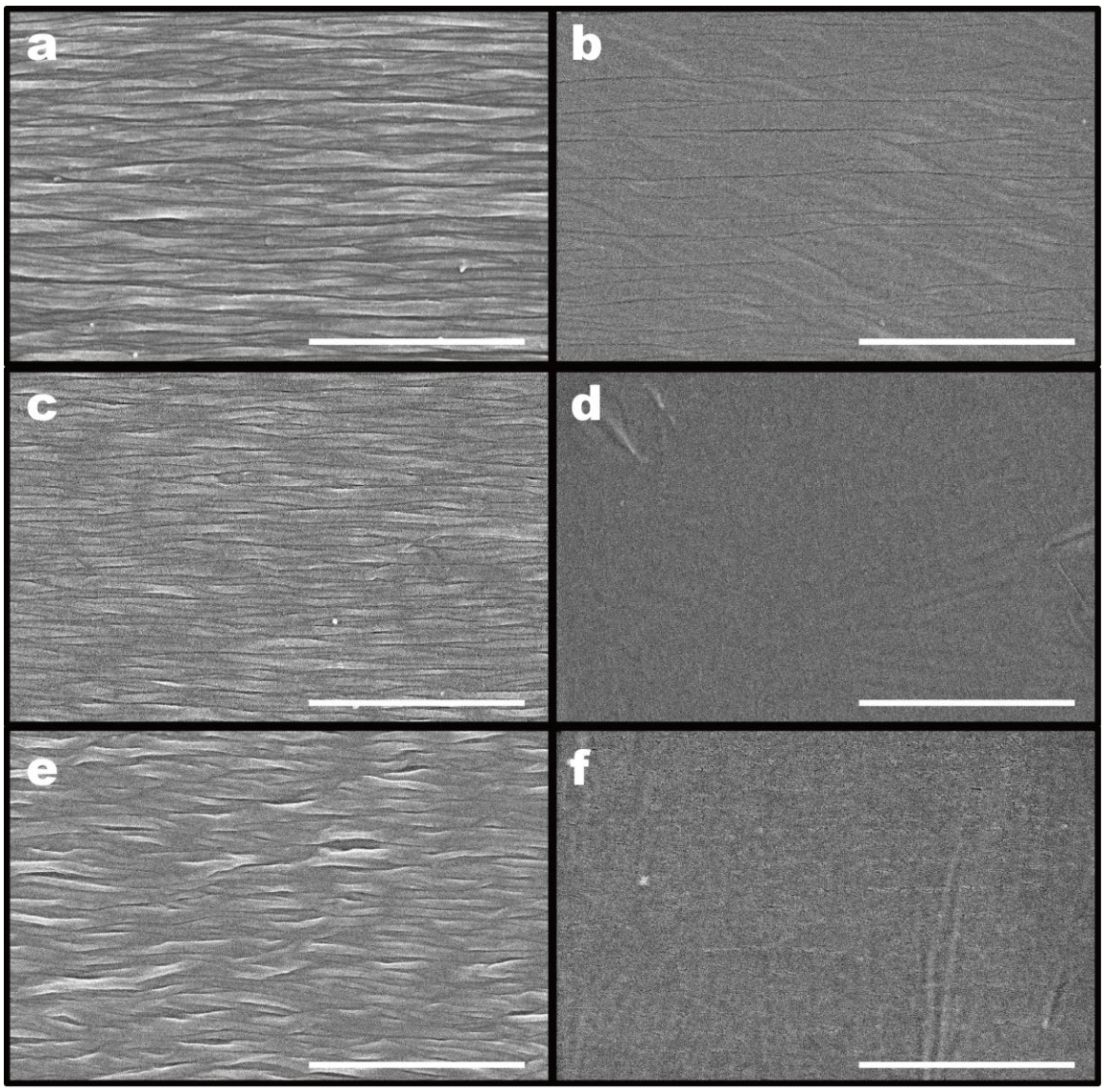

Figure 3.10. SEM of graphene on PS after (a) initial crumpling (~40%), (b) first re-flattening, (c) second crumpling (~35%), (d) second re-flattening, (e) sixth crumpling (~45%), and sixth re-flattening. All scale bars 1µm.

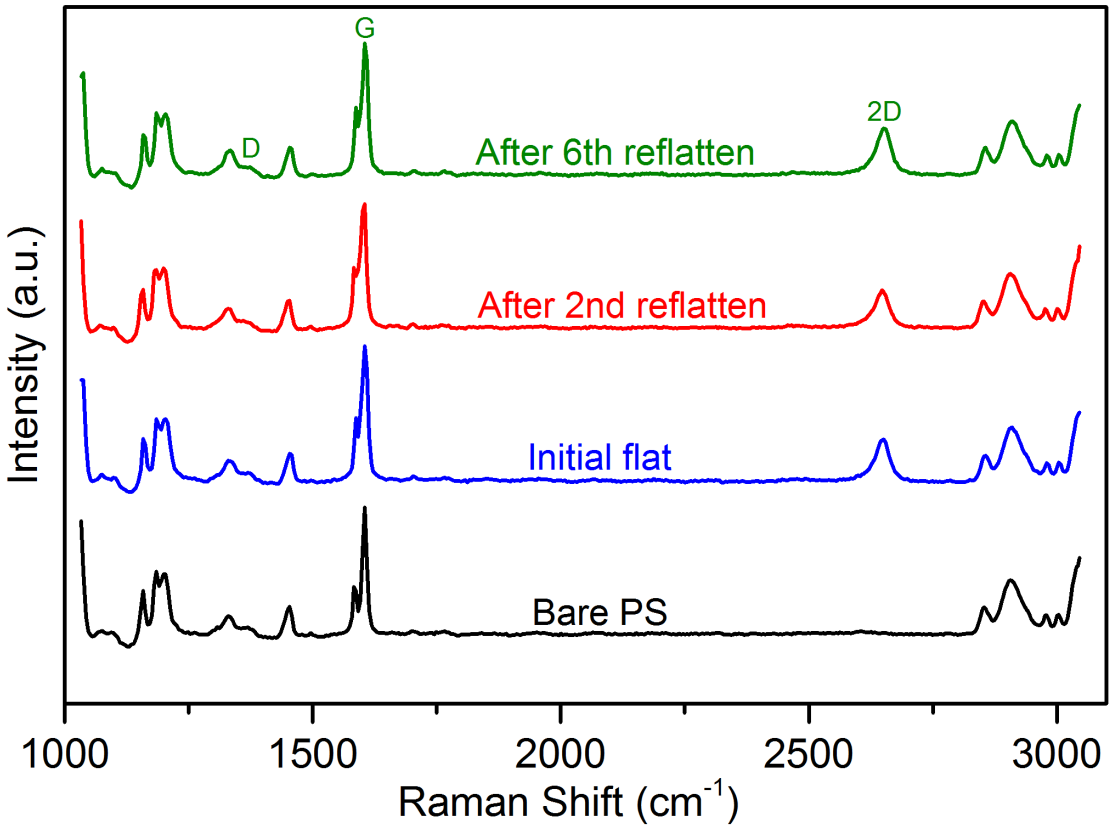

Figure 3.11. Raman spectra of the bare PS substrate (black), initially flat graphene (blue), graphene after two cycles of crumpling and re-flattening (red), and graphene after six cycles of crumpling and re-flattening (green).

The thickness effect on crumpling of multilayer graphene (or graphite) was explored and material characterizations were performed for similarly crumpled graphite films (average thickness of ~5 nm) synthesized using Co-Cu catalyst thin-films. SEM images (Figure 3.12a) and AFM height renders (Figure 3.13 and Figure 3.14) clearly show development of increasing height of crumples as a function of macroscopic compressive strains.

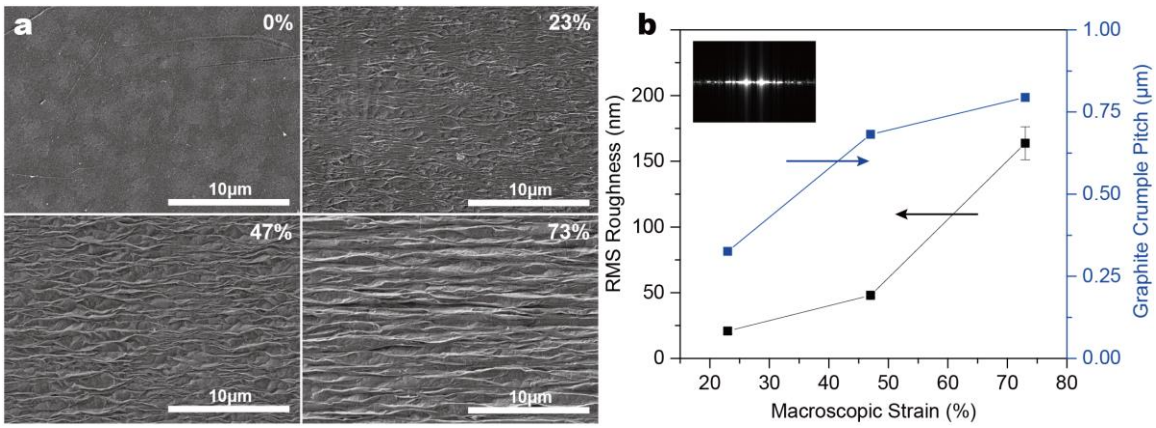

Figure 3.12. Characterization of graphite crumples. (a) SEM image of flat/untextured (0%) and uniaxially (23%, 47% and 73%) crumpled graphite. (b) Both the RMS roughness and crumple pitch increase monotonically with larger uniaxial compressive strains. The error bars represent one standard deviation. Inset shows 2D FFT obtained from AFM data of 73% uniaxially crumpled graphite.

Notably, bifurcation leading to hierarchical wrinkling is evident in the AFM renders (Figure 3.13) whereby a secondary crumple periodicity (of larger wavelength and amplitude) develops along with the original, finer crumple pattern and as a result, the 2D FFT (Figure 3.12b inset) shows an increasing crumple pitch as a function of strain (Figure 3.12b). As with graphene, the graphite crumples also show a monotonic increase in RMS roughness with larger compressive strains (Figure 3.12b).

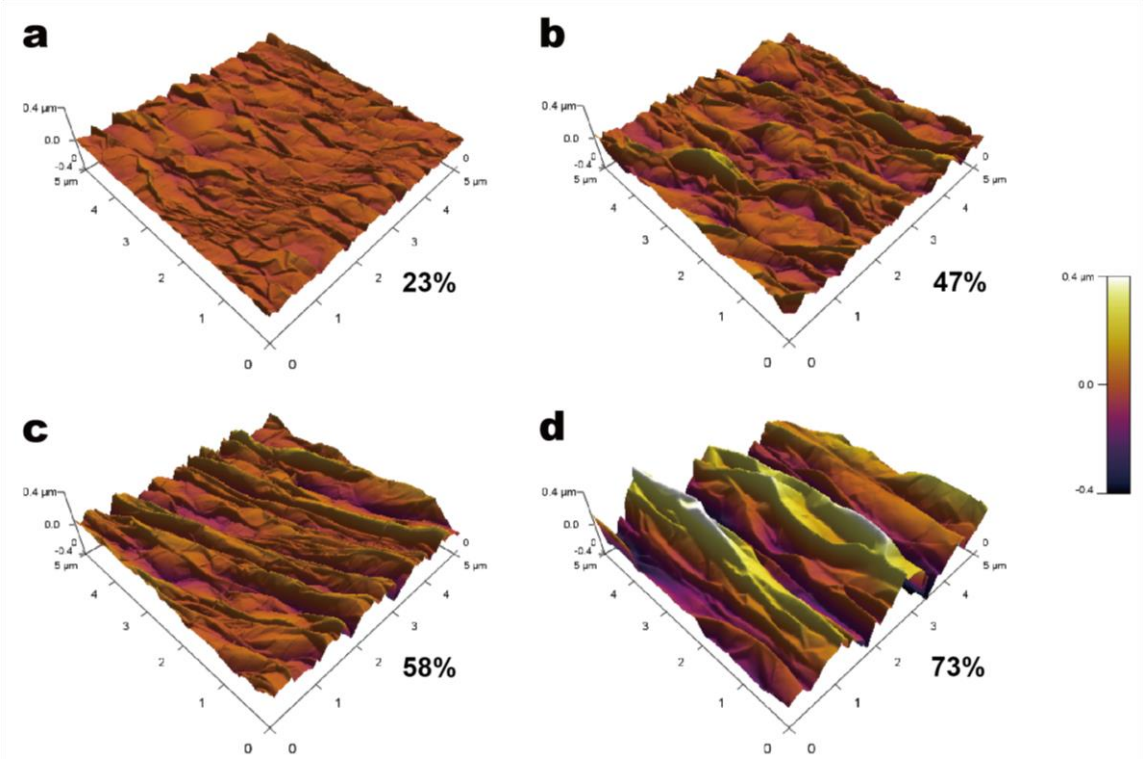

Figure 3.13. AFM topography render of uniaxially textured graphite crumples. Increased crumple height/roughness and alignment is observed as strain increases from (a) 23% to (b) 47%, (c) 58%, and (d) 73%. At the largest strain, bifurcation or hierarchical wrinkling is clearly evident. Vertical full-scale: 800 nm.

The area percent quantity represents a normalized increase in effective topographical surface area relative to the nominal AFM scan size. For example, an area percent increase of ~50% (Figure 3.14) is equivalent to a topographical area of 37.5 μm^2 on a 25 μm^2 scan domain (i.e. 5x5µm scan).

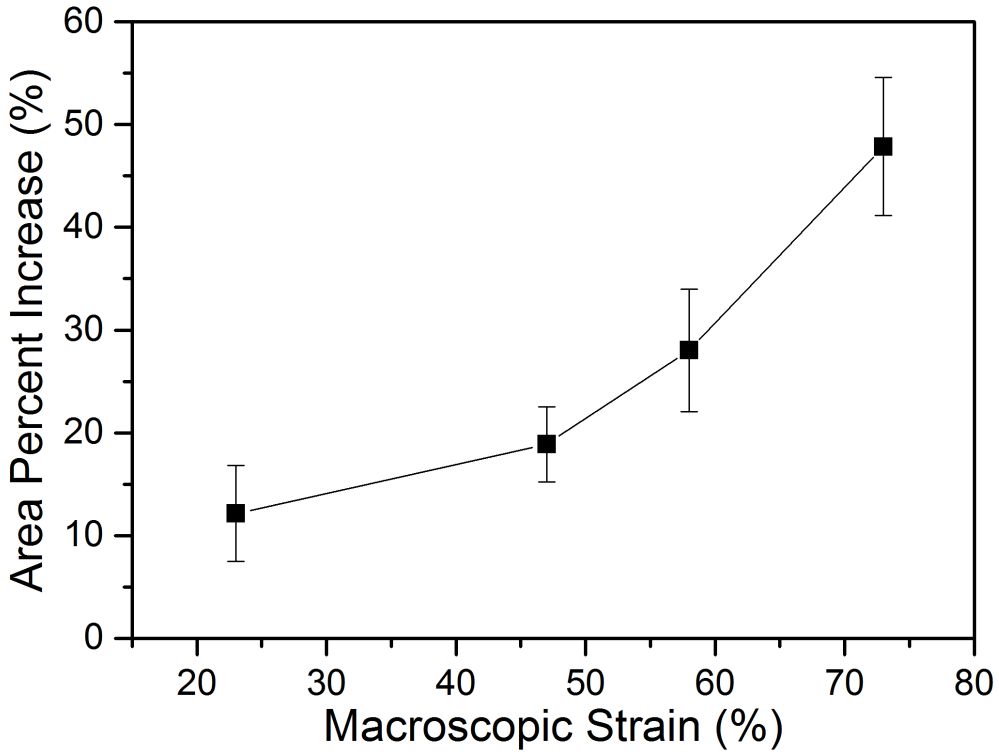

Figure 3.14. Area percent increase of uniaxially textured graphite crumples. As the strain increases, the size of the graphite crumples increases and results in larger effect surface area as measured by AFM. The error bars represent one standard deviation.

3.6. Monolithic and heterogeneous texturing of graphene

The unique aspect of thickness controlled crumpling behavior is further substantiated by investigating monolithic crumpling of connected, heterogeneous graphene-graphite patterns.[19] We synthesized a symmetrical cross pattern of thick graphite monolithically connected to a graphene background (Figure 3.15a,b). Upon uniaxial contraction of the pattern, the originally symmetrical cross-shaped graphite feature (dotted white line in Figure 3.15b) is deformed uniaxially into an asymmetric pattern reflecting the degree of contraction (~70%, black solid line in Figure 3.15b). We clearly observed differences in crumple morphology between that of graphene (surrounding the cross pattern) (Figure 3.15c) and that of graphite (inside the cross pattern) (Figure 3.15d), and furthermore, the monolithic interface is preserved between crumpled graphene and graphite.

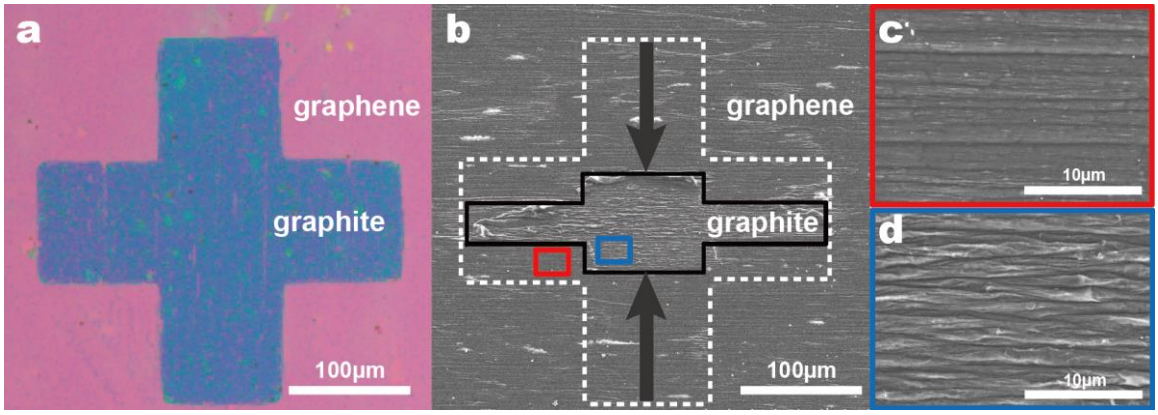

Figure 3.15. Heterogeneous uniaxial crumples via thickness variation between graphene/graphite. (a) Optical microscope image of original graphite cross pattern monolithically connected with a graphene background on a 285 nm SiO_2 substrate. Graphite features (blue) are ~20 nm thick relative to the graphene background (magenta). (b) SEM image of heterogeneous graphene-graphite cross pattern subjected to 70% uniaxial strain (dotted white outline indicates original cross pattern dimensions prior to texturing, and solid black outline shows outline after texturing). The background graphene (c) exhibits noticeably smaller crumples than the thicker graphite (d) region inside the cross pattern.

We investigate a unique capability of our heat induced crumpling approach where localized patterning of crumples is attainable via spatially selective heating of the substrate. Here, selectively controlled local texturing of graphene/graphite on PS is achieved by the application of a concentrated infrared (IR) source (Figure 3.16) on specific locations (Figure 3.17a). As opposed to previously reported approaches which require additional processing which relied on lithographic pre-patterning of the substrate or multi-step fabrication of a metal-film layer after graphene transfer[45], this direct localized patterning approach can be carried out immediately after the film of interest (i.e., graphene/graphite) has been transferred to the substrate.

Localized patterned samples were made by concentrating a 20-watt infrared source with a spot size of ~5 mm onto the PS sheet backside of the graphene/graphite surface. The IR source (IR-Si253-P-1, Hawkeye Technologies, CT) consists of a silicon nitride active element and a 1 inch

parabolic reflector. The IR was directed onto the sample in ambient conditions with no other optics used. Infrared thermal images of the IR setup were taken with a thermal camera (T400, FLIR, OR).

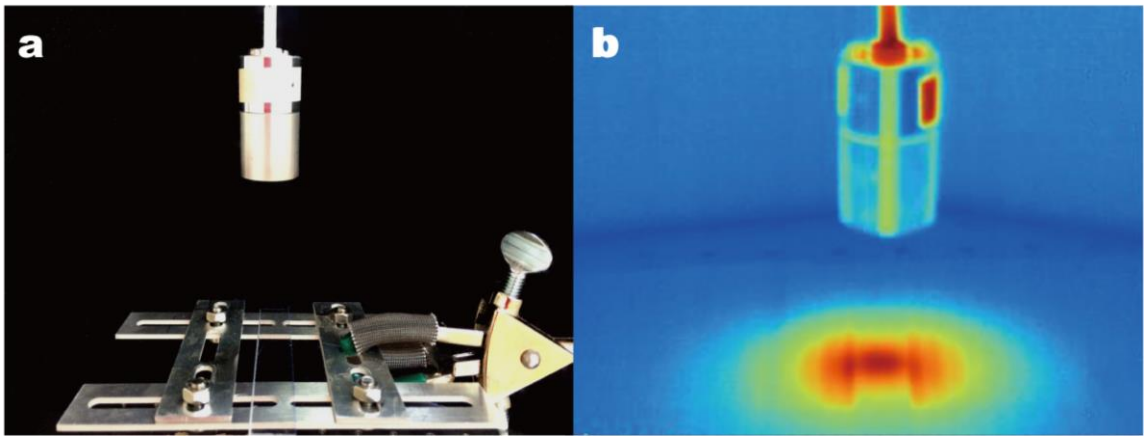

Figure 3.16. Infrared (IR) setup for localized texturing of graphene/graphite crumples. Photograph (a) shows the experimental setup of IR emitter used for localized patterning of PS with an accompanying IR thermal image (b) captured during irradiation showing a concentrated spot size of ~5 mm on a PS sheet.

At the junction of the heat affected area, the presence (or absence) of crumples is clearly visible (Figure 3.17b and Figure 3.18). High magnification SEM images at both regions show the lack and presence of crumples in the unaffected (Figure 3.17c) and affected regions (Figure 3.17d), respectively. This approach clearly demonstrates a simple, single-step, localized, direct patterning of 3D graphene or graphite crumples without any additional pre- or post-fabrication. Wide-field SEM image (Figure 3.18b) was compiled using Adobe Illustrator (Adobe Systems, CA) from individual standard SEM images.

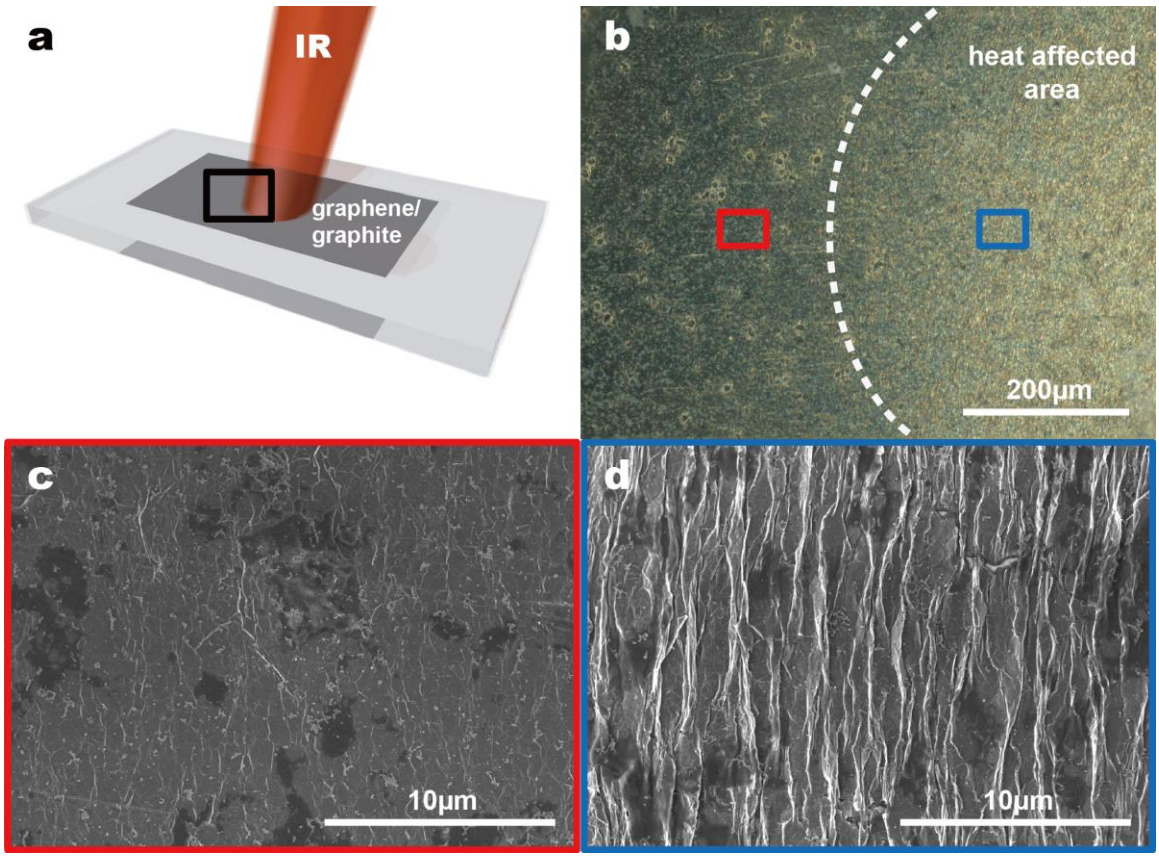

Figure 3.17. Localized patterning of graphene/graphite crumples. (a) Schematic shows localized patterned crumpling by subjecting selective areas of the sample to thermal irradiation. The heat affected area is visible in the dark field optical microscope image (b) due to contrast difference between crumpled versus flat graphene/graphite (interface shown as dotted line). SEM images show lack (c) and presence (d) of crumples on either side of the interface. Wide area SEM image (Figure 3.18) shows continuity of graphite film from flat to crumpled area.

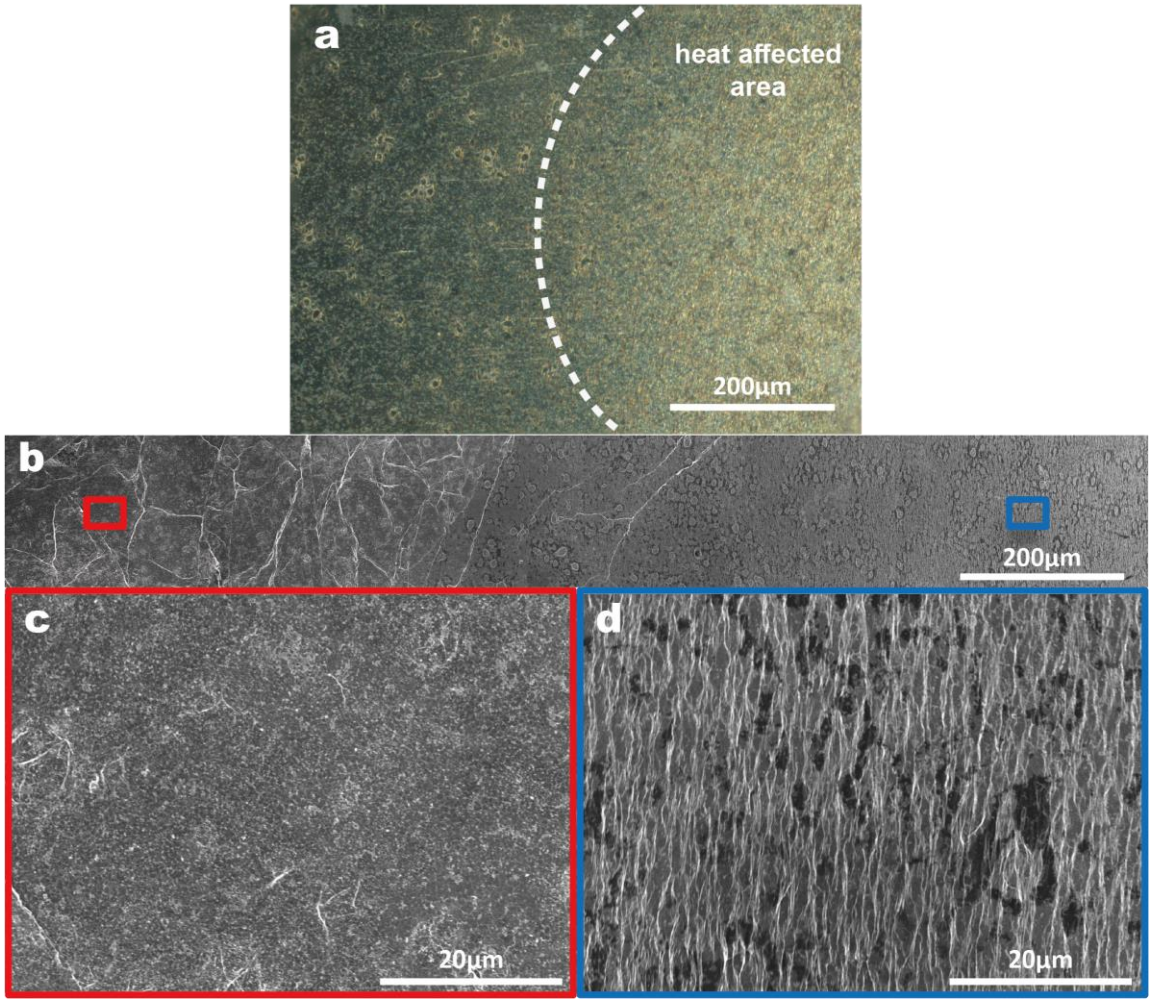

Figure 3.18. Continuity of locally textured graphite crumples. Optical microscope image of (a) locally textured graphite shows region affected by IR irradiation. Low magnification SEM image (b) corroborates continuity and gradient of crumples with the largest crumples being developed nearest to the IR focal spot (to the right). Higher magnification of the left region ((c), farther from IR spot) shows flat graphite with no crumpling whereas the right region ((d), closest to IR spot) shows large, dense crumples. Large scale (tens of microns) random wrinkles in the left portion of (b) are due to folds generated during solution transfer of graphite with PMMA onto a PS and subsequent removal of PMMA, and not associated with the IR irradiation.

To establish that the localized patterning via IR irradiation does not adversely contribute to additional graphene defect formation, the D peak intensity was characterized before and after 20

seconds of constant IR irradiation under ambient conditions for graphene on a flat 285nm SiO_2 substrate as a control (Figure 3.19) without interference from any PS Raman background.

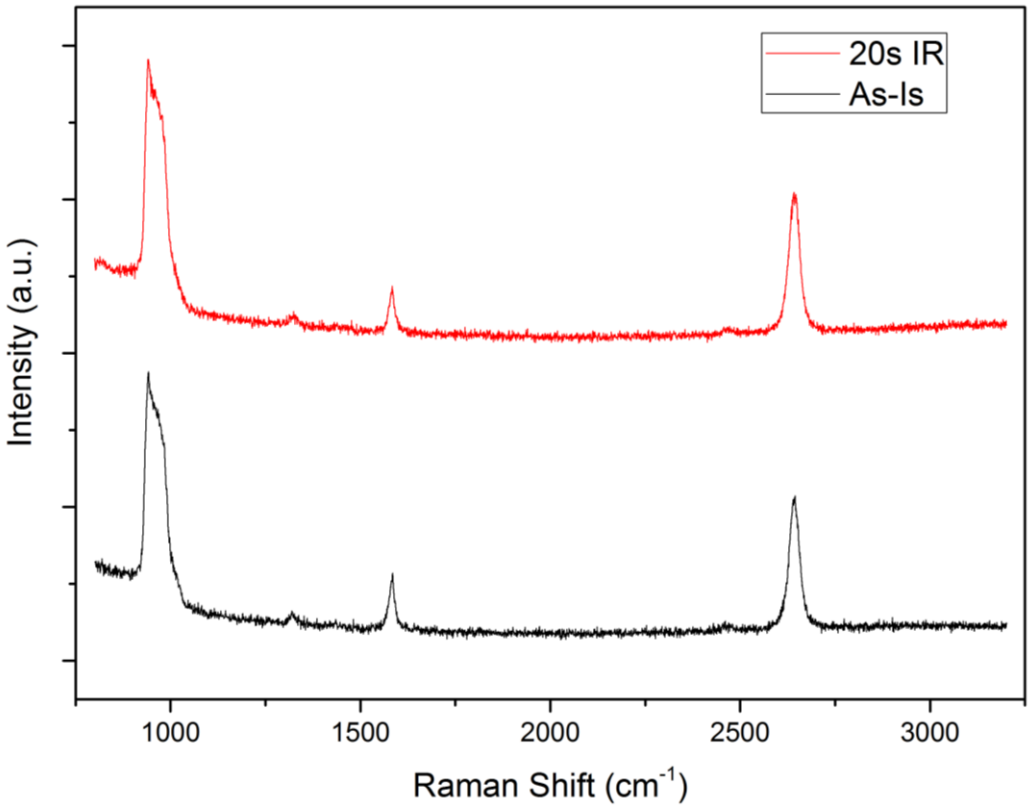

Figure 3.19. Raman spectrum of graphene on a 285nm SiO_2 substrate before (black) and after (red) 20 seconds of IR irradiation. Spectra are normalized to same 2D peak intensity.

The peak intensities in the spectra are almost identical, and there is no appreciable increase in the intensity or broadening of the D peak even after 20 seconds of constant IR irradiation on the control sample, which is significantly longer than the typical irradiation time used for localized texturing (~5s). Aside from comparing the Raman spectra, we conducted four-point probe sheet resistance measurements of graphene on SiO_2 before and after the same 20s IR irradiation to confirm that it does not significantly adversely affect its conductivity (Figure 3.20).

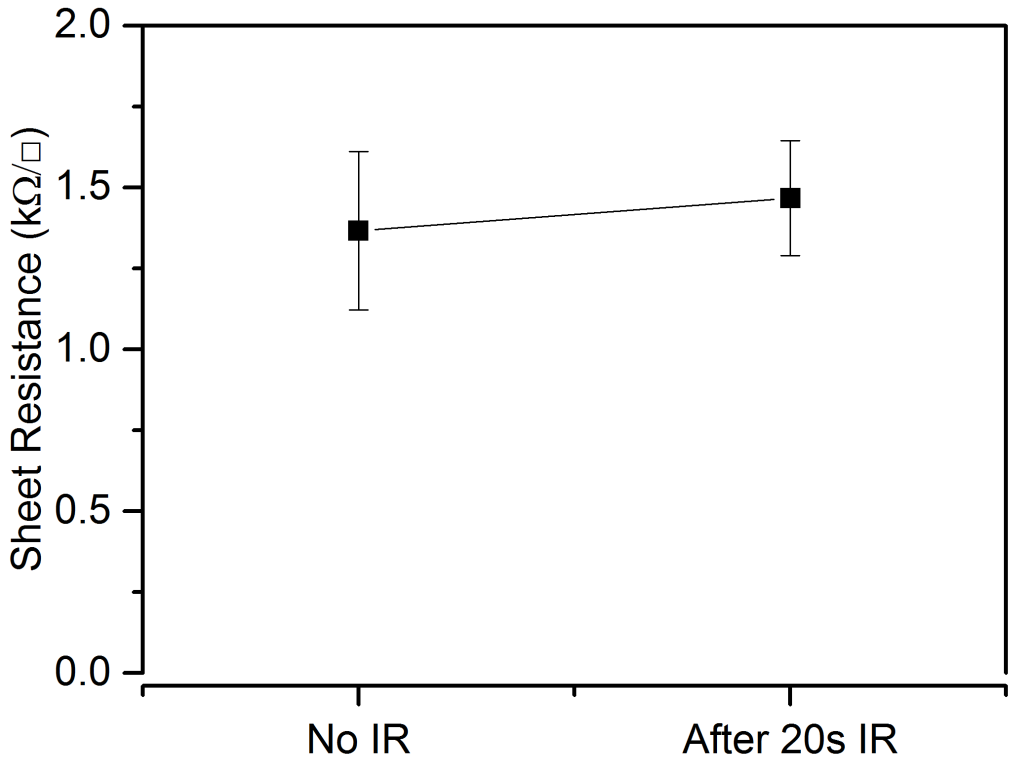

Figure 3.20. Sheet resistance of graphene on a 285nm SiO_2 substrate before and after 20s of IR irradiation.

3.7. Crumpled graphene field effect transistor

Lastly, we fabricated crumpled graphene FET arrays and characterized them in a solution-gated configuration (Figure 3.21a). The FET device consists of gold electrodes as the source and drain contacts and a crumpled graphene channel (Figure 3.21b), passivated with a polyimide layer (see Methods) with only the channel exposed to deionized water for gating.

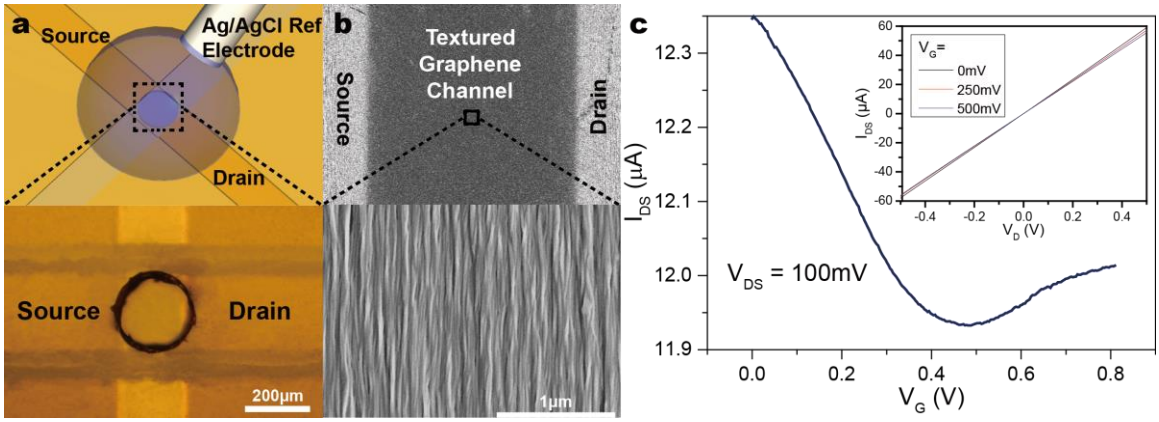

Figure 3.21. Solution (deionized water) gated crumpled graphene FET device. (a) Schematic drawing (top) and optical microscope images (bottom) show the operating configuration and structure of FET device with crumpled gold source and drain electrodes and a polyimide polymer passivation layer with a ~230 μm crumpled graphene channel. (b) SEM images show that the FET channel is composed of crumpled graphene whereas the source and drain electrodes are of crumpled gold film. (c) The transfer and output (inset) characteristics of a crumpled graphene FET.

Crumpled graphene FET devices were made by evaporating 50 nm thick gold electrodes through a shadow mask onto graphene transferred onto PS. After electrode deposition, the source and drain contacts are then defined by mechanically scratching the sample surface with a micromanipulator controlled tip, followed by thermally-induced texturing which yields the crumpled graphene channel along with crumpled gold source and drain electrodes. Finally, the entire device is passivated with a polyimide layer which has a single 230 μm pore that allows for solution-gating of the crumpled graphene channel region. FET I-V characteristics were measured with a digital sourcemeter (2614B, Keithley Instruments, OH) with an Ag/AgCl reference electrode (Harvard Instruments, MA) to gate the device through freshly generated deionized water. All measurements were performed in ambient conditions. Field-effect transistor measurements were performed with a probe station (PM8, SUSS Micro Tec, Germany) and a digital sourcemeter (2614B, Keithley Instruments, OH).

In calculating the field-effect mobilities, the transconductance was obtained by taking the linear slope (I_{DS}/V_G) of the I-V_G curve. The electric double layer capacitance (C_{DL}) and the quantum capacitance (C_Q ~28 $\mu F/cm^2$) were calculated for the estimation of total capacitance. To account for the effect of crumpled graphene roughness on the electric double layer capacitance, a shape factor of 1.15 was estimated based on COMSOL simulations. The effective crumpled graphene gate length (L) and width (W) from the physical device geometry were used for the field-effect mobility estimation.

At a water gate sweep between 0V to 0.8V using a Ag/AgCl reference electrode (Figure 3.21c), we observed ambipolar field-effect gating with estimated hole and electron field-effect mobilities of 497 and 157 cm^2/Vs, respectively, consistent with earlier literature in the device performance.[46]

3.8. Conclusion

Our results clearly show the capability to easily create 3D crumpled structures from otherwise 2D graphene using simple thermal treatment and IR irradiation. Not only are the crumpled morphologies tunable, but we also demonstrate the ability to form deterministic patterns with varying induced strain direction and amount, film thickness, and localized patterning. This thermally activated shape-memory polymer induced crumpling of graphene/graphite has several key advantages over earlier works. First, the simplicity of thermal processing allows deterministic tunability of crumple morphology and density over a large range of strains via simple processing parameters (duration, temperature, irradiation area, and mechanical constraints). Furthermore, our novel deformation mechanism allows for spatially controlled texturing via direct local patterning for the first time. Second, our proposed approach provides a simple and robust platform for studying the texturing and strain phenomena of a wide range of other novel 2D atomic-layer materials of recent interest, such as silicene, germanane, hBN, MoS_2, and other dichalcogenides.[47–

[49] The ubiquity, scalability, and low cost of polystyrene shape-memory polymers and the simplicity of thermal processing offers a pathway that is conducive to large-scale manufacturing of textured graphene/graphite devices (Figure 3.22 and Figure 3.23), circumventing costly lithographic pre-patterning and post-pressing deposition steps required in traditional feature forming techniques. To our knowledge, this study also represents the first to demonstrate a solution-gated, crumpled graphene FET device, and we believe that such studies will lead to potential 3D graphene electronics and bioelectronics in the future.

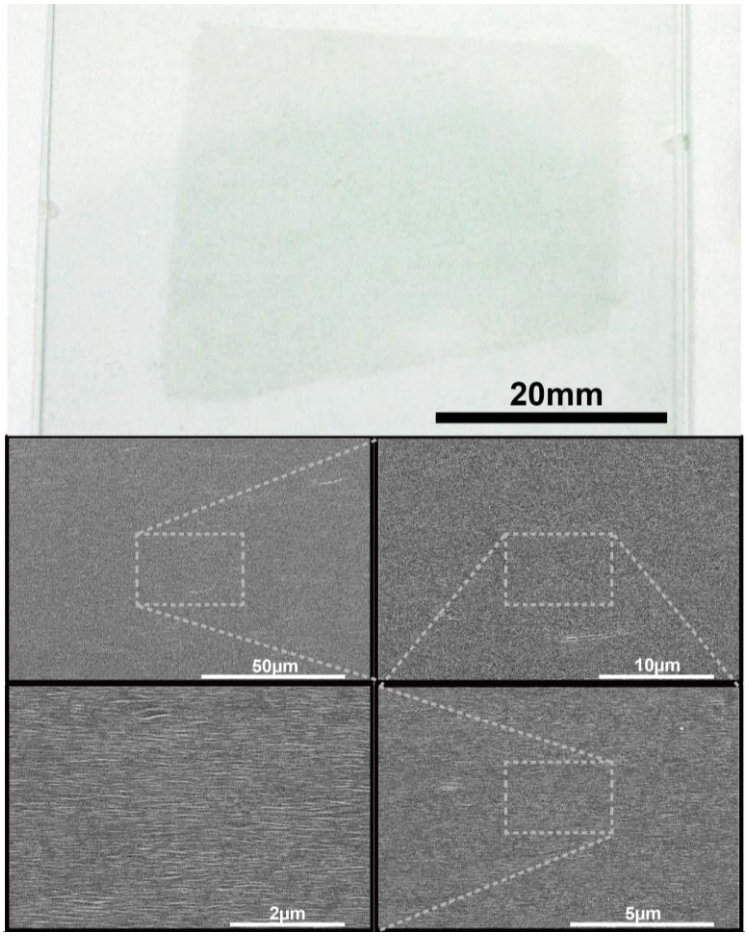

Figure 3.22. Large-area graphene and graphene crumples on PS. Photograph and SEM images of large area flat and uniaxially crumpled graphene, respectively. Photograph shows the capability of the direct transfer method up to the centimeter scale and SEM images show uniformity of graphene crumples spanning up to 100µm.

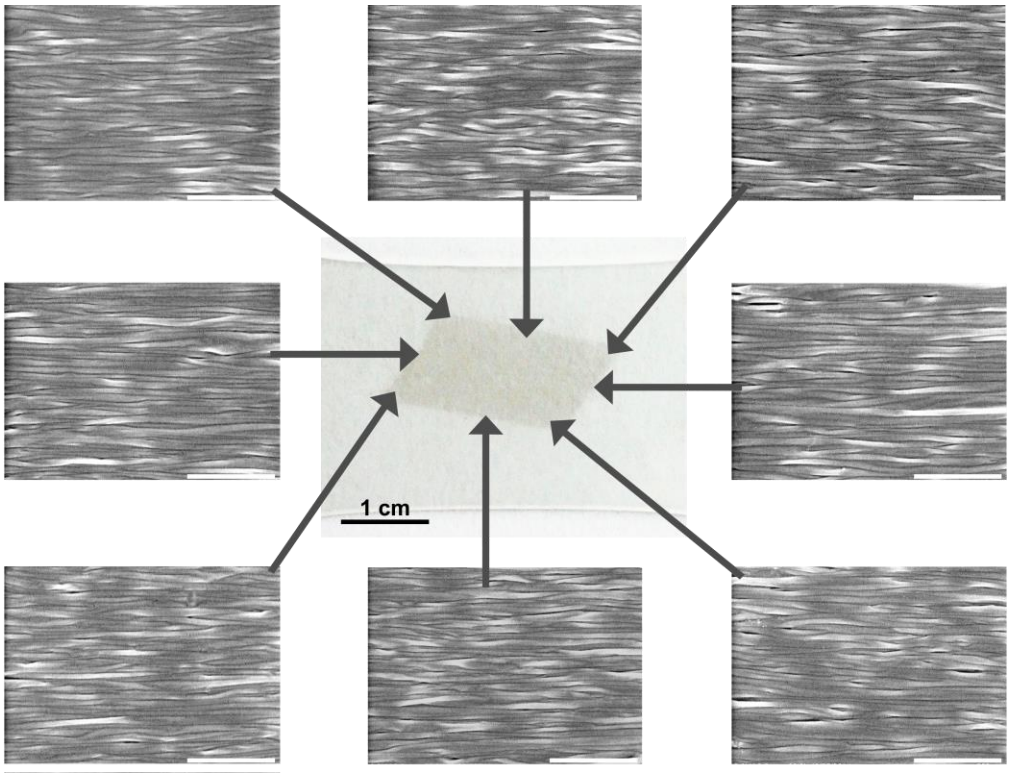

Figure 3.23. Uniformity of graphene crumples at various locations. SEM images taken at eight different locations on a centimeter-scale uniaxially crumpled graphene sample shows that the morphology is consistent and uniform across various locations on a given sample irrespective of its relative position or the size of the graphene film as a whole (all other scale bars 500nm).

In conclusion, we demonstrated the facile, single-step, controlled texturing of graphene and graphite into 3D crumples via thermally induced contractile deformation of an oriented PS substrate. We showed that the 3D texturing of both graphene and graphite can be modulated by varying simple processing parameters, and that the material integrity of graphene and graphite is maintained even up to induced macroscopic compressive strains as large as ~70%. Furthermore, we explored texturing of monolithic graphene-graphite patterns and showed that the continuous interfaces are preserved between graphene and graphite crumples. More notably, we investigated deterministic, spatially localized 3D patterning of graphene/graphite crumples which enables native creation of a mixture of flat/crumpled heterogeneous morphologies based on

graphene/graphite alone without any substrate pre-patterning or post-processing material deposition.[31] Finally, we demonstrate solution-gated, crumpled graphene FET device arrays. We believe our approach can be easily extended to a variety of other 2D materials (such as MoS_2 and other dichalcogenides),[47–50] and is much more amenable to large scale manufacturing of 3D graphene structures as compared to previously reported methods.[51] This direct patterning approach would enable monolithic integration of flat and textured graphene/graphite to realize mechanically robust and flexible advanced 3D biosensors in the future.[8]

3.9. Bibliography

(1) Novoselov, K. S.; Geim, A. K.; Morozov, S. V; Jiang, D.; Zhang, Y.; Dubonos, S. V; Grigorieva, I. V; Firsov, A. A. *Science* **2004**, *306*, 666–669.

(2) Zhang, Y.; Tan, Y.-W.; Stormer, H. L.; Kim, P. *Nature* **2005**, *438*, 201–204.

(3) Lee, C.; Wei, X.; Kysar, J. W.; Hone, J. *Science (New York, N.Y.)* **2008**, *321*, 385–388.

(4) Bolotin, K. I.; Sikes, K. J.; Jiang, Z.; Klima, M.; Fudenberg, G.; Hone, J.; Kim, P.; Stormer, H. L. *Solid State Communications* **2008**, *146*, 351–355.

(5) Seol, J. H.; Jo, I.; Moore, A. L.; Lindsay, L.; Aitken, Z. H.; Pettes, M. T.; Li, X.; Yao, Z.; Huang, R.; Broido, D.; Mingo, N.; Ruoff, R. S.; Shi, L. *Science (New York, N.Y.)* **2010**, *328*, 213–216.

(6) Schedin, F.; Geim, A. K.; Morozov, S. V; Hill, E. W.; Blake, P.; Katsnelson, M. I.; Novoselov, K. S. *Nature materials* **2007**, *6*, 652–655.

(7) Cohen-Karni, T.; Qing, Q.; Li, Q.; Fang, Y.; Lieber, C. M. *Nano letters* **2010**, *10*, 1098–1102.

(8) Choi, J.; Wang, M. C.; Cha, R. Y. S.; Park, W. Il; Nam, S. *Biomedical Engineering Letters* **2014**, *3*, 201–208.

(9) Bae, S.; Kim, H.; Lee, Y.; Xu, X.; Park, J.-S.; Zheng, Y.; Balakrishnan, J.; Lei, T.; Kim, H. R.; Song, Y. Il; Kim, Y.-J.; Kim, K. S.; Ozyilmaz, B.; Ahn, J.-H.; Hong, B. H.; Iijima, S. *Nature nanotechnology* **2010**, *5*, 574–578.

(10) Reina, A.; Jia, X.; Ho, J.; Nezich, D.; Son, H.; Bulovic, V.; Dresselhaus, M. S.; Kong, J. *Nano letters* **2009**, *9*, 30–35.

(11) Zang, J.; Ryu, S.; Pugno, N.; Wang, Q.; Tu, Q.; Buehler, M. J.; Zhao, X. *Nature materials* **2013**, *12*, 321–325.

(12) Whitby, R. L. D. *ACS nano* **2014**, *8*, 9733–9754.

(13) Guinea, F.; Katsnelson, M.; Vozmediano, M. *Physical Review B* **2008**, *77*, 075422.

(14) Guinea, F.; Katsnelson, M. I.; Geim, A. K. *Nature Physics* **2009**, *6*, 30–33.

(15) Pereira, V.; Castro Neto, A. *Physical Review Letters* **2009**, *103*, 046801.

(16) Levy, N.; Burke, S. A.; Meaker, K. L.; Panlasigui, M.; Zettl, A.; Guinea, F.; Castro Neto, A. H.; Crommie, M. F. *Science (New York, N.Y.)* **2010**, *329*, 544–547.

(17) Guinea, F.; Geim, A. K.; Katsnelson, M. I.; Novoselov, K. S. *Physical Review B* **2010**, *81*, 035408.

(18) Ruoff, R. *Nature* **2012**, *483*, S42.

(19) Park, J.-U.; Nam, S.; Lee, M.-S.; Lieber, C. M. *Nature materials* **2012**, *11*, 120–125.

(20) Cranford, S. W.; Buehler, M. J. *Physical Review B* **2011**, *84*, 205451.

(21) Luo, J.; Jang, H. D.; Sun, T.; Xiao, L.; He, Z.; Katsoulidis, A. P.; Kanatzidis, M. G.; Gibson, J. M.; Huang, J. *ACS nano* **2011**, *5*, 8943–8949.

(22) Bissett, M. A.; Tsuji, M.; Ago, H. *The Journal of Physical Chemistry C* **2013**, *117*, 3152–3159.

(23) Bissett, M. A.; Konabe, S.; Okada, S.; Tsuji, M.; Ago, H. *ACS Nano* **2013**, *7*, 10335–10343.

(24) Srivastava, D.; Brenner, D. W.; Schall, J. D.; Ausman, K. D.; Yu, M.; Ruoff, R. S. *The Journal of Physical Chemistry B* **1999**, *103*, 4330–4337.

(25) Frackowiak, E.; Béguin, F. *Carbon* **2001**, *39*, 937–950.

(26) Zhang, S.; Pan, N. *Journal of Materials Chemistry A* **2013**, *1*, 7957–7962.

(27) Zang, J.; Zhao, X.; Cao, Y.; Hutchinson, J. W. *Journal of the Mechanics and Physics of Solids* **2012**, *60*, 1265–1279.

(28) Fasolino, A.; Los, J. H.; Katsnelson, M. I. *Nature materials* **2007**, *6*, 858–861.

(29) Fu, C.-C.; Grimes, A.; Long, M.; Ferri, C. G. L.; Rich, B. D.; Ghosh, S.; Ghosh, S.; Lee, L. P.; Gopinathan, A.; Khine, M. *Advanced Materials* **2009**, *21*, 4472–4476.

(30) Grimes, A.; Breslauer, D. N.; Long, M.; Pegan, J.; Lee, L. P.; Khine, M. *Lab on a chip* **2008**, *8*, 170–172.

(31) Liu, Y.; Boyles, J. K.; Genzer, J.; Dickey, M. D. *Soft Matter* **2012**, *8*, 1764.

(32) Felton, S. M.; Tolley, M. T.; Shin, B.; Onal, C. D.; Demaine, E. D.; Rus, D.; Wood, R. J. *Soft Matter* **2013**, *9*, 7688.

(33) Bang, J.; Choi, J.; Xia, F.; Kwon, S. S.; Ashraf, A.; Park, W. Il; Nam, S. *Nano Letters* **2014**, *14*, 3304–3308.

(34) Felton, S.; Tolley, M.; Demaine, E.; Rus, D.; Wood, R. *Science* **2014**, *345*, 644–646.

(35) Wang, Y.; Yang, R.; Shi, Z.; Zhang, L.; Shi, D.; Wang, E.; Zhang, G. *ACS nano* **2011**, *5*, 3645–3650.

(36) Zhu, W.; Low, T.; Perebeinos, V.; Bol, A. A.; Zhu, Y.; Yan, H.; Tersoff, J.; Avouris, P. *Nano letters* **2012**, *12*, 3431–3436.

(37) Pan, Z.; Liu, N.; Fu, L.; Liu, Z. *Journal of the American Chemical Society* **2011**, *133*,

17578–17581.

(38) Khang, D.-Y.; Jiang, H.; Huang, Y.; Rogers, J. A. *Science (New York, N.Y.)* **2006**, *311*, 208–212.

(39) Jiang, H.; Sun, Y.; Rogers, J. A.; Huang, Y. *Applied Physics Letters* **2007**, *90*, 133119.

(40) Chen, X.; Hutchinson, J. W. *Journal of Applied Mechanics* **2004**, *71*, 597–603.

(41) Jiang, T.; Huang, R.; Zhu, Y. *Advanced Functional Materials* **2013**, *24*, 396–402.

(42) Mohiuddin, T.; Lombardo, A.; Nair, R.; Bonetti, A.; Savini, G.; Jalil, R.; Bonini, N.; Basko, D.; Galiotis, C.; Marzari, N.; Novoselov, K.; Geim, A.; Ferrari, A. *Physical Review B* **2009**, *79*, 205433.

(43) Bao, W.; Miao, F.; Chen, Z.; Zhang, H.; Jang, W.; Dames, C.; Lau, C. N. *Nature nanotechnology* **2009**, *4*, 562–566.

(44) Martins, L. G. P.; Song, Y.; Zeng, T.; Dresselhaus, M. S.; Kong, J.; Araujo, P. T. *Proceedings of the National Academy of Sciences of the United States of America* **2013**, *110*, 17762–17767.

(45) Shioya, H.; Craciun, M. F.; Russo, S.; Yamamoto, M.; Tarucha, S. *Nano Letters* **2014**, *14*, 1158–1163.

(46) Kim, B. J.; Jang, H.; Lee, S.-K.; Hong, B. H.; Ahn, J.-H.; Cho, J. H. *Nano letters* **2010**, *10*, 3464–3466.

(47) Novoselov, K. S.; Jiang, D.; Schedin, F.; Booth, T. J.; Khotkevich, V. V; Morozov, S. V; Geim, A. K. *Proceedings of the National Academy of Sciences of the United States of America* **2005**, *102*, 10451–10453.

(48) Novoselov, K. S.; Fal′ko, V. I.; Colombo, L.; Gellert, P. R.; Schwab, M. G.; Kim, K. *Nature* **2012**, *490*, 192–200.

(49) Geim, A. K.; Grigorieva, I. V. *Nature* **2013**, *499*, 419–425.

(50) Castellanos-Gomez, A.; Roldan, R.; Cappelluti, E.; Buscema, M.; Guinea, F.; van der Zant, H. S. J.; Steele, G. A. *Nano Letters* **2013**, *13*, 5361–5366.

(51) Reserbat-Plantey, A.; Kalita, D.; Han, Z.; Ferlazzo, L.; Autier-Laurent, S.; Komatsu, K.; Li, C.; Weil, R.; Ralko, A.; Marty, L.; Guéron, S.; Bendiab, N.; Bouchiat, H.; Bouchiat, V. *Nano letters* **2014**, *14*, 5044–5051.

Chapter 4. Heterogeneous elastic strain engineering of atomically-thin 2D materials

This chapter is adopted in part from work published in *2D Materials*, **15 (3)**, 1829-1835 (2018).

4.1. Introduction

Ever since graphene's explosive popularity, intensive research is now elucidating an ever-expanding genome of two-dimensional (2D) materials, spanning insulators to superconductors. While graphene is the prototypical semimetal (zero bandgap semiconductor), recent progress has yielded a plethora of novel semiconducting and superconducting transition metal chalcogenides, insulators (hexagonal boron nitride), and other elemental 2D materials (phosphorene, silicene, etc).[1–3] As 2D graphene "analogs", this ever-growing family of 2D layered materials all share the common property of vanishing flexural rigidity due to their atomic thicknesses, which presents simultaneously unique challenges yet also new opportunities for exploring processing-structure-property relations at such extreme length scales and subjected to large deformations.[4] In particular, atomically-thin semiconducting transition metal chalcogenides (TMDCs) that are three-atoms thick are similarly amenable as graphene to large out-of-plane deformations due to their extremely low bending rigidities and van der Waals nature.

Elastic strain engineering allows for simple, scalable, and reversible modulation of the bandgap and conductance of robust atomically-thin 2D materials, which is difficult to achieve with conventional bulk semiconductor materials due to the limits of fracture and plastic deformation.[5] We realize for the first time 2D TMDC lateral superlattices displaying highly tunable, well-organized, periodic, and anisotropic optoelectronic properties and structure enabled by large-scale, heterogeneous elastic strain engineering. Through tailoring the relative substrate composition, stiffness, and thickness mismatch, of the underlying deformable substrate, three-dimensional (3D)

TMDC features spanning tens of nanometers to few-microns are deterministically obtainable through instability-driven deformation of TMDCs on the centimeter-scale without any lithographic patterning. This self-assembly approach to forming various nano/micro-structured semiconducting TMDCs via controlled substrate transformation offers a unique avenue for creating periodic, heterogeneous, and emergent material properties across a broad range of length-scales. Due to material agnostic nature of this processing technique, this provides a versatile platform for a variety of optoelectronic applications and study of emergent phenomena including active tuning of carrier and phonon behavior, local band structure, excitonic funneling, flexoelectricity, spintronics and valleytronics, self-assembly, and enhanced basal plane photocatalysis, etc.

4.2. Heterogeneous strain in semiconducting thin-films and 2D materials

Strain engineering has been ubiquitously adopted to achieve higher carrier mobilities in silicon-based transistors for the past two decades. Unlike conventional bulk semiconductors, atomically-thin TMDCs, as semiconducting graphene analogs, exhibit very large ultimate strains (in excess of 20%) and are amenable to large flexural deformations due to their extremely low bending rigidities.[6,7] This enables the band structure of semiconducting TMDCs to be easily tuned by elastic strain, without the need for chemical or electrostatic doping.[8–10] Such facile tuning of the intrinsic optoelectronic properties in atomically thin semiconducting TMDCs (in addition to a large variety of intrinsic bandgaps of the various known TMDCs) opens the door for new approaches in efficient light harvesting and photo-detection across a wide and tunable range of wavelengths.

As a prototypical 2D TMDC, molybdenum disulphide is semiconducting layered material that is also widely used for its tribological properties. The most stable form of monolayer molybdenum disulphide (MoS_2) is of a trigonal prismatic structure (2H) and consists of hexagonal planes of sulphur and molybdenum. MoS_2 transitions from an indirect to a direct bandgap semiconductor at

the monolayer limit due to changes to orbital interactions along the plane-normal direction. Similarly, elastic strain can tune the in-plane bonds and orbital interactions, thereby affecting the electronic structure of monolayer MoS_2. As the magnitude of the direct bandgap in MoS_2 is only slightly smaller than that of the indirect gap,[11] relatively moderate amount of strain can cause a direct-to-indirect transition (literature values vary from 1 to 5% uniaxial strain)[12,13] and even a semiconducting-to-metallic transition (~10% biaxial).[14]

Many studies have documented the effect of strain on the electronic, vibrational, and chemical properties of monolayer MoS_2 and other similar 2D TMDCs through empirical investigations and first-principals calculations. While there is some quantitative dispersion on the magnitude of shift, it is well known that increasing tensile strain weakens in-plane interatomic bonds which correspondingly lowers the direct bandgap energy and reduces the effect carrier masses (high mobility) due to the reduced orbital overlap and hybridization.[15,16]

By draping MoS_2 over a lithographically patterned nanocone array, Li *et al.* were able to achieve large-scale indentation arrays which induced periodic strain profiles.[17] The biaxial tensile strains of up to 0.56% redshift the dominant luminescence peak (direct optical bandgap) by up to ~50 meV [18], while enabling excitation migration over hundreds of nanometers. Brotons-Gisbert et al. adopted a similar indentation approach with SiO_2 nanoparticles to heterogeneously strain nanometer thick InSe films.[19]

Castellanos-Gomez et al. and Yang et al. created locally strained buckle delaminated structures of multilayer MoS_2 and $ReSe_2$ ribbons, respectively, on top of elastomeric substrates.[8,20] The uniaxially buckled few-layer MoS_2 exhibited photoluminescence redshift of up to 90 meV for ~2.5% tensile strain at the top layer on the feature apex. Analogously for buckle delaminated

multilayer $ReSe_2$, Yang et al. observed a 70 meV decrease in the direct gap energy for a tensile strain of ~1.64%.

In monolayer MoS_2 nanoribbons, Yu *et al.* found that bending induces hole localization in bent armchair-edged ribbon, which results in a reduction of the edge-to-edge p-type conductivity as bending curvature increases (Figure 4.1).[21] Yet for both armchair and zigzag GNRs, the bandgap changes little, which makes them suitable for flexible applications where consistent electrical properties are needed. Nonetheless, the valence band maximum (VBM) and conduction band minimum (CBM) both decrease with increasing curvature, which allows for tuning of GNRs' work function. Therefore, band tuning via local strain engineering avoids the problems of crystal defects and reduced carrier mobility associated with conventional doping techniques.

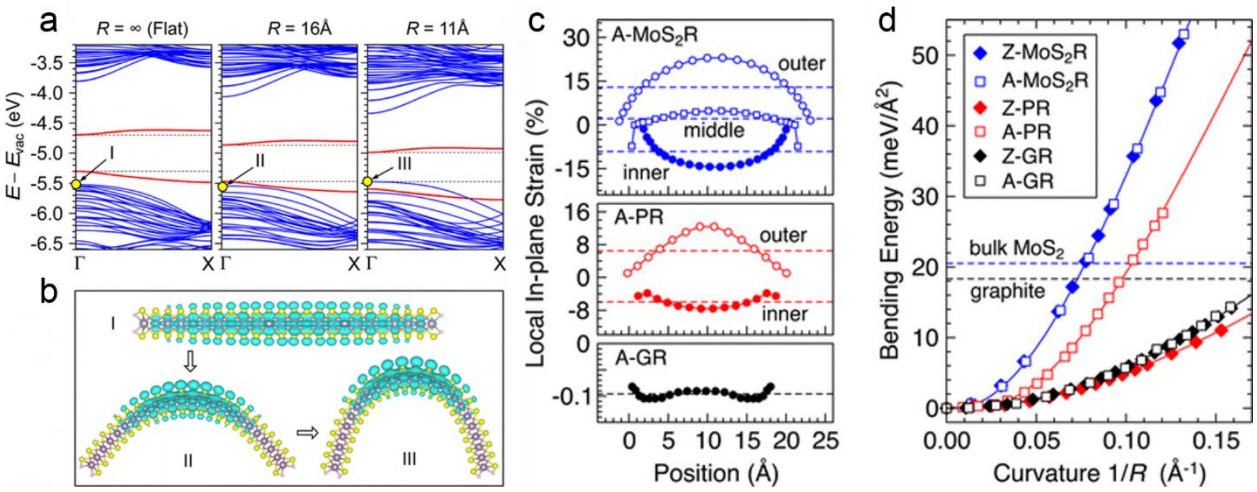

Figure 4.1. (a-b) Band structure modulation of armchair MoS_2 nanoribbons as a function of bending curvature. The horizontal dashed lines represent the CBM and VBM while the red bands are the two-fold degenerate edge-state bands. (c) Local in-plane strain profile across the armchair 2D material nanoribbons (MoS_2, phosphorene, graphene) and concomitant bending energy as a function of the bending curvature. (d) The bending energy as a function of bending curvature increases at different rates depending on the nanoribbon chirality. Dashed horizontal lines indicate the vdW interlayer binding energy of bulk molybdenite and graphite. Adapted with permission from reference 21. *Copyright 2016 American Chemical Society.*

4.3. Lateral superlattices of monolayer semiconducting transition metal dichalcogenides (TMDCs) via elastic strain engineering

We have developed a strategy to self-assemble 2D TMDC into lateral superlattices of well-organized, periodic, and spatially varying optoelectronic properties which are enabled by large-scale, heterogeneous elastic strain generated via thermally-activated shape-memory polymers. Through tailoring the relative substrate composition, stiffness, and thickness mismatch, three-dimensional features that span from tens of nanometers to few-microns may be deterministically created through wrinkling and buckling-delamination of TMDCs without any lithographic patterning and on the centimeter-scale. The periodic strain gradients induce controllable, heterogeneous, and anisotropic optoelectronic and mechanical behaviour in a lateral superlattice fashion.

To fabricate the samples, bulk synthetically grown MoS_2 crystals were mechanically exfoliated using scotch tape to generate monolayer MoS_2. Exfoliated MoS_2 is preferred to CVD MoS_2 as the state-of-the-art of CVD-grown MoS_2 nonetheless exhibits random spatially distributed inhomogeneity and resultant Stokes shift in the photoluminescence (optical bandgap) due to thickness inhomogeneity, unintended doping, interfacial contaminants, residual seeding compounds, and charge traps, etc. The freshly cleaved MoS_2 were pressed into contact with a clean SiO_2 wafer that has been treated by Pirhana solution and oxygen plasma, and the adhesive tape is slowly peel away to yield a random distribution of flakes of varying thicknesses and morphologies (Figure 4.2). Any resultant monolayer regions were identified under optical microscope by brightfield contrast and the adjacent multilayer regions were removed by manual abrasion using a probe tip to facilitate subsequent steps.

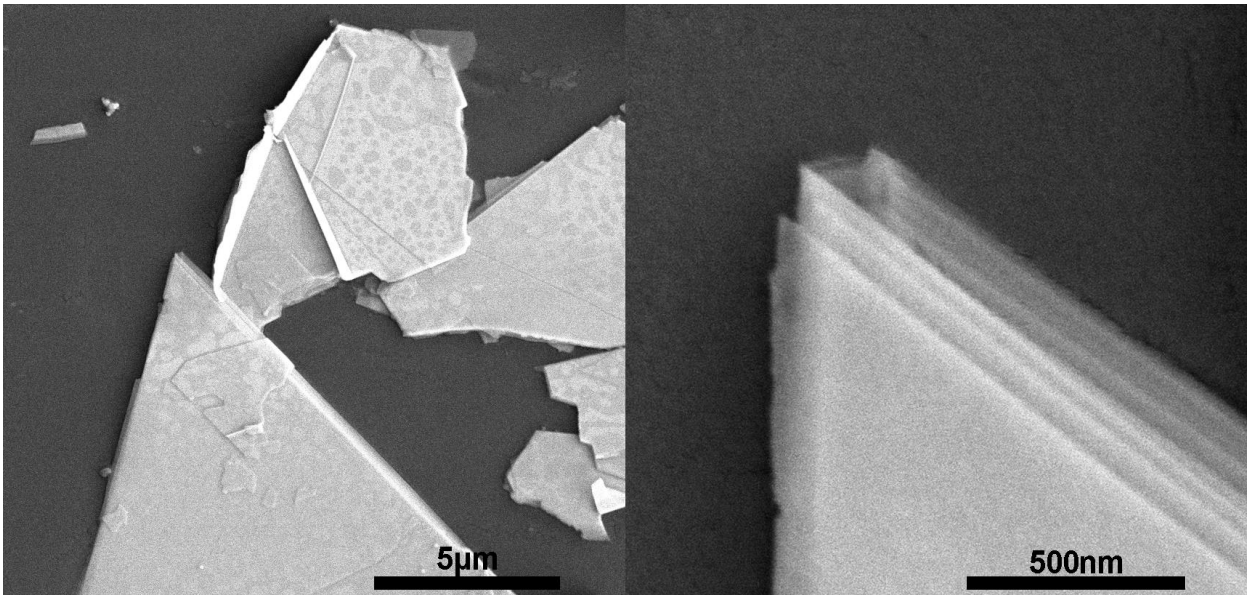

Figure 4.2. SEM of mechanically exfoliated MoS_2 flakes on PS. Visible edge states and layered stacking morphology are indicative of its 2H hexagonal crystal structure.

While the morphology of the monolayer flake edges gives some indication of the chiral orientation of the MoS_2 relative to the substrate, knowledge of the crystallographic direction is not critical to the experimental results since MoS_2 exhibits isotropic in-plane elasticity for small strains due to its three-fold rotational symmetry (D_{3h}).[12,17] Where necessary, the crystallographic orientation of monolayer MoS_2 may be inferred from the angular dependence and 6-fold symmetry of the second harmonic generation signal due to its non-centrosymmetry (D_{3h} symmetry). The reflected second harmonic signal maxima and minima correspond to polarization along the armchair and zigzag directions, respectively.[22,23]

Strain is applied to the MoS_2 flake via van der Waals coupling to the polymeric substrate's continuous and periodic sinusoidal deformations. This is achieved by first cleaning the as-exfoliated MoS_2 on the SiO_2 wafer by soaking for a few hours in hot acetone to remove adhesive residue left behind during the exfoliation process. A thin PMMA handle layer is then spuncoat onto the MoS_2/SiO_2, prior to floating the sample on top of a hot potassium hydroxide (KOH)

solution to remove the thin SiO_2 interface and release the PMMA/MoS_2 film. The free floating PMMA/MoS_2 film is then transferred iteratively into multiple baths of deionized water and left for a few hours to completely remove any KOH residue, prior to being transferred onto a thin film of PDMS spin coated (~5 um thick) onto a shape memory polystyrene substrate.

After the PMMA/MoS_2 film has dried and adhered to the PDMS surface, the PMMA handle layer is removed using acetic acid and then rinsed in DI water and IPA. Immediately following PMMA handle layer removal, the entire sample surface is encapsulated with an IPA-diluted spin-on-glass (SOG) methyl siloxane polymer solution (Accuglass T11 211) (Figure 4.3). The SOG solution specifies curing at temperatures in excess of 400 ℃, but the polymeric substrate used here and the volatility of MoS_2 at elevated temperatures limits our sample preparation to 80 ℃ for extended periods of time. This resulted in a glassy encapsulation surface layer that is sufficiently stiff (but not fully cured) to induce conformal surface wrinkling with the MoS_2 conformally sandwiched between the SOG and underlying PDMS film upon thermal activation and bulk straining of the underlying shape memory polystyrene substrate. For buckle delaminated crumpled MoS_2 features, the process is the same as described above but without a PDMS interlayer and without an SOG encapsulation top layer.

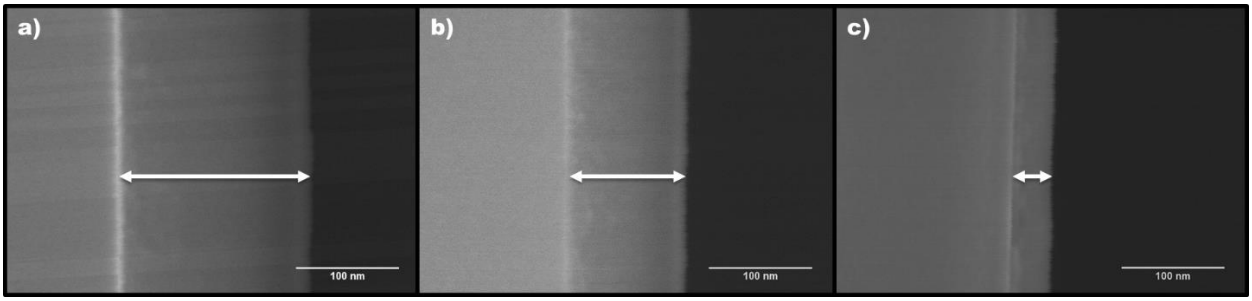

Figure 4.3. Cross-section SEM calibration of varying thicknesses of spin-on-glass coated onto a silicon wafer. Samples were spun coat at 8000 rpm for 90s of SOG used as-is (a) and diluted with 0.5 parts (b) and 3 parts (c) isopropanol.

When the macroscopic compressive strain reaches a critical strain (ε_c), the stiff surface layer becomes unstable and results in a conformally wrinkled morphology, where the critical strain is dictated by the relative moduli mismatch between the still surface layer and the compliant substrate (Figure 4.4).

$$\varepsilon_c = \frac{1}{4}\left(3\,\bar{E}_s/\bar{E}_f\right)^{2/3}$$

Where

$$\bar{E}_s = E_s/(1-v_s^2) \text{ and } \bar{E}_f = E_f/(1-v_f^2)$$

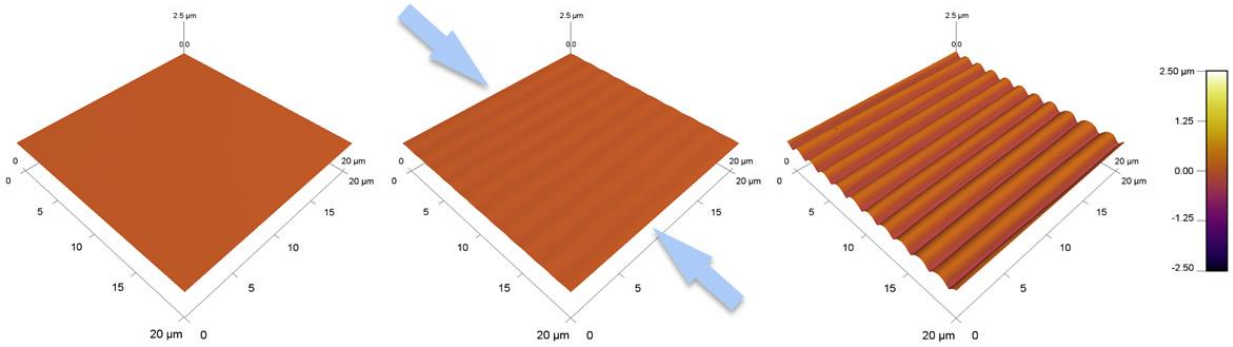

Figure 4.4. Morphology evolution due to increasing macroscale compressive strain inducing surface wrinkling of a stiff film on a compliant substrate.

This yields a uniform grating-like pattern on the centimeter scale with undulating sinusoidal profiles consisting of periodic peaks and troughs on the micron scale described by the function,

$$w = A\cos\left(\frac{2\pi x}{\lambda}\right)$$

Where A and λ describe the amplitude and wavelength of the wrinkled profile, respectively takes on initial values (A_0, λ_0) of

$$\lambda_0 = 2\pi h_f\left[\bar{E}_f/(3\bar{E}_s)\right]^{1/3}$$

$$A_0 = h_f\sqrt{\varepsilon_{pre}/\varepsilon_c - 1}$$

Further compressive strain more than the critical strain ε_c evolves the structure (Figure 4.4) such that the amplitude increases and the wavelength decreases (wrinkles densify), such that

$$\lambda = \frac{\lambda_0}{(1+\varepsilon_{pre})\left(1+\ \xi\right)^{1/3}}$$

$$A = \frac{A_0}{\sqrt{1+\varepsilon_{pre}}\left(1+\ \xi\right)^{1/3}}$$

Where ξ is a non-dimensionalized strain factor given by

$$\xi = 5\varepsilon_{pre}(1+\varepsilon_{pre})/32$$

In the trough or valley regions of the wrinkles, the SOG is deformed in a concave fashion (from the perspective of the top surface) to place the interfacial monolayer MoS_2 in in-plane tensile strain (Figure 4.5). Conversely, in the peak or apex regions of the wrinkles, the SOG is deformed in a convex fashion (from the perspective of the top surface) to place the interfacial monolayer MoS_2 in in-plane compressive strain. At the atomic level, the heterogeneous local in-plane tensile strain increases the Mo-Mo and Mo-S bond lengths while contracting the S-S layer separation, causing reduced orbital hybridization and d-orbital bandwidth and thus a corresponding reduction in the band gap, and vice versa for compressive strain.

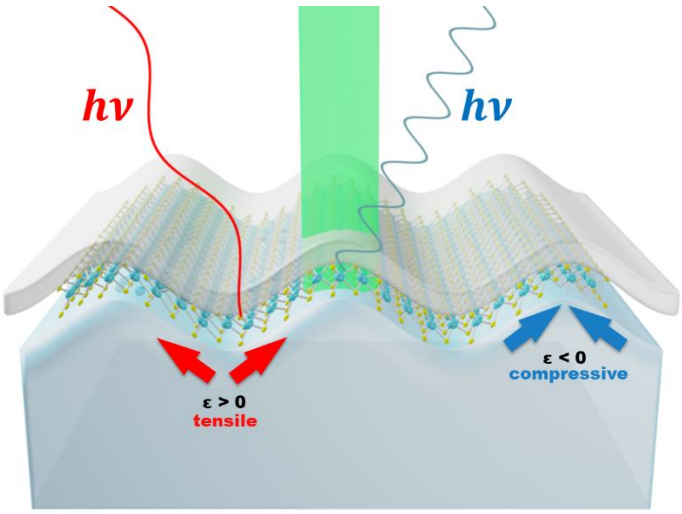

Figure 4.5. Continuous band banding of monolayer MoS_2 via encapsulation conformal wrinkling and elastic strain engineering in a lateral superlattice configuration. The MoS_2 in the convex peak regions are in compression (photoluminescence blue-shifted), while those in the concave regions are in tension (photoluminescence red-shifted).

The generality of using surface instability induced corrugations to impart periodic and heterogeneous strain profiles afford the versatility in tuning the magnitude of strain, characteristic lengths, and strain gradient. Specifically, we explored the effect of progressively increasing the macroscale uniaxial strain resulting in gradual morphological evolution of the local strain profile and also the effects of tuning the top SOG layer thickness to realize different wrinkling length scales.

Due to its bright photoluminescence at the monolayer limit, micro-photoluminescence represents a versatile method to probe the optical emission of MoS_2.[24] White light spectroscopy also presents a useful tool to study the absorption spectra of MoS_2. Diffraction-limited micro-Raman and micro-Photoluminescence spectroscopy of superlattices with micron-sized features show large tunability in the local optical bandgap and strain confinement, whereas the analogous nanoscale superlattices show large polarization dependence in overall Raman and photoluminescence response.

The A and B emission peaks (at ~1.90 eV and ~2.05 eV, respectively) both correspond to excitons associated with the direct-gap transitions around the K-point, whereas the much weaker I emission peak (~1.55 eV) results from the indirect-gap transition and is only observed in bilayers or thicker (Figure 4.6). The A-B exciton splitting in monolayer MoS_2 is independent of small amounts of strain since it corresponds to the spin-orbit splitting of the lowest energy valence bands, which originates from the interior parts of the atoms and thus insensitive to changes in the molecular bond lengths.[25]

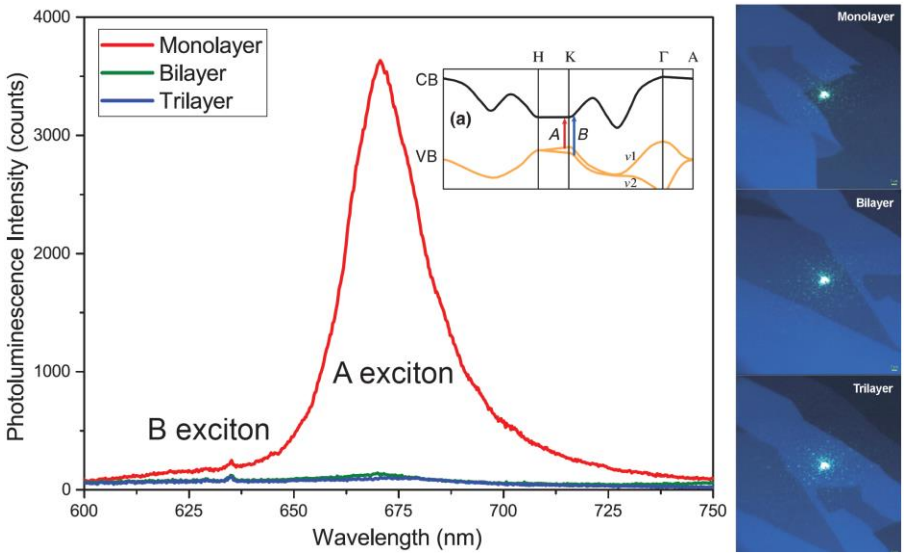

Figure 4.6. Photoluminescence of mechanically exfoliated mono-, bi-, and tri-layer MoS_2 on PS. The A exciton arising from the direct gap transition at the K point is drastically enhanced at the monolayer limit.

It is noted that while the binding energies of neutral exciton and charged trion are strong in monolayer MoS_2 due to reduced dielectric screening (>20 meV at room temperature), they are mostly strain independent.[11,26–28] Therefore, the observed changes to the photoluminescence emission spectra are mainly attributed to the strain-induced changes to the electronic band structure (shifts in optical band gap correspond to changes in the fundamental band gap, and not due to changes to the exciton binding energies) and thus accessible by the photoluminescence spectra

(Figure 4.7). Here, the bands near the Fermi level consist primarily of molybdenum's 4d and sulphur's 3p orbitals, and the direct-gap is dictated by the Mo4d-S3p hybridization and d-manifold splitting.

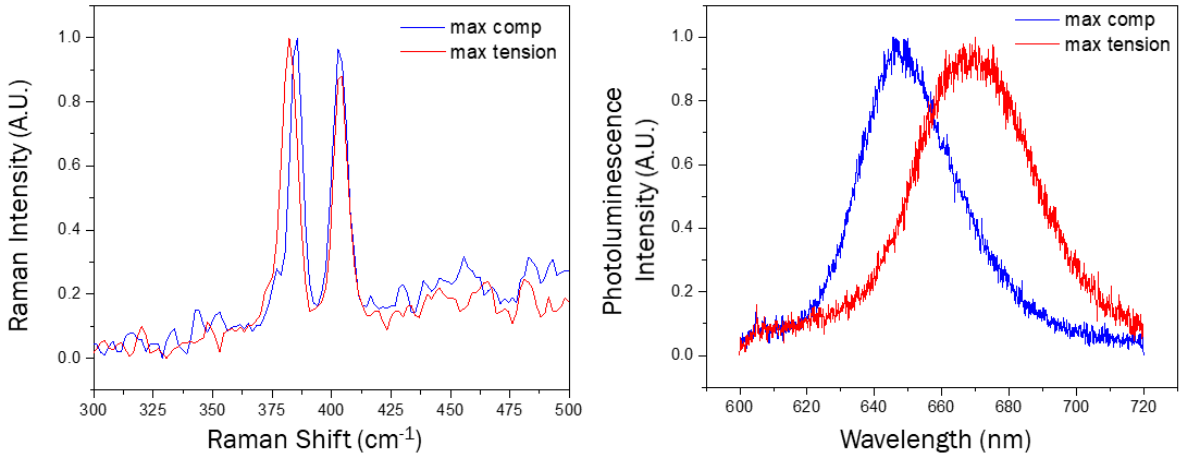

Figure 4.7. Strain induced shift in the Raman and photoluminescence spectra of monolayer MoS_2. Tensile strains red-shift both the in-plane E' vibrational mode and also the A peak corresponding to the direct gap transition at the K point.

By rastering line scan of the photoluminescence spectra across the undulations of the wrinkled profile (along the grating k-vector) to generate a spectrogram of the photolumescence spectra, we observe a continuous and periodic shift in the A peak position and thus spatially-varying band bending, indicative of the imparted strain (Figure 4.8). In particular, the as-prepared planar sample exhibits a constant A peak position at ~655 nm. Upon application of progressively larger macroscopic uniaxial strain in excess of the critical strain, the wrinkled structure evolves taller in height and slightly tighter in wavelength, leading to tighter radii of curvature, higher strain difference, and a larger spectral dispersion in the A peak position.

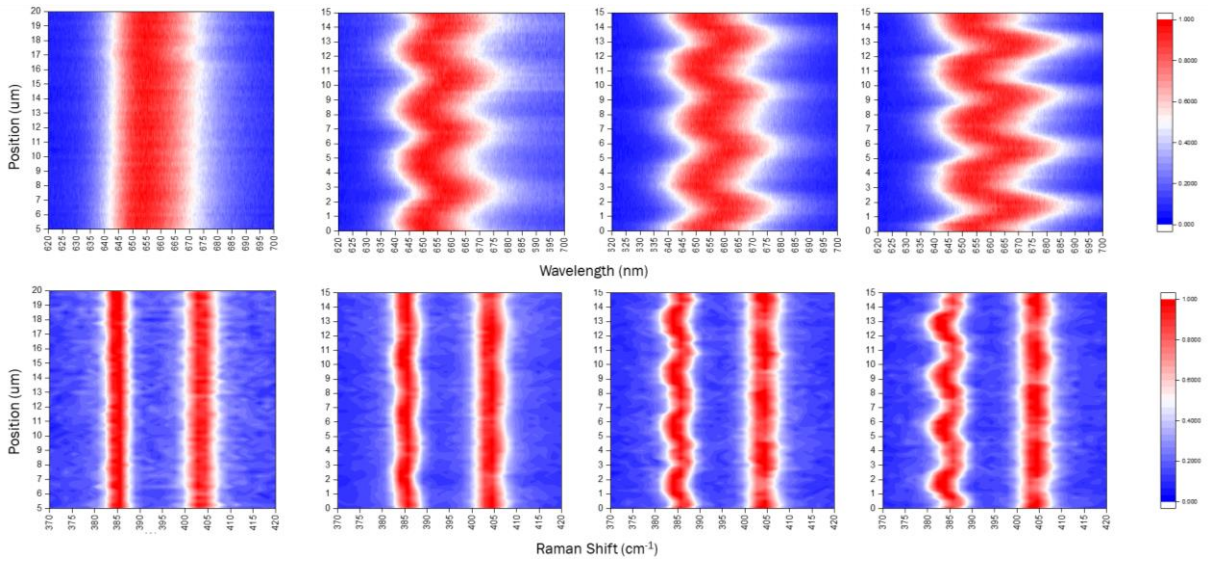

Figure 4.8. Line-mapped photoluminescence (top panels) and Raman (bottom panels) spectral evolution as the sample is being subjected to increasing amounts of macroscopic strain: 0%, 3%, 6%, 9%. Colour scale denotes normalized spectral intensity.

Here in the case of progressively imparted larger strains to the sample, we see that the photoluminescence and Raman spectra evolve to exhibit larger spectral dispersion (difference between most red-shifted and most blue-shift) due to increased wrinkling amplitude. However, the characteristic length scale between the compressive and tensile regions remain relatively unchanged. Since the shift of the Raman E_{2g} is poorly resolved due to limits of the spectral resolution (and no peak splitting was observed), we rely on the measurement of the photoluminescence to determine the actual strain in the MoS_2. Here, the maximum red-shifted and blue-shifted A exciton peaks reached ~675 nm and ~645 nm respectively. Calibrating against a linear shift of ~45 meV at the small strain regime. Taking the initial peak position at ~660 nm, these values correspond to a tensile strain of ~0.93% and compressive strain of ~0.97% in the MoS_2 at the trough and peak regions, respectively.[29–31] These values underestimate the peak strains given by the analytical relationship,[32]

$$\varepsilon_{peak} = 2\sqrt{\varepsilon_{pre}\varepsilon_c}\frac{(1+\zeta)^{1/3}}{\sqrt{1+\varepsilon_{pre}}}$$

Which yields a peak strain of ~2.2% given a substrate PDMS modulus of 1.5 MPa, an SOG modulus of 14 GPa (75 nm thick), and a macroscopic compression of 9% strain. Here, the expression gives the peak strains sustained in the stiff SOG film layer, which occurs at the very top and bottom strands of the stiff SOG layer wrinkles. This quantitative disparity (~1% measured vs ~2% calculated) between the anticipated strain and that actually corroborated by the photoluminescence shift may be attributed to imperfect interfacial shear transfer of the strain and slippage across the SOG-MoS_2 and PDMS-MoS_2 interface.

One of the most unique phenomena enable by such an elastically strained graded band structure construct is the possibility to realize room temperature exciton funneling and flexoelectricity. A prerequisite to realizing these novel phenomena in low-dimensional systems is the deterministic control over the spatial strain gradient and strain distribution by manipulating the magnitude and direction of band bending to match the exciton lifetime and drift length, etc. To tune the characteristic length scale (superlattice wavelength) of the wrinkled morphology (Figure 4.9), other material parameters may be affected in addition to the aforementioned application of progressive larger macroscale strain. These include changing the PDMS interlayer stiffness (thickness is assumed to be semi-infinite compared to the MoS_2 and SOG), the encapsulating SOG stiffness, and its thickness. We systemically tune the superlattice wavelength by encapsulating the MoS_2 with SOG of varying thickness by diluting the SOG solution with IPA prior to spin coating.

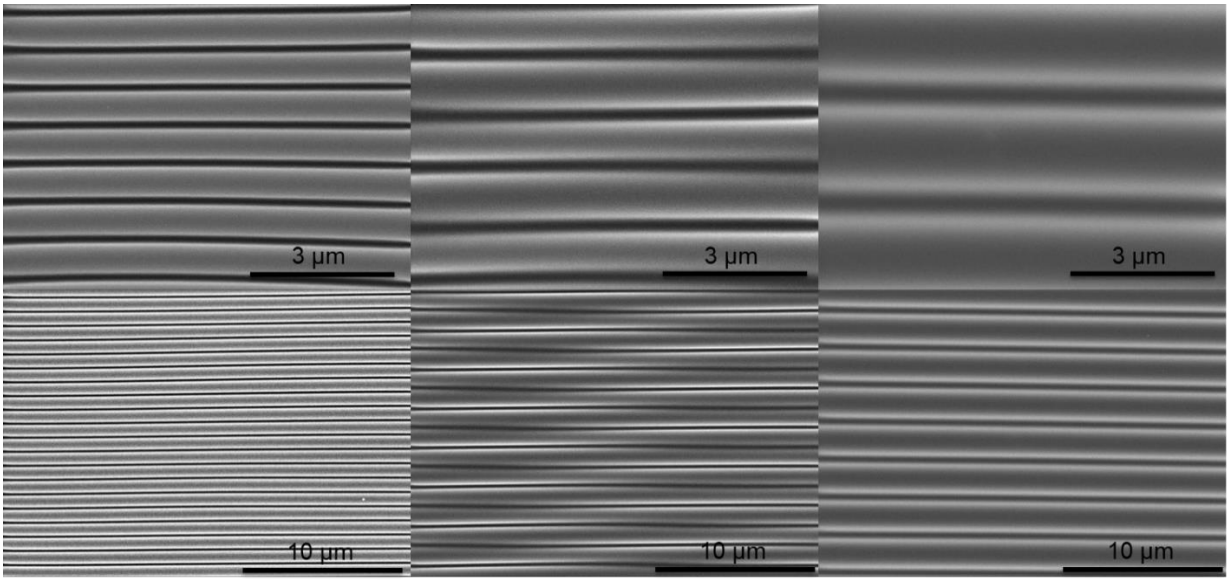

Figure 4.9. Tuning conformal wrinkle wavelength via variation of the surface silica layer thickness

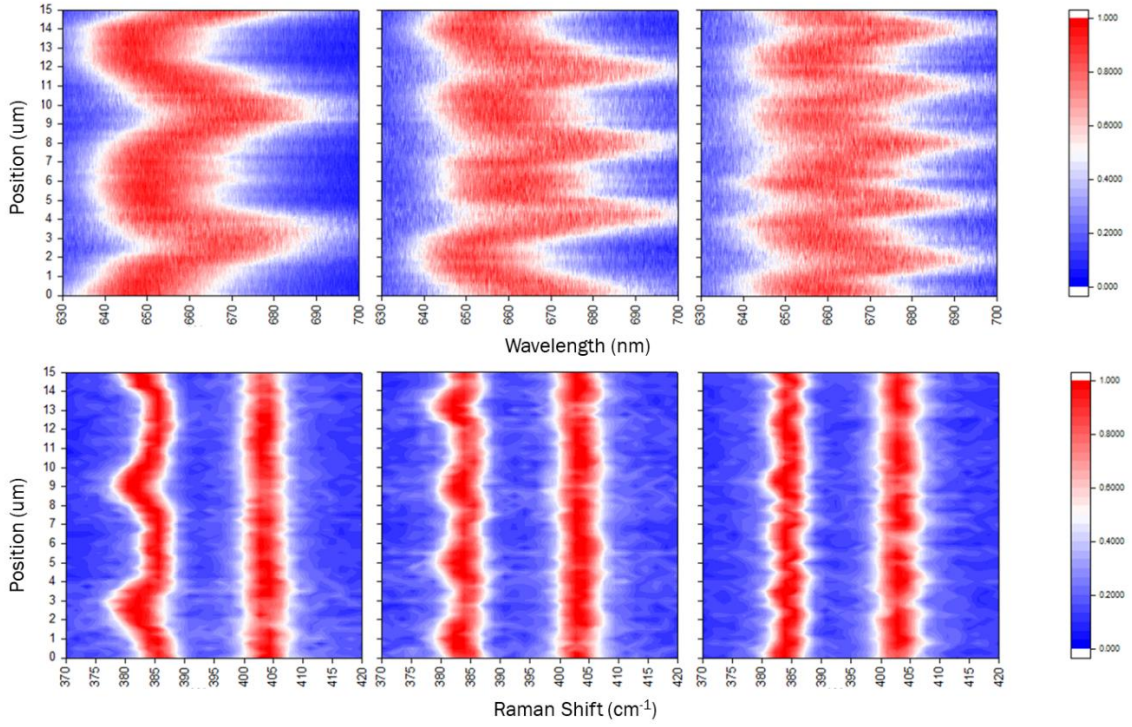

Figure 4.10. Line-mapped photoluminescence (top panels) and Raman (bottom panels) spectra for different samples of varying SOG thickness, exhibiting tunability to the superlattice characteristic wavelength.

By varying the thickness of the stiff SOG encapsulant while keeping the PDMS substrate the same, we can design strained superlattices with varying characteristic wavelengths. As an example, we present here three different superlattices (Figure 4.10) with wavelengths of 6.3, 4.1, and 3.2 um while keeping the macroscale strain relatively consistent (~9%). Such versatility allows to then tune the spectral dispersion (magnitude of local strain) via the macroscale compressive strain (Figure 4.8), while decoupling the independent control over the spatially varying strain gradient (intensity of spectral shift over lateral distance) by engineering the characteristic wavelength and amplitude of the wrinkled morphology.

To access even smaller (sub-micron) length scale morphologies (and thus strain confinement) and non-sinusoidal profiles towards stronger strain confinement and localization, we adopt the strategy similar to that described in the previous Chapter 3. Here, in contrast to the aforementioned conformal wrinkling on a compliant PDMS layer, the MoS_2 is directly adhered onto the polystyrene substrate via van der Waals interaction. Subsequent application of strain by the PS substrate results in non-conformal, buckling delamination of the MoS_2 off the PS surface and can form a variety of different morphologies, depending on the MoS_2 thickness and deformation scheme (Figure 4.11).

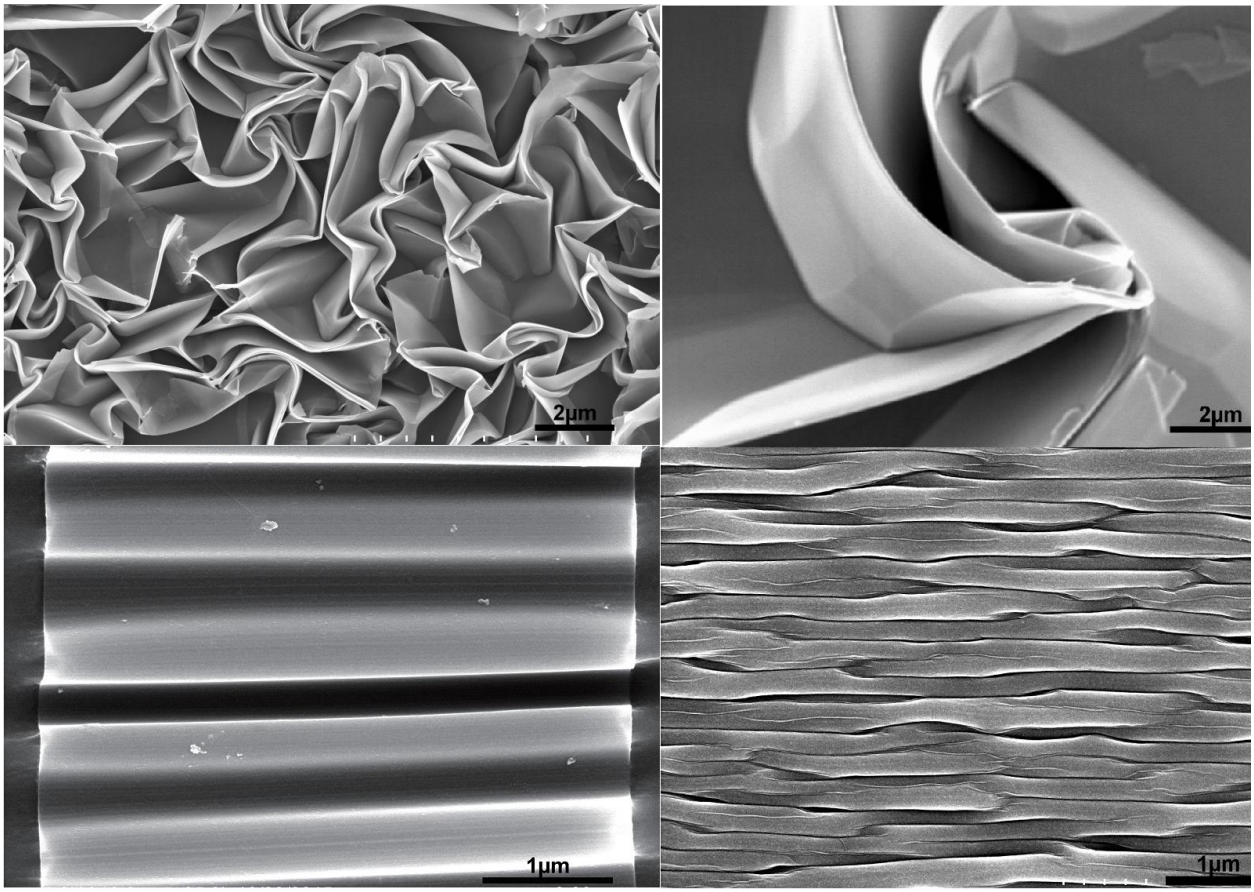

Figure 4.11. Various buckle delaminated crumpled morphology of multilayer MoS_2 are obtainable from the nanometer to micrometer scale via different substrate deformation schemes.

By buckling delamination, uniaxial grating-like MoS_2 superlattices with characteristic length scales below 100 nm may be obtained, which is below the diffraction limit and smaller than the excitation laser spot size of the optical spectroscopy techniques we have employed. Due to the buckling delamination process (or crumpling), portions of the MoS_2 becomes decoupled from the PS substrate, which effectively reduces substrate-induced scattering and associated non-radiative recombination, thereby resulting in brighter photoluminescence emission (Figure 4.12). With the excitation laser spot size averaging over multiple crumpled features, the photoluminescence emission is a convolution of the various strain states in the overall deformed MoS_2 architecture, and shows an overall compressive strain state (blue-shifted), indicative of the frustrated crumpling

morphology and consistent with our previous Raman observations with nanometer scale crumpled graphene.

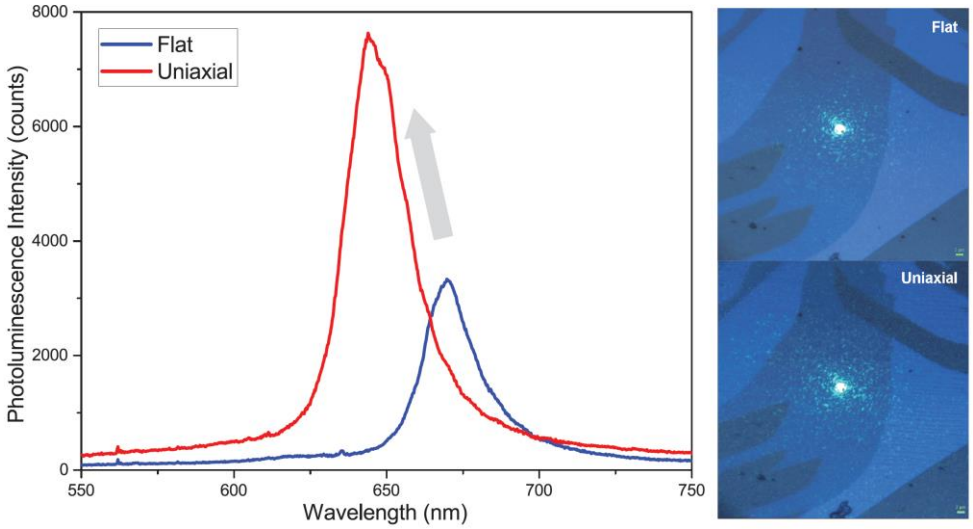

Figure 4.12. Blue-shift and enhancement of the monolayer MoS_2 photoluminescence A peak due to uniaxial crumpling on PS.

Due to the highly anisotropic and dense morphology of these uniaxial crumples, they effectively act as grating-like scatterers to the incident light. Analogous to the optically anisotropic patterned MoS_2 nanoribbons and semiconducting (InP) nanowires, we see that the uniaxially crumpled monolayer MoS_2 displays a linear dichroic effect.[33,34] Notably, when the linearly polarized green laser is aligned along the direction of the crumples, the luminescence intensity is greatly enhanced from when the same MoS_2 flake is flat on the substrate (Figure 4.13). Conversely, when the incident laser polarization is aligned across the wrinkles (along the k-vector of the grating like crumples), the photoluminescence intensity is not only just half of the aligned condition but is also suppressed compared to the flat morphology.

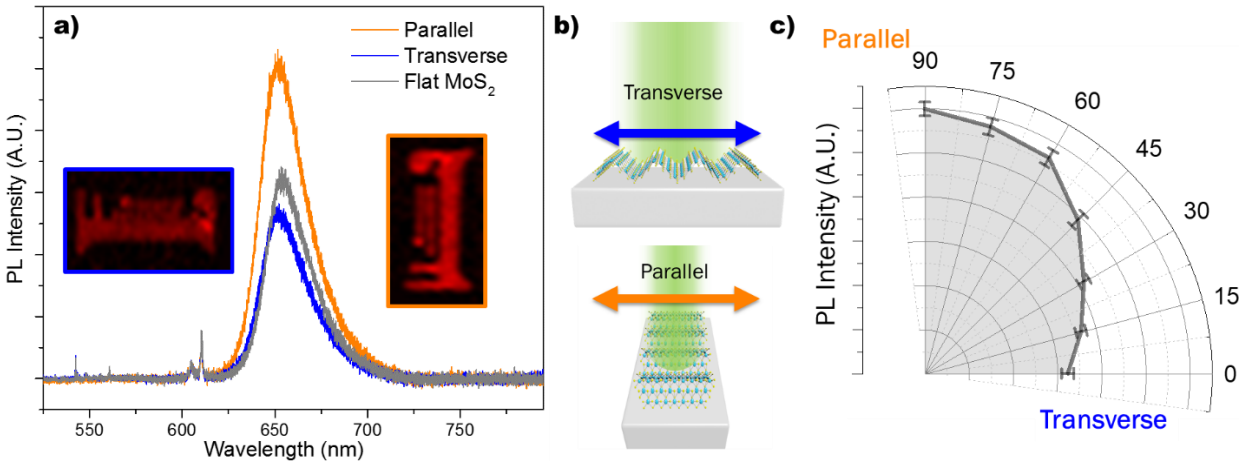

Figure 4.13. Uniaxial crumpling induced pseudo linear dichroism of the A photoluminescence peak intensity.

We observe a similar effect of higher intensity of both the characteristic Raman vibrational modes when the incident polarization is aligned with the crumples (Figure 4.14). However, the relative intensity ratio changes such that there is a larger enhancement of the out-of-plane A' (~402 cm^{-1}) peak compared to the in-plane E' peak (385 cm^{-1}). This could be due to the increased excitation of the out-of-plane phonon modes when the polarization is aligned.

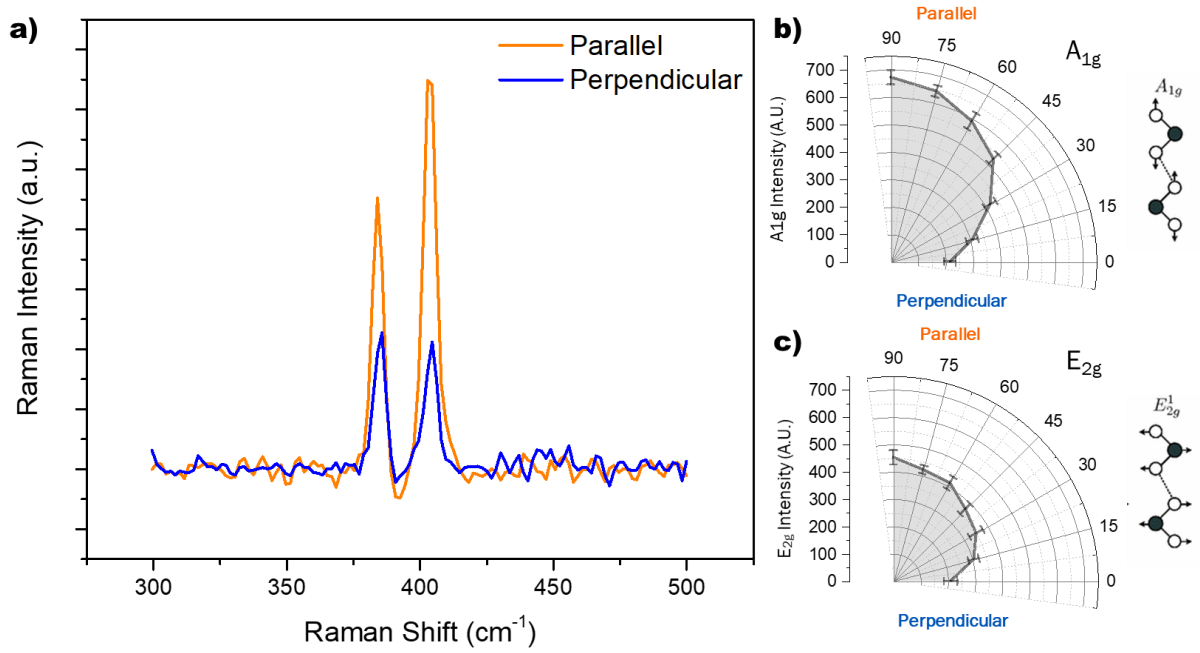

Figure 4.14. Uniaxial crumpling induced pseudo linear dichroism of the Raman spectra. The relative vibrational intensities ratio changes as a function of the incident polarization with respect to the crumpling morphology.

4.4. Conclusion

This chapter presents intriguing strain coupled phenomena that emerge due to heterogeneous deformations and strain gradients in atomically-thin 2D materials. Specifically, a robust approach is presented that enables facile creation of nano/micro-structured semiconducting TMDCs laterally strained superlattice structures via substrate transformation which yields periodic, heterogeneous strain that induces emergent material properties across a broad range of length-scales. Here, the periodic and heterogeneous strain profile generates spatially varying band structure and optical anisotropy in an otherwise homogeneous material. Such strain-induced morphologies are amenable for a variety of novel applications and phenomena including active tuning of carrier and phonon behavior, local band structure, excitonic funneling, flexoelectricity, spin/valleytronics, self-assembly, and enhanced basal plane photocatalysis.

4.5. Bibliography

(1) Novoselov, K. S.; Fal′ko, V. I.; Colombo, L.; Gellert, P. R.; Schwab, M. G.; Kim, K. *Nature* **2012**, *490*, 192–200.

(2) Novoselov, K. S.; Mishchenko, A.; Carvalho, A.; Castro Neto, A. H. *Science* **2016**, *353*, 461.

(3) Bhimanapati, G. R.; Lin, Z.; Meunier, V.; Jung, Y.; Cha, J.; Das, S.; Xiao, D.; Son, Y.; Strano, M. S.; Cooper, V. R.; Liang, L.; Louie, S. G.; Ringe, E.; Zhou, W.; Kim, S. S.; Naik, R. R.; Sumpter, B. G.; Terrones, H.; Xia, F.; Wang, Y.; Zhu, J.; Akinwande, D.; Alem, N.; Schuller, J. A.; Schaak, R. E.; Terrones, M.; Robinson, J. A. *ACS Nano* **2015**, *9*, 11509–11539.

(4) Wang, M. C.; Leem, J.; Kang, P.; Choi, J.; Knapp, P.; Yong, K.; Nam, S. *2D Materials* **2017**, *4*, 022002.

(5) Roldán, R.; Castellanos-Gomez, A.; Cappelluti, E.; Guinea, F. *Journal of Physics: Condensed Matter* **2015**, *27*, 313201.

(6) Bertolazzi, S.; Brivio, J.; Kis, A. *ACS Nano* **2011**, *5*, 9703–9709.

(7) Cooper, R. C.; Lee, C.; Marianetti, C. A.; Wei, X.; Hone, J.; Kysar, J. W. *Physical Review B* **2013**, *87*, 035423.

(8) Castellanos-Gomez, A.; Roldán, R.; Cappelluti, E.; Buscema, M.; Guinea, F.; van der Zant, H. S. J.; Steele, G. A. *Nano Letters* **2013**, *13*, 5361–5366.

(9) Qi, J.; Li, X.; Qian, X.; Feng, J. *Applied Physics Letters* **2013**, *102*, 173112.

(10) Lloyd, D.; Liu, X.; Christopher, J. W.; Cantley, L.; Wadehra, A.; Kim, B. L.; Goldberg, B.

B.; Swan, A. K.; Bunch, J. S. *Nano Letters* **2016**, *16*, 5836–5841.

(11) Cheiwchanchamnangij, T.; Lambrecht, W. R. L. *Physical Review B - Condensed Matter and Materials Physics* **2012**, *85*, 205302.

(12) Li, T. *Physical Review B - Condensed Matter and Materials Physics* **2012**, *85*, 235407.

(13) Johari, P.; Shenoy, V. B. *ACS Nano* **2012**, *6*, 5449–5456.

(14) Scalise, E.; Houssa, M.; Pourtois, G.; Afanas'ev, V.; Stesmans, A. *Nano Research* **2012**, *5*, 43–48.

(15) Peelaers, H.; Van De Walle, C. G. *Physical Review B - Condensed Matter and Materials Physics* **2012**, *86*, 241401.

(16) Shi, H.; Pan, H.; Zhang, Y. W.; Yakobson, B. I. *Physical Review B - Condensed Matter and Materials Physics* **2013**, *87*, 155304.

(17) Feng, J.; Qian, X.; Huang, C.-W.; Li, J. *Nature Photonics* **2012**, *6*, 866–872.

(18) Li, H.; Contryman, A. W.; Qian, X.; Ardakani, S. M.; Gong, Y.; Wang, X.; Weisse, J. M.; Lee, C. H.; Zhao, J.; Ajayan, P. M.; Li, J.; Manoharan, H. C.; Zheng, X. *Nature Communications* **2015**, *6*, 7381.

(19) Brotons-Gisbert, M.; Andres-Penares, D.; Suh, J.; Hidalgo, F.; Abargues, R.; Rodríguez-Cantó, P. J.; Segura, A.; Cros, A.; Tobias, G.; Canadell, E.; Ordejón, P.; Wu, J.; Martínez-Pastor, J. P.; Sánchez-Royo, J. F. *Nano Letters* **2016**, *16*, 3221–3229.

(20) Yang, S.; Wang, C.; Sahin, H.; Chen, H.; Li, Y.; Li, S.-S.; Suslu, A.; Peeters, F. M.; Liu, Q.; Li, J.; Tongay, S. *Nano Letters* **2015**, *15*, 1660–1666.

(21) Yu, L.; Ruzsinszky, A.; Perdew, J. P. *Nano Letters* **2016**, *16*, 2444–2449.

(22) Kumar, N.; Najmaei, S.; Cui, Q.; Ceballos, F.; Ajayan, P. M.; Lou, J.; Zhao, H. *Physical Review B - Condensed Matter and Materials Physics* **2013**, *87*, 161403.

(23) Malard, L. M.; Alencar, T. V.; Barboza, A. P. M.; Mak, K. F.; De Paula, A. M. *Physical Review B - Condensed Matter and Materials Physics* **2013**, *87*, 201401.

(24) Splendiani, A.; Sun, L.; Zhang, Y.; Li, T.; Kim, J.; Chim, C.-Y.; Galli, G.; Wang, F. *Nano letters* **2010**, *10*, 1271–1275.

(25) He, K.; Poole, C.; Mak, K. F.; Shan, J. *Nano letters* **2013**, *13*, 2931–2936.

(26) Ramasubramaniam, A. *Physical Review B* **2012**, *86*, 115409.

(27) Ross, J. S.; Wu, S.; Yu, H.; Ghimire, N. J.; Jones, A. M.; Aivazian, G.; Yan, J.; Mandrus, D. G.; Xiao, D.; Yao, W.; Xu, X. *Nature Communications* **2013**, *4*, 1474.

(28) Mak, K. F.; He, K.; Lee, C.; Lee, G. H.; Hone, J.; Heinz, T. F.; Shan, J. *Nature Materials* **2013**, *12*, 207–211.

(29) Liu, Z.; Amani, M.; Najmaei, S.; Xu, Q.; Zou, X.; Zhou, W.; Yu, T.; Qiu, C.; Birdwell, A. G.; Crowne, F. J.; Vajtai, R.; Yakobson, B. I.; Xia, Z.; Dubey, M.; Ajayan, P. M.; Lou, J. *Nature Communications* **2014**, *5*, 5246.

(30) Conley, H. J.; Wang, B.; Ziegler, J. I.; Haglund, R. F.; Pantelides, S. T.; Bolotin, K. I. *Nano Letters* **2013**, *13*, 3626–3630.

(31) Zhu, C. R.; Wang, G.; Liu, B. L.; Marie, X.; Qiao, X. F.; Zhang, X.; Wu, X. X.; Fan, H.; Tan, P. H.; Amand, T.; Urbaszek, B. *Physical Review B* **2013**, *88*, 121301.

(32) Song, J.; Jiang, H.; Liu, Z. J.; Khang, D. Y.; Huang, Y.; Rogers, J. A.; Lu, C.; Koh, C. G. *International Journal of Solids and Structures* **2008**, *45*, 3107–3121.

(33) Wu, J. Bin; Zhao, H.; Li, Y.; Ohlberg, D.; Shi, W.; Wu, W.; Wang, H.; Tan, P. H. *Advanced Optical Materials* **2016**, *4*, 756–762.

(34) Wang, J.; Gudiksen, M. S.; Duan, X.; Cui, Y.; Lieber, C. M. *Science* **2001**, *293*, 1455–1457.

Chapter 5. Plasmonic metamaterials via nano-convective/capillary self-assembly of 0D/1D nanoparticles on deformed 2D templates

5.1. Introduction

The deterministic organization 0D/1D plasmonic noble metal nanostructures and nanoparticles (NPs) with atomically-thin 2D layered materials (2DLMs) can lead to novel and tunable near-field quantum effects such as coupling of the plasmonic resonance with excitons between 0D/1D NPs (0D nanospheres/balls and 1D nanorods/wires) and 2D semiconductors. While mix-dimensionality nanoscale architectures and hybrid metameterials have been an area of active research, existing top-down strategies to precisely and scalably fabricate nanoscale resonant architectures based on lithographically definition followed by subsequent metal deposition are limited in their spatial resolution, material diversity, quality, and compatibility, and flexibility in morphological configurations for both the resonant nanostructures and the substrate material.

In contrast, a plethora of methods which has been developed for colloidal preparations of plasmonic nanoparticles are very versatile and highly scalable with excellent material quality and stoichiometry. Gold nanoparticles (AuNPs) or colloidal gold have been used by the ancients for staining glass and for its purported medicinal powers since as early as the fourth century.[1] Over the past decades, much research has centered on AuNPs for their strong interactions with light and their ability to sustain surface plasmons, which has wide uses ranging from surface enhanced Raman spectroscopy to plasmonic waveguides and metamaterials.[2] The characteristic local surface plasmon resonance (LSPR) and the resultant local electric fields are highly dependent on the particle size, shape, and local dielectric environment (including AuNP surface functionalization), resulting in a spectrum of beautiful colours in colloidal suspension.

Such vast library of AuNPs allows one to readily design arbitrary nanoscale constituent building blocks for self-assembly into meta-material structures on deformed 2DLM surfaces. When a plurality of noble metallic nanostructures is in close proximity, their individual modes can interact and form new hybrid modes and higher order interactions due to multiple scattering.[3] Lattice modes due to geometric resonance can also emerge when the wavelength of the scattered/incident is commensurate with the characteristic length scales and periodicities of the particle array. However, their solution form limits their potential in solid state and device form as NPs tend to form arbitrary or close-packed aggregates upon assembly onto surfaces (Figure 5.1). There is thus a need for practical methods to deterministically manipulate and control 0D/1D NPs at the nanoscale.

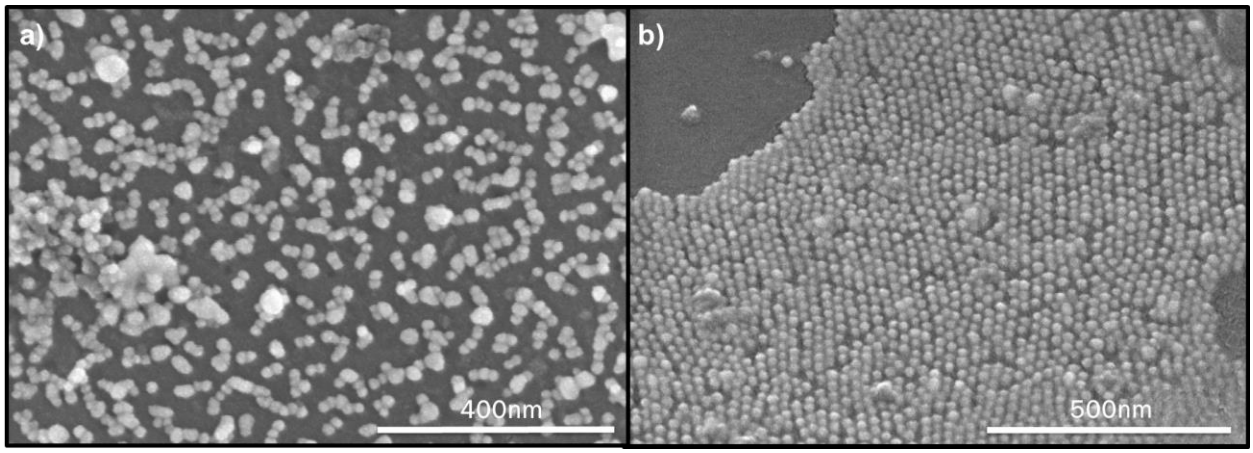

Figure 5.1. Morphology of gold nanospheres functionalized with polyethylene glycol dispersed onto (a) hydrophilic silica substrate (uniformly dispersed with some aggregation and without any particular order) and (b) hydrophobic polystyrene substrate (unevenly dispersed and hexagonally closed packed).

We have developed a generalized method to nano-manufacture mixed-dimensionality 0D/1D/2D meta-materials via self-assembly. By coupling the nanoscale surface morphologies formed via deformed atomically-thin 2DLMs with the dimensionalities of 0D/1D NPs, we can achieve large-

scale, highly-ordered self-assembly of 0D/1D plasmonic nanoparticle arrays on arbitrary 2DLM topographical templates.

This is achieved via nanoscale nano-convection/capillary driven self-assembly of 0D/1D NPs onto large-scale, heterogeneously strained, deformed 2DLM templates formed via strain induced mechanical surface instabilities (i.e., buckles, wrinkles, creases, etc.). By controlling simple material parameters, we design deformed 2DLMs templates with characteristic features spanning a few dozens of nanometers to several microns to match arbitrary dimensionalities and morphologies of various NPs. This method thus decouples the fabrication of the NPs from the substrate and allows independent control over the various processing factors. This allows one to take advantage of the now rapidly expanding library of methods to synthesize many 2DLMs via physical and chemical based vapour deposition.

This approach enables such versatile assembly (morphology, coverage, and ordering) including nanoparticle size, concentration, aspect ratio, surface and solvent chemistry, in addition to the conjugate properties in the deformed 2DLM template and supporting substrate (isotropy, periodicity, amplitude, surface energy).

By optimizing the various material properties and processing parameters, NPs as small as ten nanometers can be readily self-assembled up to the inch scale into well-organized, massively-parallel, single-file arrays onto deterministically deformed monolayer 2DLMs. A variety of high quality, colloidally-synthesized 0D/1D AuNPs of various geometries and surface chemistries may thus be organized onto deformed graphene and transition metal chalcogenide (TMDC) monolayers.

This development represents a first in realizing self-assembly with mixed-dimensionality deformed nanoscale materials and enables not only new tools to study emergent coupled phenomena in mixed low-dimensional heterogeneous systems but also as a general strategy to realize self-assembly based nanomanufacturing of novel low-dimensional material architectures.

5.2. Nano-convective/capillary self-assembly onto deformed 2D templates

To access a broad range of characteristic length scales and to assemble 0D/1D AuNPs of various shapes and sizes, we adopted two different patterning approaches to generate the deformed 2DLM templates. Separately, these are buckling delamination (crumpling) and conformal wrinkling, whereby the 2DLM corrugates through delamination from the polymeric substrate or conforms to the corrugations of the underlying polymeric substrate, respectively. Since both these approaches are mechanistic in nature, the templating process is material-agnostic and extendable to assembly onto arbitrary 2DLMs and thin film templates.

The ability to functionalize AuNPs with a variety of surface chemistries and to arbitrarily pattern 2DLMs via substrate deformation allows decoupling of the two constituent components. This enables separate control of the AuNPs' alignment/orientation, packing density, distribution, etc. independent from that of the substrate 2DLM and its configuration. This process can access length scales as small as tens of nanometers AuNPs while spanning centimeter scale without any prerequisite for lithographic definition. Such a self-assembly scheme for high quality, colloidally synthesized AuNPs on highly crystalline monolayer 2DLMs forgoes the issues associated with size and shape polydispersity in thermal annealing generated random gold patches and is also substantially more scalable and of better material quality than via e-beam/optical lithography followed by metal deposition.[4] As typically AuNPs tend to aggregate and close-pack into quasi-random geometries upon solvent removal, this development presents a simple solution to the long-

standing desire by the scientific community to realize highly ordered arrays of AuNPs in a scalable and precise fashion.[5]

The combination of plasmonic nanoparticles with 2DLMs to form hybrid 0D/1D/2D metamaterials systems has been have been an area of active research. For graphene-based metamaterials, these have included surface enhanced Raman spectroscopy,[6–8] enhanced photodetection,[9–11] and photocatalysis.[12] For monolayer semiconducting TMDCs, metallic plasmonic nanostructures have been used for excitonic photoluminescence pumping and plasmonic photoluminescence modulation, adatom induced doping, and plasmonically enhanced photocurrent.[13–15]

5.3. Experimental procedure

To prepare the substrate used to later impart strain-induced self-assembly of the 2DLM substrate, we thoroughly clean shape memory polystyrene (PS) sheets via ultrasonication in a mixture of deionized water and isopropanol. To fabricate templates with sub 100 nm length scale (buckling delamination crumpling), the PS sheet is used immediately as the substrate for 2DLM transfer. To fabricate templates with characteristic length scales of 250 nm and larger, the PS sheet is used as a substrate to spin-coat a thin film (~5 um) of Sylgard 184 PDMS elastomer (PDMS/PS). This PDMS thin film is then subjected to oxygen plasma for a few seconds to achieve the desired vitrified silica thickness for the target template length scale.

2DLM such as graphene and TMDCs grown via chemical vapour deposition (CVD) are then subsequently transferred onto the PS or PDMS/PS surface via solution-based transfer with a sacrificial handle layer from the growth substrate (copper foil or SiO_2 wafer) as previously reported. After thorough drying and removal of the sacrificial layer, the 2DLM is exposed at the top surface and is subsequently patterned via heat-activation of the underlying PS thermoplastic

above its glass transition temperature causing lateral strain. This induces the 2DLM to either crumple via buckle delamination (PS only, see Chapter 3) or wrinkle conformally (with the PDMS thin film, Figure 5.2) in a uniaxial fashion to form three-dimensional template features spanning from dozens of nanometers to several microns. The cleanliness of the 2DLM transfer process and homogeneity in the effective material thickness (e.g. uniformly monolayer with few multilayers or adlayers and free of trapped interfacial contaminants) are critically important to achieving uniform templates.

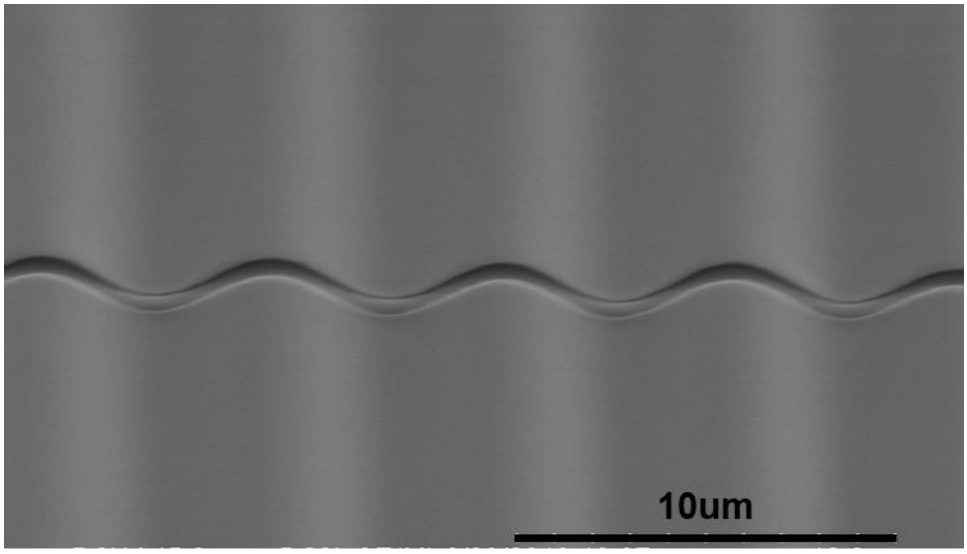

Figure 5.2 Tilt SEM of highly uniform uniaxial conformally wrinkled silica layer on PDMS. The silica layer was generated via surface vitrification of the PDMS substrate in oxygen plasma. The transverse cracks were intentionally introduced by bending the substrate to visualize the cross-section.

Gold nanospheres (AuNSs) smaller than 20 nm diameter were synthesized via a modified Turkevich method, whereas those lager than 30 nm were synthesized via the hydroquinone reduction route developed by Chan et al.[16,17] Long AuNRs, medium AuNRs, and short AuNRs were synthesized via methods developed by Busbee et al.,[18] Vigderman et al.,[19] and Murphy et al.,[20,21] respectively. AuNPs were functionalized with PEG coating of different molecular weights by incubation in a PEG-thio solution overnight. Several iterations of centrifugation and washing

with deionized water were done to remove excess PEG, before the solution being dispersed in ethanol for deposition. The AuNPs concentrations in ethanol solution were measured using UV-vis spectroscopy. Detailed procedures of the nanoparticle and decoration schemes are explained in my collaborator Dr. Wayne Lin's PhD dissertation.[22] The ability to uniformly self-assemble AuNPs on the 2DLM template is highly dependent on the choice of AuNPs shape and size, their surface chemistry/functionalization, solvent composition, and the subsequent deposition scheme. Monodispersity of the aforementioned properties of AuNPs is also critically important to yielding uniform assemblies on the large scale.

The AuNPs were self-assembled onto the 2DLM templates (Figure 5.3) via drop-casting the ethanol AuNP solution onto a freshly made substrate of appropriate characteristic length scales (crumple/wrinkle wavelength and amplitude). The sample is then kept perfectly levelled and left to dry. Care is taken to ensure the sample surface and surrounding environment is undisturbed to maintain uniform solution coverage, thus preventing the meniscus from breaking and forming undesired coffee rings or local film dewetting during the deposition and drying process.

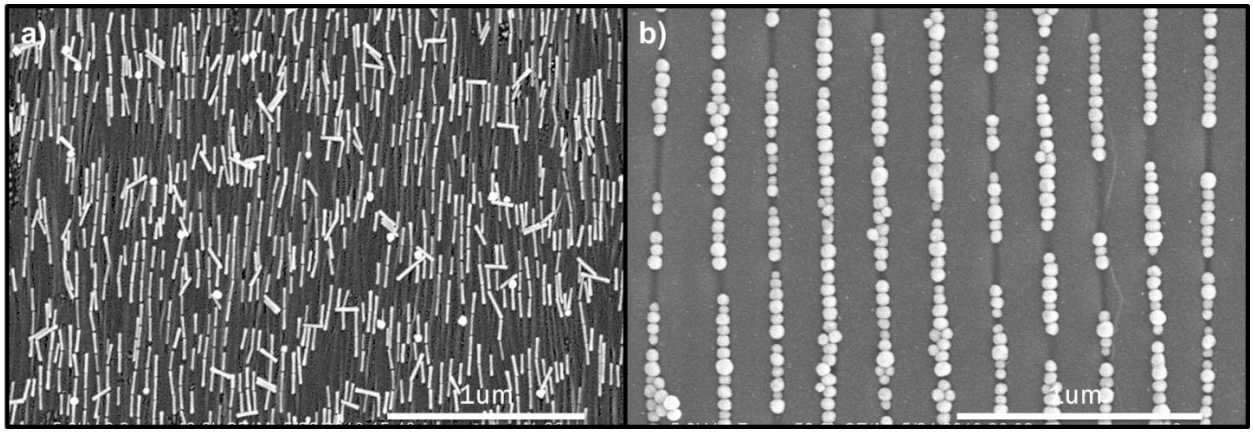

Figure 5.3. Self-assembly of 16x106nm NRs onto uniaxially crumpled graphene (a) and of 50nm NSs onto uniaxially conformally wrinkled graphene (b).

After the samples have completed the self-assembly process, they were characterized as-is via brightfield and darkfield optical microscopy, polarized UV-vis spectroscopy, micro-Raman spectroscopy, and micro-photoluminescence (PL) spectroscopy. Samples characterized using atomic force microscopy (AFM) were mounted and used as is; samples characterized under scanning electron microscope were coated with 3 nm of gold palladium via sputtering.

5.4. Materials characterization and analysis

To realize high fidelity, highly-anisotropic, single-file assemblies of the NPs onto the deformed 2DLM template, there are a few material quality considerations that must be ensured. Firstly, the template must be clean and uniform, with few interfacial contaminants from the 2DLM synthesis and transfer process and absent of spurious adlayers or adsorbates. The 2DLM should also be of mostly uniform thickness and be free of cracks or voids. The homogeneity and cleanliness of the 2DLM are critical to ensuring adequate adhesion to the polymeric substrate during the solution deposition process to avoid delamination and to generate a consistent and uniform wrinkling template pattern.

To mitigate arbitrary or non-specific particle assembly, the interaction between the surface and particle exterior should be repulsive in nature, which induces the particles to assemble in the wrinkle grooves via capillary forces during drying.[23,24] To prevent discontinuities in the surface energy which may promote unwanted film dewetting and uneven deposition, the 2DLM must be mostly free of cracks, voids, and wrinkles, etc. For example, if there are spurious wrinkles formed during the transfer process (while the substrate is still planar), they can remain as hierarchical wrinkles on the deformed template. These untended surface defects will tend to trap and induce assembly of AuNPs onto undesired locations (Figure 5.4a). Surface imperfections may also

adversely affect the template wrinkling uniformity, as seen by the presence of wrinklon bifurcations leading to discontinuities in the AuNPs assemblies (Figure 5.4b).

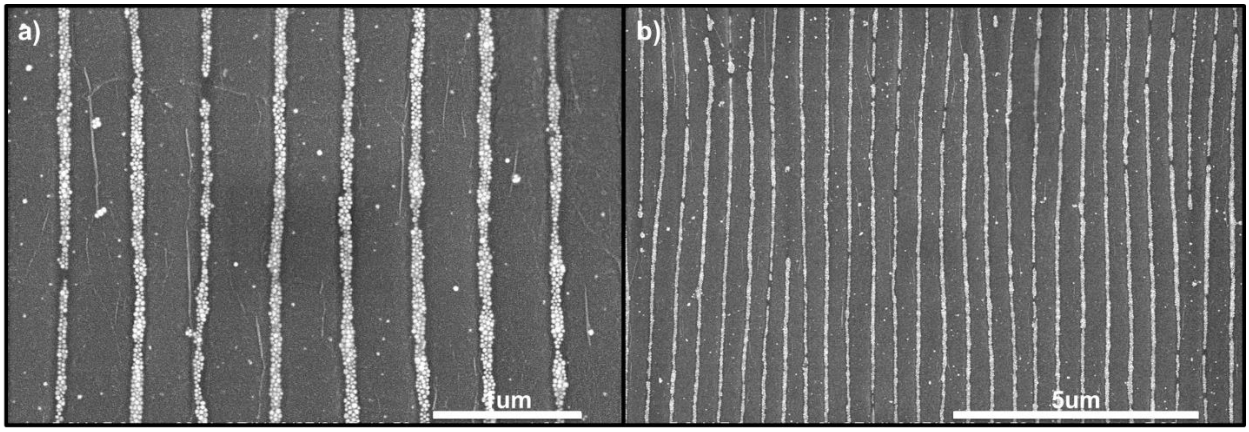

Figure 5.4. Overfilling and size mismatch of assembly. A) hierarchical wrinkles causing unintended assembly at arbitrary locations and b) wrinklons causing discontinuity in the assembled chains.

The morphology of the 2DLM template should be spatially uniform and dimensionally compatible with the AuNPs to be assembled. In particular, if the troughs or grooves of the wrinkled morphology are too wide and/or too deep for the target AuNPs, aggregates that are several particles wide or deep (filling into the trough) will form as opposed to well-organized single-file assemblies (Figure 5.4).

Conversely, the AuNPs fail to register with the wrinkles when the troughs are too shallow and flat. This non-deposition can be seen in the case of uniform bifurcation due to a large amount of macroscopic strain causing the originally sinusoidal wrinkles to form period-doubles (Figure 5.5). Here, the NRs tend to deposit into alternate rows where the troughs are of comparable widths to the diameter of the NRs, whereas there is only spurious deposition of random NRs and polydisperse NSs from the colloidal solution.

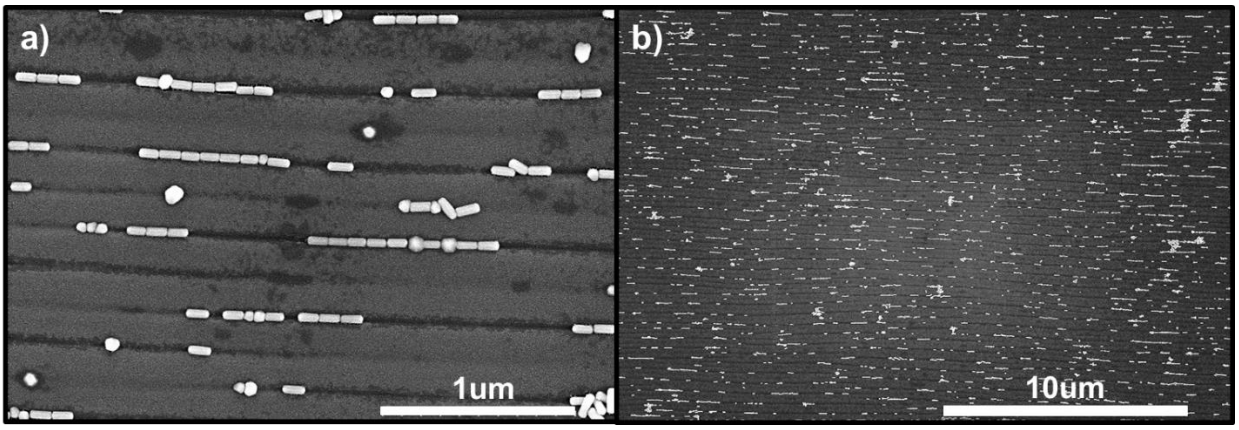

Figure 5.5. Alternate filling of NRs into wrinkle troughs of non-uniform dimensions due to bifurcation period doubling arising from excessive macroscale strain.

The ability to control the template morphology agnostic of the 2DLM and the AuNPs allows us to independently control the two orthogonal lattice parameters of the self-assembled metamaterial. Namely, the separation between the self-assembled chains (interchain spacing dictated by the wavelength of the template wrinkles) and the dimensions between the individual nanoparticles themselves (interparticle or intrachain spacing) may be designed independent of each other.

Thus, to control the interchain spacing, the wavelength of the wrinkled template substrate (and thus the wrinkle troughs) may be altered by tuning the amount of macroscopic compressive strain, surface film thickness, and the relative modulus mismatch between the surface film and the polymeric substrate. Since the wrinkling wavelength is also coupled to the trough depth and width, this can also be used to control the alignment density in each trough (single- or multi-file) and to suit the characteristic size of the AuNPs to be assembled. As an example, we could achieve nearly single file alignment of 20nm, 50nm, and 80nm AuNSs on conformally wrinkled graphene on PDMS (Figure 5.6).

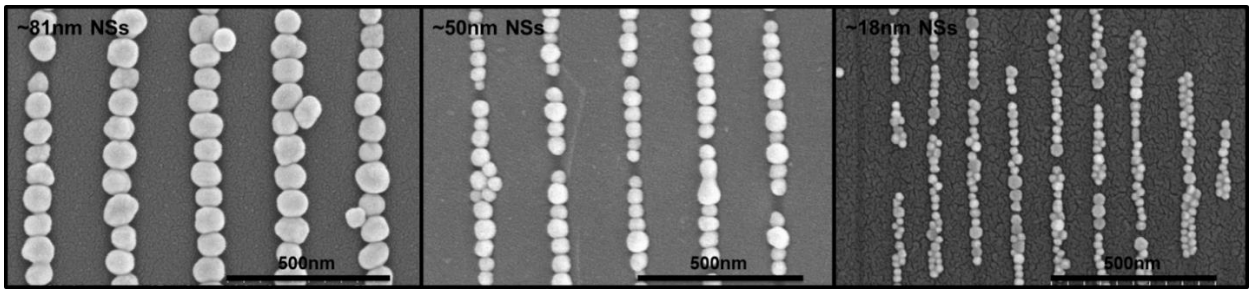

Figure 5.6. Nearly single file alignment of 20nm, 50nm, and 80nm AuNSs (5kDa PEG) on uniaxial conformally wrinkled graphene on PDMS.

To tune the interparticle or intra-chain spacing (Figure 5.7 and Figure 5.8), we decorate the surface of the AuNPs with polyethylene glycol of various molecular weights ranging from 5 to 40 kDa. Such flexible and independent control allows us to tune the lattice modes of the metamaterial by simply changing the constituent material properties and assembly processing parameters.

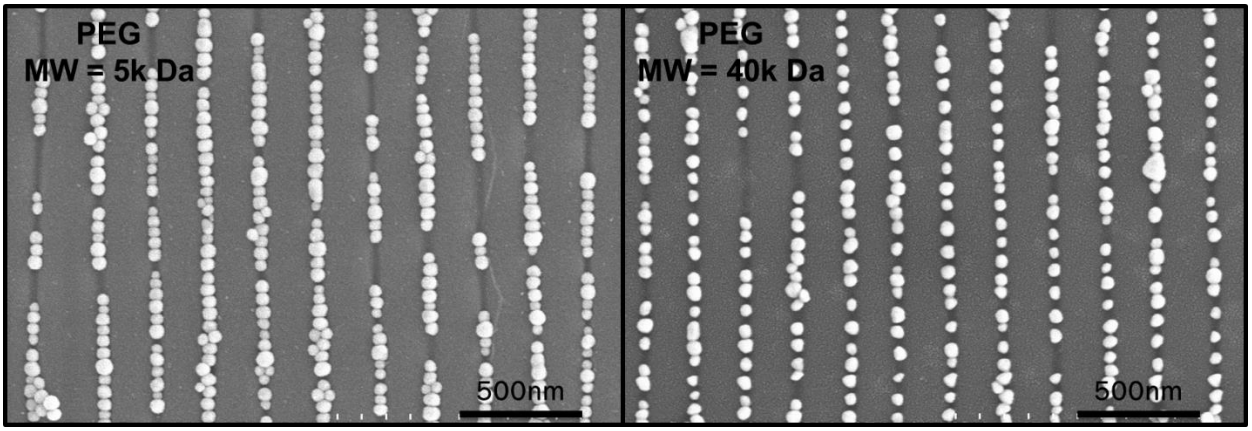

Figure 5.7. Single file self-assembled AuNSs (50nm) decorated with 5kDa PEG (left) are closer packed than those decorated with 40 kDa PEG (right) on conformally wrinkled graphene on vitrified PDMS.

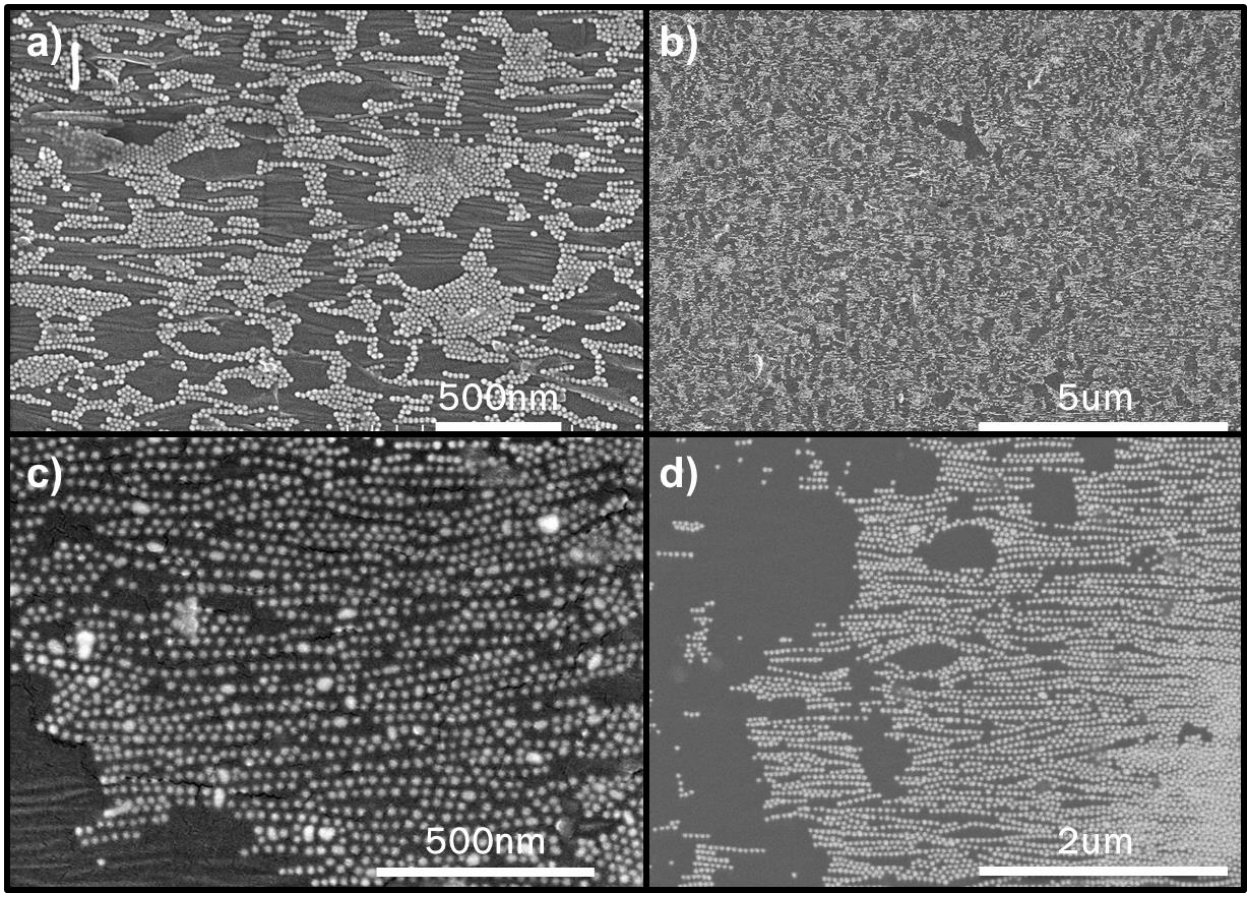

Figure 5.8. Influence of surface chemistry on interparticle assembly. AuNSs (20nm) decorated with 5kDa PEG (a-b) are closer packed than those decorated with 20 kDa PEG (c-d) on buckle delaminated uniaxial graphene crumples.

5.5. Emergent optical properties in 0D/1D/2D metamaterials

Since AuNPs intrinsically exhibit strong optical scattering and absorption, their emergent behavior can be characterized via optical spectroscopy. While AuNRs are intrinsically anisotropic (with characteristic transverse and longitudinal SPR modes), AuNSs are spherical and thus isotropic. Similarly sized AuNRs can generate field intensities at least an order of magnitude stronger than that by AuNSs.[17] Typically, when these AuNPs are deposited out of a colloid they will form closed packed structures. However, their self-assembly on 2DLMs is preferential to the valley regions of 2DLM wrinkles and crumples. This topological self-selectivity allows us to deterministically

realize end-to-end coupling of AuNRs and create highly uniform organization of the individual transverse and longitudinal modes, in addition to anisotropic lattice modes from otherwise isotropic AuNSs due to plasmonic coupling between adjacent AuNPs (red-shifted from their intrinsic LSPR). In particular, the ensemble of AuNPs into ordered lattices possesses large anisotropy that approaches seven orders of magnitudes (from dozens of nanometers width to centimeters long). Such structures thus exhibit polarizing effects that can be characterized via standard UV-vis spectroscopy and polarized angle-resolved spectroscopy (Figure 5.9).

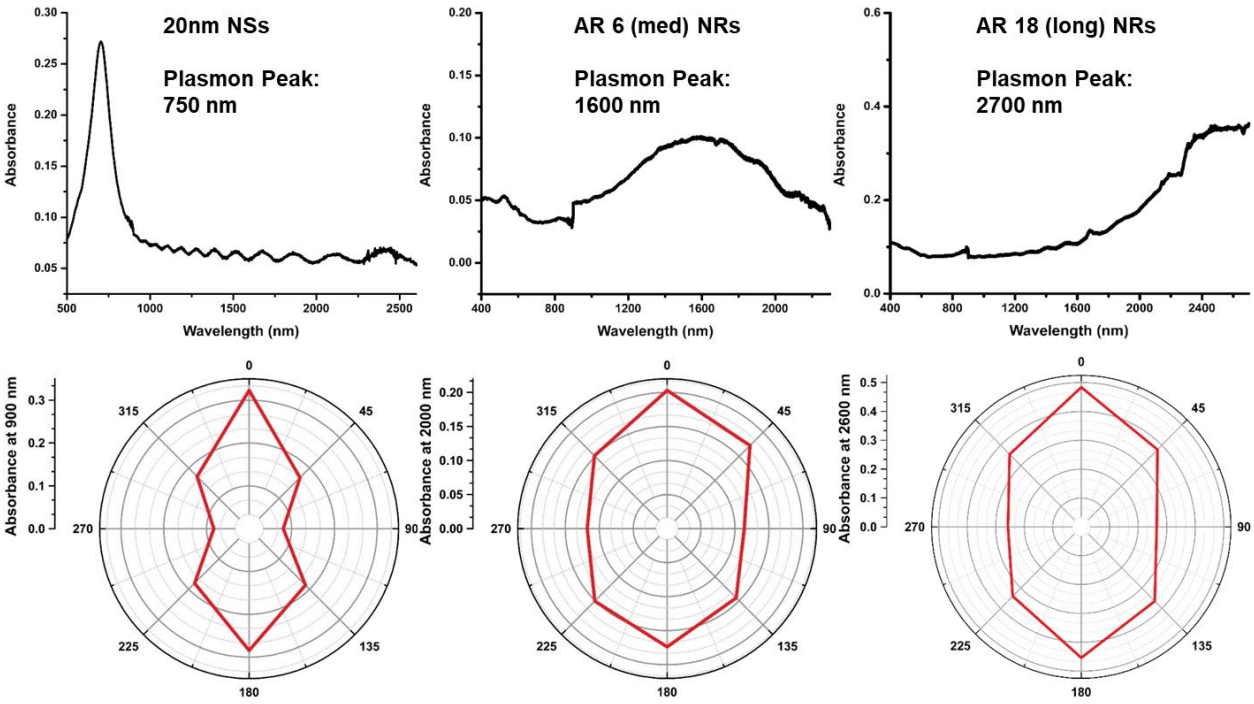

Figure 5.9.Optically anisotropic metamaterials. UV-vis spectra of various AuNPs self-assembled onto PDMS (top panels) and angular dependence of the plasmon peak intensity (bottom panels). Adapted from reference 22.

For example, the SPR peak of isotropic 20 nm AuNSs redshifts to ~800 nm in the ensemble from its original peak at 520 nm in colloidal solution. Analogously for the intrinsically anisotropic AuNRs (aspect ratio of 6), the longitudinal SPR peak redshifts from 1200 nm to 1600 nm, while

the transverse SPR peak remains at ~500 nm, since the highly anisotropic end-to-end alignment prevents coupling between the transverse modes. This selective coupling of only the longitudinal SPR and not the transverse SPR is indicative of the close end-to-end coupling of the AuNRs in their assembly onto conformal 2DLM wrinkles on the order of 200 nm or greater, which exceeds the critical coupling length. Such end-to-end self-assembly of intrinsically anisotropic AuNRs allows facile selective excitation of its transverse, longitudinal, and/or coupled lattice modes by simply changing the optical polarization.

To probe the polarizing effect of the AuNPs ensemble, we characterized the optically anisotropic metamaterials with single-axis angle-resolved polarized UV-vis (Figure 5.9). In the case of assembled AuNSs, polarization perpendicular to the assembled AuNS chains yields their individual LSPR (strongly red-shifted from colloidal solution) whereas polarization parallel to the chain length-wise direction probes the linear coupling between adjacent AuNSs.[25–27] Conversely, for the case of intrinsically anisotropic AuNRs, polarization perpendicular to the chain excites their transverse SPR modes whereas polarization parallel to the chain, the individual longitudinal modes and coupled end-to-end modes are excited.

For the 20 nm AuNSs, the maximum transmittance occurs at 90° and 270°, where the light polarization is parallel to the k-vector of the grating-like wrinkled substrate. Correspondingly, the maximum transmittance occurs when the light polarization is parallel to the chain ensemble of the AuNPs, yielding an anisotropic absorption ratio of almost five for the 20 nm AuNSs. Interestingly, the maximum/minimum absorption ratios for the longer (higher AR of 18) AuNRs is larger than that of the medium AuNRs (AR 6), which corroborates with SEM images suggesting some misalignment of some of the shorter polydispersed AuNRs in the trough of the conformally wrinkled structure.

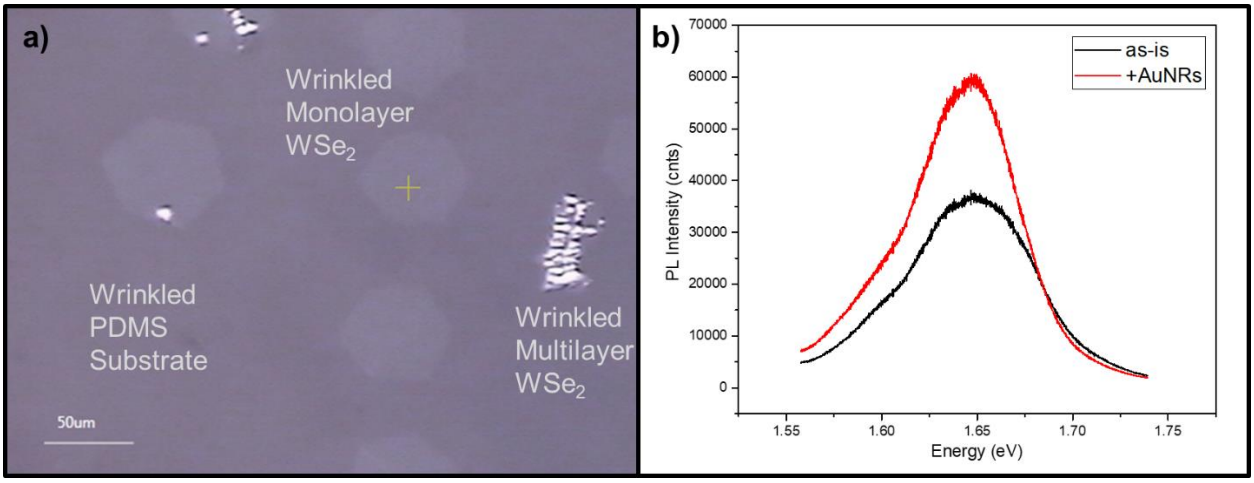

Figure 5.10. a) AR2.5 NRs self-assembled onto monolayer WSe_2 and b) area averaged PL before and after enhancement by AuNR.

One immediate ramification of plasmonic 0D/1D assemblies on 2DLMs is local confinement of light (far field excitation) and the resultant nearfield interaction between AuNP LSPR and TMDC optical transitions. The AuNPs support plasmonic mediated absorption and pumping of PL emission which results from surface enhanced absorption and reemission of the underlying 2DLM substrate in the form of stronger photoluminescence.

Earlier attempts by researchers to define metallic plasmonic features have faced challenges in patterning resolution, lateral scale, and material degradation resulting from the electron beam or photolithography process. To optimize the PL enhancement effect, AuNRs with LSPR and assemblies with lattice modes matching that of the optical bandgap of the 2DLM should be used. Here, discreet monolayer tungsten diselenide WSe_2 islands with a photoluminescence emission peak of 1.65 eV serve as the wrinkled self-assembly template. Subsequent deposition and self-assembly of AuNRs (13 x 43 nm) with an intrinsic longitudinal LSPR of 640 nm show a doubling of the PL signal over the bare wrinkled $WeSe_2$ (Figure 5.10). We note that with the addition of AuNRs, there is no observable PL broadening nor red-shifting as previously reported by Najmaei

et al. and Kang et al. for MoS_2 and AuNP hybrid structures.[13,28] There is also no evidence of significant changes to the spectral properties as previously observed with hot electron induced trigonal prismatic to octahedral (2H to 1T) phase transitions in MoS_2.[28] This robustness in the metamaterial provides an idea platform to investigate tunable plasmonic-excitonic interactions in hybrid noble metal/2D semiconductor nanostructured metamaterials.

5.6. Conclusion

We have developed a highly scalable and efficient method to nano-manufacture mixed-dimensionality 0D/1D/2D metamaterials on the macroscale via nanoscale convection/capillary self-assembly. This technique is agnostic to the selection of the constituent nanomaterial building blocks and enables assembly of arbitrary colloidally prepared NPs onto arbitrary 2D templates that span a wide length scale, overcoming challenges associated with lithographic definition of nanostructures on 2D materials and the poor polycrystallinity of deposited noble metal structures.

While only the first order of 0D/1D self-assembly onto 2DLMs has been shown here, the stability of the metamaterial in solution makes it amenable to further processing. For example, the order of operations for the architecturing of the 2DLM templates and AuNPs deposition may be arbitrarily repeated to further realize layer-by-layer nanomanufacturing of arbitrary 3D metamaterials consisting of stacked 0D/1D/2D heterostructures.

5.7. Bibliography

(1) Leonhardt, U. *Nature Photonics* **2007**, *1*, 207–208.

(2) Février, M.; Gogol, P.; Aassime, A.; Mégy, R.; Delacour, C.; Chelnokov, A.; Apuzzo, A.; Blaize, S.; Lourtioz, J.-M.; Dagens, B. *Nano Letters* **2012**, *12*, 1032–1037.

(3) Gunnarsson, L.; Rindzevicius, T.; Prikulis, J.; Kasemo, B.; Käll, M.; Zou, S.; Schatz, G. C. *Journal of Physical Chemistry B* **2005**, *109*, 1079–1087.

(4) Kravets, V. G.; Schedin, F.; Jalil, R.; Britnell, L.; Novoselov, K. S.; Grigorenko, A. N. *The Journal of Physical Chemistry C* **2012**, *116*, 3882–3887.

(5) Chen, H.; Shao, L.; Li, Q.; Wang, J. *Chem. Soc. Rev.* **2013**, *42*, 2679–2724.

(6) Schedin, F.; Lidorikis, E.; Lombardo, A.; Kravets, V. G.; Geim, A. K.; Grigorenko, A. N.; Novoselov, K. S.; Ferrari, A. C. *ACS Nano* **2010**, *4*, 5617–5626.

(7) Lee, J.; Shim, S.; Kim, B.; Shin, H. S. *Chemistry - A European Journal* **2011**, *17*, 2381–2387.

(8) Leem, J.; Wang, M. C.; Kang, P.; Nam, S. *Nano Letters* **2015**, *15*, 7684–7690.

(9) Liu, Y.; Cheng, R.; Liao, L.; Zhou, H.; Bai, J.; Liu, G.; Liu, L.; Huang, Y.; Duan, X. *Nature Communications* **2011**, *2*, 579.

(10) Echtermeyer, T. J.; Britnell, L.; Jasnos, P. K.; Lombardo, A.; Gorbachev, R. V.; Grigorenko, A. N.; Geim, A. K.; Ferrari, A. C.; Novoselov, K. S. *Nature Communications* **2011**, *2*, 458.

(11) Chen, X.; Jia, B.; Zhang, Y.; Gu, M. *Light: Science & Applications* **2013**, *2*, e92–e92.

(12) Zhang, H.; Fan, X.; Quan, X.; Chen, S.; Yu, H. *Environmental Science & Technology* **2011**,

45, 5731–5736.

(13) Najmaei, S.; Mlayah, A.; Arbouet, A.; Girard, C.; Léotin, J.; Lou, J. *ACS Nano* **2014**, *8*, 12682–12689.

(14) Lee, B.; Park, J.; Han, G. H.; Ee, H.-S.; Naylor, C. H.; Liu, W.; Johnson, A. T. C.; Agarwal, R. *Nano Letters* **2015**, *15*, 3646–3653.

(15) Singha, S. S.; Nandi, D.; Singha, A. *RSC Advances* **2015**, *5*, 24188–24193.

(16) Kimling, J.; Maier, M.; Okenve, B.; Kotaidis, V.; Ballot, H.; Plech, A. *Journal of Physical Chemistry B* **2006**, *110*, 15700–15707.

(17) Perrault, S. D.; Chan, W. C. W. *Journal of the American Chemical Society* **2009**, *131*, 17042–17043.

(18) Busbee, B. D.; Obare, S. O.; Murphy, C. J. *Advanced Materials* **2003**, *15*, 414–416.

(19) Vigderman, L.; Zubarev, E. R. *Chemistry of Materials* **2013**, *25*, 1450–1457.

(20) Jana, N. R.; Gearheart, L.; Murphy, C. J. Wet chemical synthesis of high aspect ratio cylindrical gold nanorods. *Journal of Physical Chemistry B*, 2001, *105*, 4065–4067.

(21) Gole, A.; Murphy, C. J. *Chemistry of Materials* **2004**, *16*, 3633–3640.

(22) Lin, W. The surface chemistry of nanoparticles: towards biological and engineering applications, University of Illinois at Urbana-Champaign, 2017.

(23) Tebbe, M.; Mayer, M.; Glatz, B. A.; Hanske, C.; Probst, P. T.; Müller, M. B.; Karg, M.; Chanana, M.; König, T. A. F.; Kuttner, C.; Fery, A. *Faraday Discuss.* **2015**, *181*, 243–260.

(24) Hanske, C.; Müller, M. B.; Bieber, V.; Tebbe, M.; Jessl, S.; Wittemann, A.; Fery, A.

Langmuir **2012**, *28*, 16745–16750.

(25) Solís, D. M.; Taboada, J. M.; Obelleiro, F.; Liz-Marzán, L. M.; García de Abajo, F. J. *ACS Nano* **2014**, *8*, 7559–7570.

(26) Funston, A. M.; Novo, C.; Davis, T. J.; Mulvaney, P. *Nano Letters* **2009**, *9*, 1651–1658.

(27) Hanske, C.; Tebbe, M.; Kuttner, C.; Bieber, V.; Tsukruk, V. V.; Chanana, M.; König, T. A. F.; Fery, A. *Nano Letters* **2014**, *14*, 6863–6871.

(28) Kang, Y.; Najmaei, S.; Liu, Z.; Bao, Y.; Wang, Y.; Zhu, X.; Halas, N. J.; Nordlander, P.; Ajayan, P. M.; Lou, J.; Fang, Z. *Advanced Materials* **2014**, *26*, 6467–6471.